Institut für Kernphysik und Nukleare Festkörperphysik
Fakultät für Physik E 15
Technische Universität München

Non-Destructive Mössbauer Spectroscopy in Archaeometallurgy

Andreas Kyek

Vollständiger Abdruck der von der Fakultät für Physik der Technischen Universität München zur Erlangung des akademischen Grades eines

Doktors der Naturwissenschaften (Dr. rer. nat.)

genehmigten Dissertation.

Vorsitzender: Univ.-Prof. Dr. M. Kleber
Prüfer der Dissertation:
1. Univ.-Prof. Dr. F.E. Wagner
2. Univ.-Prof. Dr. H.-J. Körner

Die Dissertation wurde am 20.4.2000 bei der Technischen Universität München eingereicht und durch die Fakultät für Physik am 15.6.2000 angenommen.

Zu den sanften, zu den guten
Herzen, die da schweigend bluten,
Hat das meine nie gezählt,
Aber zu den stürm'schen, weiten,
Die sich heiß ihr Glück erstreiten,
Kämpfend gegen ein Welt.

So um ein gewaltig Lieben
Ist es endlich Sieger blieben
Und zufrieden ruft es aus,
Aber nicht in Schlaf zu sinken,
Denn noch höh're Ziele winken
Bald zu neuem schweren Strauß.

Emerenz Meier

Summary

This work describes the applications of Mössbauer spectroscopy in the field of archaeometallurgy. Since studies of archaeological artefacts usually have to be non-destructive, this point is paid special attention.

After a introduction to Mössbauer spectroscopy, a detailed discussion is presented how Mössbauer spectra can be taken from samples that are too thick for measurements in the usual transmission geometry:

First there is conversion electron Mössbauer spectroscopy (CEMS), where electrons emitted after resonance absorption of γ-rays are detected and the probing depth is determined by the range of the conversion electrons in the sample material. This technique probes very thin layers on the surface of the samples. For the three Mössbauer isotopes which are of interest in the context of archaeometallurgy, namely ^{57}Fe, ^{119}Sn and ^{197}Au the special experimental arrangements are described. These vary according to the requirements of these isotopes, like energy of the Mössbauer transition, the Lamb-Mössbauer factor and temperature at which the measurements can be carried out. A Monte Carlo model is used to describe the conversion electron transport in the sample materials, from which the probing depth of CEMS in different materials can be calculated. For ^{197}Au the computed results were found to be in good agreement with covering experiments, where layers of metallic gold were put on a $AuAl_2$ substrate.

The second method for non-destructive Mössbauer spectroscopy uses back scattered γ- or X-rays as evidence of Mössbauer resonance absorption. The probing depth here is determined by the absorption of the incident γ-rays and the emerging radiation. Again different experimental arrangements and the operation of the Mössbauer spectrometer for the different Mössbauer isotopes are described. In analogy to the transmission integral in absorption experiments a backscattering integral is given to determine the shape of the Mössbauer resonance pattern in the backscattering spectra and the probing depth of the method. These calculations are again in good agreement with experimental results from measurements on gold foils of different thickness.

In the second part of this work two fields are presented in which the described techniques could be successfully applied. The first of these are strongly alloyed Celtic gold coins, which show an enrichment of gold near the surface. Using Mössbauer scattering techniques it is shown that there are areas of pure metallic gold of micrometer size on the surface and that there is furthermore a depletion of silver and copper in surface near regions. In different experiments it could be shown that the formation of pure metallic gold requires a phase separation into a silver rich and a copper rich phase

according the ternary gold-silver-copper phase diagram and a subsequent removal of the copper from the copper rich phase by diffusion and oxidation. Such a phase separation requires temperatures around 300 °C, but cannot be seen in the interior of the coins. This result and the fact that there are different coins of one and the same hoard, of which some show gold enrichment on the surface, while others do not, shows clearly that the gold enrichment on the surface is due to a special treatment of the coins by the ancient craftsmen and cannot be due to two thousand years of underground burial. A detailed model is given how the ancient craftsmen may have obtained the features that can be seen on the gold coins.

The second example deals with the application of backscattering Mössbauer spectroscopy in studies of iron artefacts. As examples Damascus steel swords and related objects from different historical contexts were chosen. These are a Bajuwarian spatha, a Japanese Katana, a German sabre, a British epée, a Indonesian kris and a Indian wootz bar. Also some experiments on modern Damascus steel objects are described. From the different possible phases which are suggested by the iron-carbon phase diagram only ferrite and cementite are found in the examined Damascus steel samples. The ferrite in the ancient objects is of remarkable purity. A model is given how the carbon content can be derived from the Mössbauer spectra. The results are discussed in relation to the notions on the making of Damascus steel. While the Japanese Katana, the German sabre and the British epée are similar in the carbon concentration and clearly under-eutectoid steel, the Bajuwarian spatha does not contain any iron-carbide at all, but has obtained its pattern from phosphorisation. The cementite content in the Indian wootz bar is very high as expected from the production process of this material. On the Indonesian kris traces of black burning are found. The modern Damascus steel objects show the formation of austenite due to traces of different alloying elements according the use of scrap material in modern steel production and recycling.

Contents

1 Introduction

Interdisciplinary cooperation becomes increasingly important for a better understanding of our world. To work on a subject in a foreign discipline requires learning the commonly used language and methods of this discipline. This work represents such an interdisciplinary effort in attempting to bridge nuclear solid states physics and archaeology by the use of Mössbauer spectroscopy on archaeological metal objects.

Mössbauer spectroscopy already has a reputation as a tool for characterising iron bearing samples like soils and ceramics. The investigation of archaeological ceramics has, indeed, become a major field of archaeometry. However, Mössbauer spectroscopy is not a tool that could be easily learned and used by any scientist in any discipline. The handling of the equipment, but also the complicated evaluation and interpretation of the measured Mössbauer spectra require some specialisation, probably more than for example electron microprobe analysis.

Archaeometallurgy is, to some extent, applied engineering in a discipline of anthropology. It describes the properties and production of metal objects from archaeological or at least historical contexts. The goal is to learn how ancient metalworkers may have treated their material for the production of weapons and tools as well as juwellery and coins. The skill of these craftsmen and the materials used by them reflects the cultural development of ancient people from the beginning of metal working in the early Bronze Age. Due to the fact that the knowledge of the craftsmen meant power, it was often a well hidden secret. Thus written evidence about antique metal working techniques are rare even for historic times and the today's scientist has only the objects themselves as a source of information.

The methods in analytical metallurgy are elemental and microstructural analysis, the first yielding information about the composition, the second about the metallurgical treatment (for example casting, welding, tempering and quenching). Typical techniques are, for instance, chemical analysis and microprobe analysis with an electron microprobe, and optical and electron micrography and X-ray diffraction for the detection of special phases. All of these methods are destructive since they require at least that the metal surfaces must be polished. Another widely used technique is X-ray or, less frequently used, neutron radiography or tomography to examine dirty and corroded objects, which is often only helpful to decide the feasibility of further investigation. Indeed archaeometallurgy always attempts to clean the object down to the bare metal since it is of no particular interest to study the surface corrosion. Corrosion always destroys the original chemical composition as well as the metallographic structure.

In many cases the metallic finds are so valuable, like for example gold coins and swords, that destructive methods cannot be applied. Then only typological aspects can be used for a description, or one has to find non-destructive methods that can yield information on the object.

This work describes the use of non-destructive Mössbauer spectroscopy in archaeometallurgy. Mössbauer spectroscopy uses γ-rays to study the hyperfine interactions of the nuclei of the Mössbauer isotope with the surrounding lattice. These interactions are typical for the chemical state or states of the atoms in the given phases. After a brief description of the theoretical foundations of Mössbauer spectroscopy and the most commonly used set-up in transmission mode, it is shown how Mössbauer spectroscopy can be used as a surface sensitive probe (Conversion Electron Mössbauer spectroscopy CEMS) as well as for studying objects that are too thick for transmission experiments (Mössbauer spectroscopy in backscattering mode). A detailed description will be given of the set-up of the Mössbauer spectrometer for the different Mössbauer isotopes that are of interest for archaeometallurgy: ^{197}Au for gold alloys, ^{119}Sn for studying tin in bronze objects and ^{57}Fe for iron and steel objects. The last two chapters focus on the analysis of Celtic gold coins and Damascus steel swords and demonstrate the application of the technique and what kind of information it yields.

2 The Theory of Mössbauer Spectroscopy

2.1 Introduction

This chapter describes the principles of Mössbauer spectroscopy, a technique to detect the resonant emission and absorption of γ-rays in solids. As an example, the Mössbauer isotope ^{197}Au will be discussed, but specific properties of ^{57}Fe and ^{119}Sn will also be considered, since they are also used in this work.

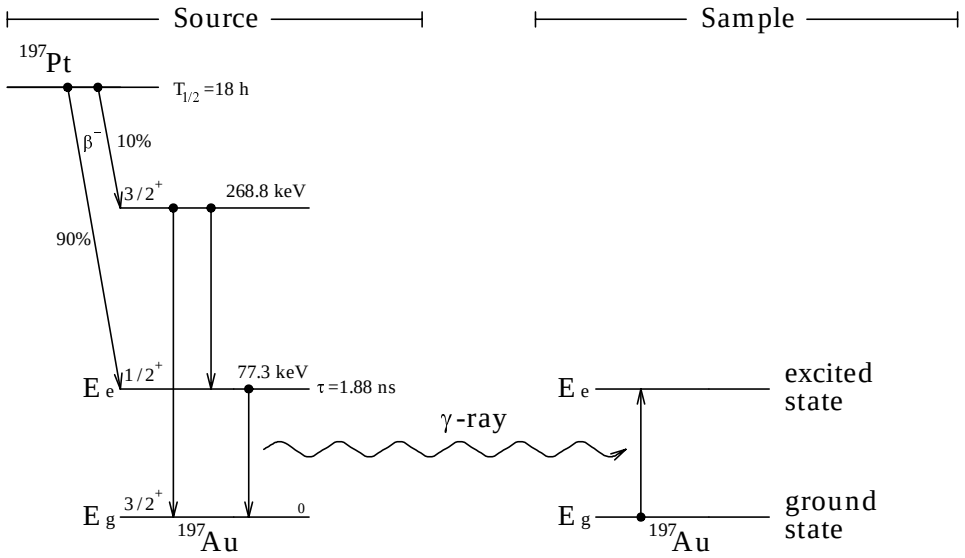

Fig. 2.1: Emission and absorption of a γ-ray in the Mössbauer effect

Figure 2.1 describes the principle of resonant absorption: A radioactive source isotope decays forming an excited daughter nucleus. In the case of ^{197}Au Mössbauer spectroscopy the source isotope is ^{197}Pt, which decays according to

$$^{197}\mathrm{Pt} \longrightarrow {}^{197}\mathrm{Au}^{*} + \beta^{-} + \overline{\nu_{\mathrm{e}}}. \tag{2.1}$$

The excited ^{197}Au* nucleus will then decay into the ground state by emission of a γ-ray with an energy of $E_0 = 77.3\,\mathrm{keV}$. If the nucleus is bound into a solid, an energy loss due to the production or annihilation of phonons may occur, but there will be a finite

probability that no emission or absorption of phonons occurs. Such processes are called recoil-free emission processes. The probability for the emission of a γ-ray without the involvement of phonons is called the *Lamb-Mössbauer factor* or *f-factor*. The f-factor depends on temperature, the γ-ray energy and the binding forces in the lattice solid. Iron and tin can be measured well at room temperature, while gold should be kept close to liquid helium temperature. The recoil-free emitted γ-ray from the source may now be resonantly absorbed by a ^{197}Au nucleus in the sample, by inducing a transition of this nucleus to the excited state. With the typical lifetime of the excited state the nucleus will decay again to the groundstate, emitting either a γ-ray or a conversion electron followed by an X-ray or an auger electron. This radiation can be used to detect the resonant absorption process. The number of emitted conversion electrons compared to the number of re-emitted γ-rays is given by the conversion coefficient α. The conversion electrons will have the energy of the excited state of the nucleus minus the binding energy of the emitted electron. The subsequently emitted X-ray stem from the fluorescent X-ray emission when the hole in the electron shell of the Mössbauer atom is filled. Both the conversion electrons and the emitted X-ray cannot be distinguished from photo electrons and X-ray emission induced by the photo effect, respectively.

In order to scan the resonance, one uses the Doppler effect by moving source (or absorber) with appropriate velocities. In fact, to record a Mössbauer spectrum one records the count rate in the detector as a function of velocity.

Figure 2.2 shows the different ways the resonant absorption process can be detected:

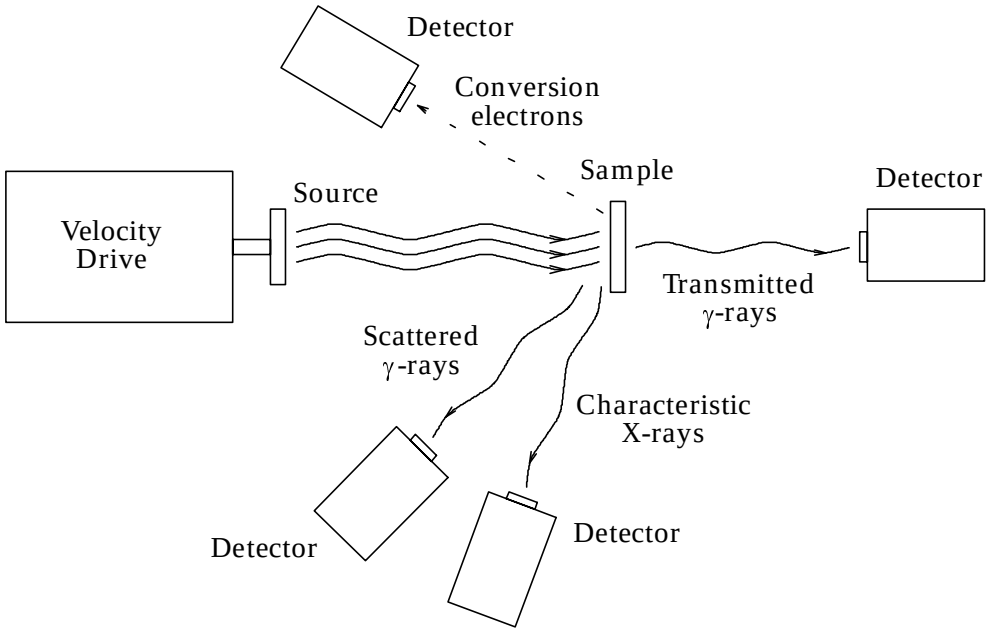

Fig. 2.2: Schematic set-up of a Mössbauer experiment demonstrating the different possibilities of detector positioning.

- In an absorption experiment by observing the γ-rays transmitted through the absorber. At resonance the number of transmitted γ-rays is reduced.

- By detecting the scattered γ-rays.
- By detecting the conversion electrons.
- By detecting the characteristic X-rays after the conversion process.

The absorption experiment is the standard geometry in Mössbauer spectroscopy, the sample is therefore often called *absorber* even in the other detection modes. In the following, the sample or absorber will be referred to by the subscript A, while the source is referred to by the subscript S.

The information one obtains from Mössbauer spectra stems mainly from the shift and splittings of the Mössbauer resonance arising from the hyperfine interactions of the Mössbauer nuclei with their solid state environment.

Table 2.1 shows a summary of important data concerning the three Mössbauer isotopes discussed in this work.

2.2 The Lamb-Mössbauer Factor

The Lamb-Mössbauer factor, or f-factor, describes quantitatively the fraction of resonantly emitted (or absorbed) γ-rays in the total number of emitted γ-rays from the excited resonant state of the Mössbauer isotope. The f-factor can be described as the probability of emission or absorption without change of the phonon state of the crystal(Wegener 1966):

$$f(T) = \overline{|\langle n|e^{-i\mathbf{kx}}|n\rangle|}. \tag{2.2}$$

Here, $|n\rangle$ describes the phonon state of the lattice, the bar indicates the thermodynamic averaging over all possible states of the lattice, and $\mathbf{x}$ the displacement of the Mössbauer nucleus from its equilibrium position. Assuming a harmonic lattice potential one obtains

$$f(T) = \exp\left(-\overline{\langle n|(\mathbf{kx})^2|n\rangle}\right), \tag{2.3}$$

and in case of a cubic lattice,

$$f(T) = \exp\left(-k^2\overline{\langle n|x^2|n\rangle}/3\right). \tag{2.4}$$

For an explicit expression for the f-factor one has to use a specific lattice model. The Debye model yields:

$$f_D(T) = \exp\left\{-\frac{E_0^2}{2Mc^2}\cdot\frac{3}{2k_B\Theta}\left[1+4\left(\frac{T}{\Theta}\right)^2\int_0^{\Theta/T}\frac{x\,\mathrm{d}x}{e^x-1}\right]\right\}. \tag{2.5}$$

Θ is the Debye temperature, which may differ from the usual given Debye temperature derived from the specific heat, since the real phonon spectrum differs from that of the Debye model and influences the f-factor and the specific heat in different ways. From

Tab. 2.1: Summary of important data for the Mössbauer transitions of ^{197}Au, ^{119}Sn and ^{57}Fe. The data are from Stevens (1978), Schatz (1985), Prosser (1975), Shenoy (1978), Crecelius (1973), Storm and Israel (1970) and Johnson (ASTM DS46).

Mössbauer isotope	^{197}Au	^{119}Sn	^{57}Fe
Isotope abundance	100%	8.58%	2.14%
Usual source isotope	^{197}Pt	^{119m}Sn	^{57}Co
Half life $T_{1/2}$ of source isotope	18.3 h	250 d	270 d
Mössbauer transition	$1/2^+ \rightarrow 3/2^+$ $M1 + 14.2\%E2$	$3/2^+ \rightarrow 1/2^+$ $100\%M1$	$3/2^- \rightarrow 1/2^-$ $100\%M1$
Life time τ of Mössbauer transition	1.879 ns	25.77 ns	141.1 ns
Transition energy E_γ	77.34 keV	23.87 keV	14.41 keV
Resonant cross section σ_0	$3.86 \cdot 10^{-20}$ cm^2	$1.40 \cdot 10^{-18}$ cm^2	$2.56 \cdot 10^{-18}$ cm^2
Energy equivalent 1 mm/s =	$2.580 \cdot 10^{-7}$ eV	$7.962 \cdot 10^{-8}$ eV	$4.807 \cdot 10^{-8}$ eV
Line width 2Γ	1.882 mm/s	0.642 mm/s	0.194 mm/s
Magn. moment μ			
excited state	$+0.4163\,\mu_N$	$+0.681\,\mu_N$	$-0.1553\,\mu_N$
ground state	$+0.1448\,\mu_N$	$-1.0462\,\mu_N$	$+0.09060\,\mu_N$
Elec. quad. moment Q			
excited state	0	−0.06 barn	+0.2 barn
ground state	+0.594 barn	0	0
Change $\Delta\langle r^2\rangle$ of nucleus charge radius	$+8.6 \cdot 10^{-3}$ fm^2	$+3.3 \cdot 10^{-3}$ fm^2	$-14.3 \cdot 10^{-3}$ fm^2
Conversion coefficient α	4.3	5.1	8.2
Electron bonding energies			
K-edge	80.7 keV	29.2 keV	7.1 keV
L_I-edge	14.3 keV	4.5 keV	0.8 keV
L_{II}-edge	13.7 keV	4.2 keV	0.7 keV
L_{III}-edge	11.9 keV	3.9 keV	0.7 keV
M-edge	2.9 keV	0.9 keV	0.1 keV

Equation 2.5 one also sees that even for $T = 0$ the f-factor cannot become 1 because of the quantum mechanical zero point motion of the atoms. Moreover one sees that a large f-factor results for a small transition energy E_0, a large atomic mass M and a high Debye temperature Θ. Equation 2.5 is only valid for pure elements. Thus it is invalid for most sources, including gold, where the ^{197}Au nuclei are placed in a platinum matrix. However, as illustrative examples, Figure 2.3 shows the f-factor of ^{197}Au in metallic gold, ^{119}Sn in metallic tin and ^{57}Fe in metallic iron, where the Debye temperatures are

Θ =180 K, 170 K and 450 T, respectively. From Figure 2.3 it becomes quite obvious why gold should be measured at liquid helium temperature, while tin and particulary iron can be measured at room temperature.

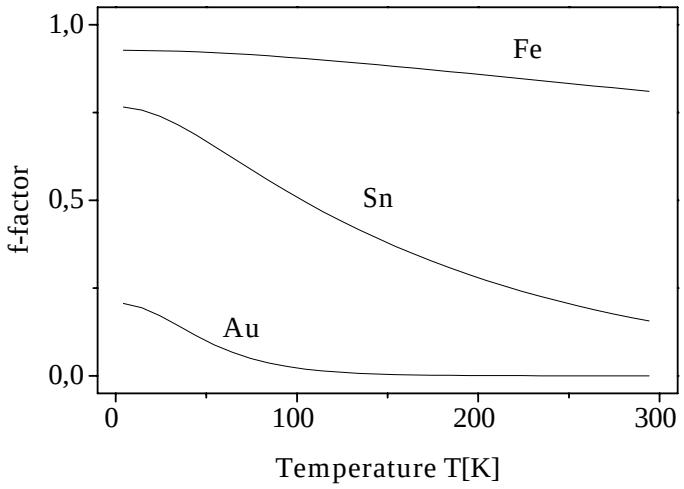

Fig. 2.3: f-factor of ^{197}Au in metallic gold, ^{119}Sn in metallic tin and ^{57}Fe in α-iron as a function of temperature according Equation 2.5.

2.3 Line Shape

The damped electromagnetic wave emitted by a source nucleus can be described by the wave function

$$\Psi(t) = e^{-i\left(\omega_0 - i\frac{\Gamma}{2\hbar}\right)t} \quad . \tag{2.6}$$

Here $E_0 = \hbar\omega_0$ is the transition energy and Γ the width of the excited state due to the Heisenberg uncertainty relation. A Fourier transformation of Equation 2.6 yields

$$F(\omega) = \int e^{i\omega t}\Psi(t)\mathrm{d}t = \int e^{i\left[(\omega-\omega_0)+i\frac{\Gamma}{2\hbar}\right]t}\mathrm{d}\omega = \frac{1}{i\left[(\omega-\omega_0)+i\frac{\Gamma}{2\hbar}\right]}, \tag{2.7}$$

which leads to a frequency spectrum

$$|F(\omega)|^2 = \frac{1}{(\omega-\omega_0)^2 + \left(\frac{\Gamma}{2\hbar}\right)^2} \tag{2.8}$$

and to the emitted energy spectrum normalised to the area S_0

$$S(E) = S_0 \cdot \frac{\frac{\Gamma}{2\pi}}{(E-E_0)^2 + \left(\frac{\Gamma}{2}\right)^2}. \tag{2.9}$$

This is referred to as a lorentzian energy spectrum. If the source is moving with a velocity v, E_0 is changing to $E_0(v) = E_0 \cdot (1 + v/c)$ owing to the Doppler effect and one obtains:

$$S(E, v) = S_0 \cdot \frac{\frac{\Gamma}{2\pi}}{\left(E - E_0 \cdot (1 + v/c)\right)^2 + \left(\frac{\Gamma}{2}\right)^2}. \tag{2.10}$$

Positive velocities v describe a movement of the source towards the absorber.

Like the emission spectrum, the resonant absorption cross section also depends on energy in lorentzian form:

$$\sigma(E) = \sigma_0 \frac{(\Gamma/2)^2}{(E - E_0)^2 + (\Gamma/2)^2}, \tag{2.11}$$

with

$$\sigma_0 = \frac{2\pi c^2 \hbar^2}{E_0^2} \cdot \frac{2I_e + 1}{2I_g + 1} \cdot \frac{1}{1 + \alpha} \tag{2.12}$$

where I_e and I_g are the spins of the nucleus in the excited state and ground state respectively and α is the conversion coefficient.

To obtain the shape of the measured spectrum one has to fold the cross section for resonant absorption with the emission spectrum over the whole energy range:

$$S(v) = \int_{-\infty}^{\infty} S(E, v) \exp\left(-n z_A f_A \sigma(E)\right) \mathrm{d}E \tag{2.13}$$

where n is the number of the Mössbauer nuclei per volume in the absorber, z_A the (geometrical) thickness of the absorber and f_A its f-factor. In the case of very thin absorbers, where $n \cdot z_A \cdot f_A \cdot \sigma_0 \ll 1$, one can expand the exponential in Equation 2.13 in a rapidly converging Taylor series. Using only the first order term of this series, one can solve the integral analytically, which results in a lorentzian form with a width of 2Γ:

$$S(v) = S_0 \cdot n \cdot z_A \cdot f_A \cdot \frac{\sigma_0}{2} \cdot \frac{\Gamma^2}{\left(E \cdot \frac{v}{c}\right)^2 + \Gamma^2}. \tag{2.14}$$

Especially for conversion electron Mössbauer spectroscopy (CEMS), where the range of the electrons in the absorber (probing depth) determines the absorber thickness, one is in the limit of thin absorbers. In this case it is very convenient to use the simplified lorentzian lineshape or a sum of lineshapes.

In case of Mössbauer spectroscopy using backscattered γ-ray or X-ray one is often at the saturation limit. Here one has to solve Equation 2.13 numerically. The appropriate equations will be given later, since they depend also on the geometry of the measurement.

2.4 Hyperfine Interactions

The interactions of electrical and magnetic fields with the charge and current distribution of the nucleus are called hyperfine interactions. They lead to shifts and splittings of the resonant line in the Mössbauer spectrum and are characteristic of the given chemical surroundings of the nucleus in the solid.

The interaction energy of the charge distribution $\rho(\mathbf{x})$ and the current distribution $\mathbf{j}(\mathbf{x})$ of the nucleus with the electromagnetic field produced by the electrons in the solid is given by (Jackson 1974)

$$E = \int \rho(\mathbf{x})\Phi(\mathbf{x}) + \mathbf{j}(\mathbf{x}) \cdot \mathbf{A}(\mathbf{x}) \, \mathrm{d}^3x, \tag{2.15}$$

where Φ is the electrostatic potential and $\mathbf{A}$ the vector potential. The integration extends over the volume of the nucleus. The electromagnetic field of the electron shell varies only weakly within this volume, so the potentials can be expanded into a Taylor series as:

$$\Phi(\mathbf{x}) = \Phi(0) + \sum_i \frac{\partial \Phi}{\partial x_i} + \frac{1}{2} \sum_{i,j} \frac{\partial^2 \Phi}{\partial x_i \partial x_j} x^i x^j + \cdots \tag{2.16}$$

$$A_i(\mathbf{x}) = A_i(0) + \sum_j \frac{\partial A_i}{\partial x_j} x_j + \cdots \tag{2.17}$$

Thus the hyperfine interaction energy can be split as follows

$$E = E_{E0} + E_{M0} + E_{E1} + E_{M1} + E_{E2} + \cdots \tag{2.18}$$

with

$$E_{E0} = \Phi(0) \int \rho(\mathbf{x}) \mathrm{d}^3x = Ze\Phi(0) \tag{2.19}$$

$$E_{M0} = \mathbf{A}(0) \cdot \int \mathbf{j}(\mathbf{x}) \mathrm{d}^3x = 0 \tag{2.20}$$

$$E_{E1} = \sum_i \frac{\partial \Phi}{\partial x_i} \int x_i \rho(\mathbf{x}) \mathrm{d}^3x = 0 \tag{2.21}$$

$$E_{M1} = \sum_{i,j} \frac{\partial A_i}{\partial x_j} \int x_j j_j(\mathbf{x}) \mathrm{d}^3x = -\mathbf{B}(0) \cdot \int \mathbf{x} \times \mathbf{j}(\mathbf{x}) \mathrm{d}^3x \tag{2.22}$$

$$E_{E2} = \frac{1}{2} \sum_{i,j} \frac{\partial^2 \Phi}{\partial x_i \partial x_j} \int x^i x^j \rho(\mathbf{x}) \mathrm{d}^3x \tag{2.23}$$

E_{E0} just describes the total charge of the nucleus, which is equal for both states involved in a Mössbauer transition, so it is of no interest for Mössbauer spectroscopy. E_{M0} vanishes because $\nabla \cdot \mathbf{j} = 0$ for a stationary current distribution, and E_{E1} vanishes, because nuclei do not have a stationary electrical dipole moment (Wegener 1966). So only E_{M1} and E_{E2} remain, which describe the magnetic dipole interaction, the isomer shift and the electric quadrupole interaction.

2.4.1 Electric Interaction

Equation 2.23 can be split into two parts with the help of the identity

$$x^i x^j = \frac{1}{3} r^2 \delta^{ij} + \frac{1}{3} \left(3x^i x^j - r^2 \delta^{ij} \right) \tag{2.24}$$

and the Poisson Equation

$$\sum_i \frac{\partial^2 \Phi}{\partial x_i^2} = -\frac{\rho_e(0)}{\epsilon_0} = \frac{e}{\epsilon_0} \left| \Psi_e(0) \right|^2 . \tag{2.25}$$

The first term in Equation 2.23 yields

$$E_I = \frac{e}{6\epsilon_0} \left| \Psi_e(0) \right|^2 \int r^2 \rho(\mathbf{x}) d^3x = \frac{Ze^2}{6\epsilon_0} \left| \Psi_e(0) \right|^2 \langle r^2 \rangle \tag{2.26}$$

and the second term

$$E_Q = \frac{1}{6} \sum_{i,j} \frac{\partial^2 \Phi}{\partial x_i \partial x_j} \int (3x^i x^j - r^2 \delta^{ij}) \rho(\mathbf{x}) \mathrm{d}^3x =: \frac{1}{6} \sum_{i,j} \frac{\partial^2 \Phi}{\partial x_i \partial x_j} Q^{ij} . \tag{2.27}$$

Here $\langle r^2 \rangle$ is the mean squared nuclear charge radius and Q^{ij} is the traceless tensor of the nuclear quadrupole moment.

The energy shift E_I of the individual states of the nucleus leads to the so called isomer shift IS: If the mean square nuclear charge radii of the first excited state and the ground state are different, i.e. $\langle r^2 \rangle_e - \langle r^2 \rangle_g \equiv \Delta \langle r^2 \rangle \neq 0$, and if furthermore the electron density at the site of the nucleus in the source, $\left| \Psi_S(0) \right|^2$ is different from the electron density in the absorber $\left| \Psi_A(0) \right|^2$, then source and absorber have to be moved with a velocity

$$IS = \frac{Ze^2 c}{6\epsilon_0 E_0} \left(\left| \Psi_A(0) \right|^2 - \left| \Psi_S(0) \right|^2 \right) \Delta \langle r^2 \rangle \tag{2.28}$$

towards each other to get resonant absorption in the absence of a hyperfine splitting (see below). For example, the isomer shift IS of gold in a metallic gold absorber against the gold in the metallic platinum matrix in the source is $IS = -1.23\,\mathrm{mm/s}$. The electron density at the site of the nucleus is thereby mainly determined by the chemical bonding in the crystal.

Since the tensor Q^{ij} of the quadrupole moment is traceless, one can rewrite Equation 2.27 as

$$E_Q = \frac{e}{6} \sum_{i,j} V_{ij} Q^{ij} \tag{2.29}$$

with the tensor of the electric field gradient

$$V_{ij} = \frac{\partial^2 \Psi}{\partial x_i \partial x_j} - \frac{1}{3} \Delta \Psi \delta_{ij}. \tag{2.30}$$

Diagonalisation by transformation to principle axes leads to a electric field gradient which is fully described by only two parameters V_{zz} and $\eta \equiv (V_{xx} - V_{yy})/V_{zz}$. By convention, the coordinate axes are chosen so that $|V_{zz}| \geq |V_{yy}| \geq |V_{zz}|$. The asymmetry parameter η then only assumes values between 0 and 1. The matrix elements of V_{ij} are then

$$V_{2,0} = \frac{3}{\sqrt{6}} V_{zz} \tag{2.31}$$

$$V_{2,\pm 1} = 0 \tag{2.32}$$

$$V_{2,\pm 2} = \frac{1}{2} \eta V_{zz}. \tag{2.33}$$

In the case of an axially symmetric field, where $V_{xx} = V_{yy} \neq V_{zz}$ and thus $\eta = 0$, one gets a splitting of a nuclear state with spin $I \geq 1$ and the possible magnetic quantum number $m = I, I-1, \ldots, -I$:

$$E_Q(m) = \frac{eQV_{zz}}{4} \frac{3m^2 - I(I+1)}{I(2I-1)}. \tag{2.34}$$

The electric quadrupole moment of the nucleus is defined as

$$Q := \frac{1}{e} \langle I, m = I | Q^{zz} | I, m = I \rangle. \tag{2.35}$$

The electric quadrupole splitting of the nuclear energy levels with spin 1/2 and 3/2, where only the $I = 3/2$ splits, are given in Figure 2.4 (left). The influence of the isomer shift and quadrupole splitting on the Mössbauer spectrum in the case of a transition between nuclear states with spin 1/2 and 3/2 are shown in Figure 2.5. Conventionally the count rate out of resonance is set to 100%.

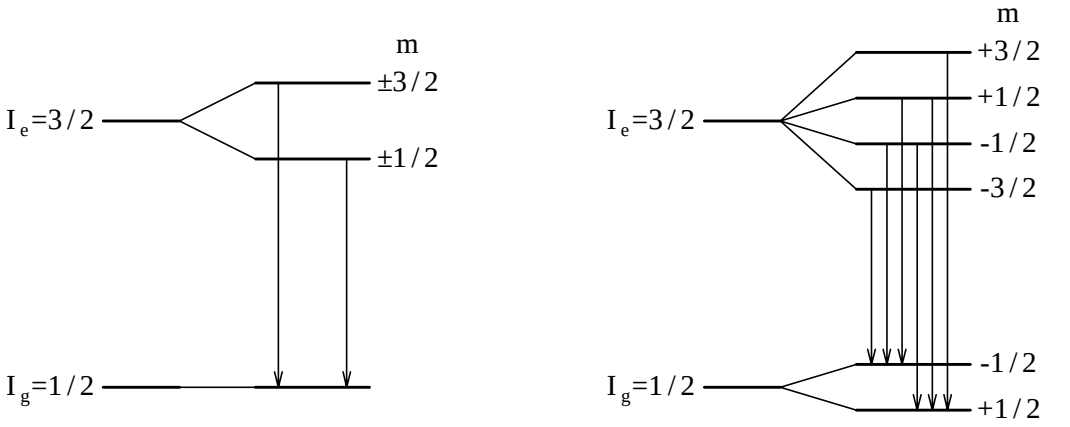

Fig. 2.4: Nuclear energy levels in case of an electric quadrupole splitting (left) or a magnetic dipole splitting (right) for ^{57}Fe.

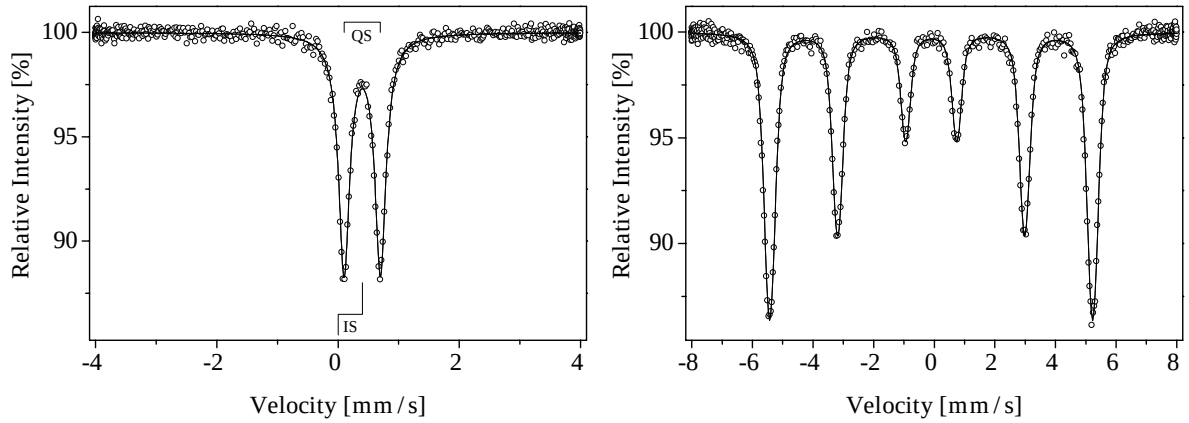

Fig. 2.5: Simulated Mössbauer spectra exhibiting lorentzian line shape, an isomer shift, and an electric quadrupole splitting (left) or magnetic dipole splitting (right).

2.4.2 Magnetic Dipole Interaction

Position of Lines

Equation 2.22 describes the magnetic dipole interaction and can be rewritten as

$$E_{M1} = -\sum_i B_i \mu_i \qquad \text{with} \qquad \boldsymbol{\mu} = \int \mathbf{x} \times \mathbf{j}(\mathbf{x}) \mathrm{d}^3 x, \tag{2.36}$$

where $\boldsymbol{\mu}$ is the magnetic moment of the nucleus and $\mathbf{B}$ is the magnetic field produced by the electrons in a magnetically ordered material. In case where the electric quadrupole interaction vanishes it is preferable to choose the coordinates so that $B_x = B_y = 0$. This leads to a splitting of the energy of a nuclear state with spin I into energy levels at

$$E_M = -\frac{\mu m}{I} B, \tag{2.37}$$

which is the well known Zeemann splitting. In this study magnetic hyperfine splittings are observed only for ^{57}Fe. For the $3/2 \rightarrow 1/2$ transition of ^{57}Fe the $I = 1/2$ groundstate splits into two ($m = \pm 1/2$) substates, while the 14.4 keV state with $I = 3/2$ splits into 4 (c.f. Figure 2.4). As a consequence, the Mössbauer resonance splits into 8 transitions, of which only 6 are allowed, since the Mössbauer resonance is a $M1$ transition for which transitions with $|\Delta m| > 1$ are forbidden. For illustration a magnetic splitting is shown in Figure 2.5 (right). If there is also an electric field gradient $V_{zz} \neq 0$ the complete Hamiltonian has to be diagonalised. Only in the case where $eQV_{zz} \ll \boldsymbol{\mu}\mathbf{B}$ can one handle the electric quadrupole interaction as a perturbation of the magnetic interaction. In the first approximation the eigen functions are those of the pure magnetic case. The energy levels will become

$$E_M = -\frac{\mu m}{I} B + \frac{eQV'_{zz}}{4} \frac{3m^2 - I(I+1)}{I(2I-1)}. \tag{2.38}$$

Here V'_{zz} is the z-component of the field gradient in the direction of the magnetic field. Expressed as a function of V_{zz} and η, V'_{zz} can be written as

$$V'_{zz} = \frac{3\cos^2\theta - 1 + \eta\cos(2\phi)\sin^2\theta}{2} V_{zz}, \tag{2.39}$$

where θ and ϕ are the polar and azimuthal angle of the magnetic field vector in the principal axes system of the electric field gradient.

Relative Line Intensities

Given the magnetic splitting of the resonant line, the relative intensities of the six lines can be calculated from the interaction of the nucleus with the electromagnetic radiation field of the γ-ray, taking into account the direction and polarisation of the radiation (Wegener 1966). Here only the results for the possible transitions in the case of iron are given in Table 2.2.

Tab. 2.2: Relative probabilities for transitions between the torque eigenvalues $|I, m\rangle$ for the isotope ^{57}Fe. Shown are the relative intensities for unpolarised incident radiation and single crystals, samples with a prefered orientation of the hyperfine field (for example surface magnetisation) and powder samples (which includes alloys). θ is the angle between the $\mathbf{k}$-vector of the resonant radiation and the magnetic hyperfine field.

Transition	Single crystal	Sample with texture	Powder
$-3/2 \rightarrow -1/2$	3	3	3
$-1/2 \rightarrow -1/2$	$4 \cdot \frac{1-\cos^2\theta}{1+\cos^2\theta}$	$4 \cdot \frac{1-\langle\cos^2\theta\rangle}{1+\langle\cos^2\theta\rangle}$	2
$-1/2 \rightarrow +1/2$	1	1	1
$+1/2 \rightarrow -1/2$	1	1	1
$+1/2 \rightarrow +1/2$	$4 \cdot \frac{1-\cos^2\theta}{1+\cos^2\theta}$	$4 \cdot \frac{1-\langle\cos^2\theta\rangle}{1+\langle\cos^2\theta\rangle}$	2
$+3/2 \rightarrow +1/2$	3	3	3

In this chapter possible phenomena were described from a general point of view. More detailed descriptions for special cases will be given where necessary for understanding the measured Mössbauer spectra.

3 Mössbauer Spectroscopy in Transmission Mode

3.1 Introduction

This chapter describes the usual experimental set-up in Mössbauer spectroscopy. In the following chapters, this description will serve as the basis for the more special cases of backscattering experiments and CEMS. Moreover the standard transmission geometry was used for the measurements on reference materials. The measurements on reference materials are important for instance for finding out the proper hyperfine parameters for special materials and phases in the original materials. The production of sources will be also described in this chapter.

3.2 Source Preparation

The source isotope used for the gold measurements was ^{197}Pt, which decays via a β^- decay to ^{197}Au. The ^{197}Pt was obtained by neutron activation in the Munich research reactor FRM. 200 mg of metallic platinum enriched in ^{196}Pt up to 96% were irradiated as discs with a diameter of 8 mm in a thermal neutron flux of about $2 \cdot 10^{13}\,\mathrm{cm^{-2}s^{-1}}$ for two days. With the resulting starting activity of $2 \cdot 10^9$ to $4 \cdot 10^9$ Bq of ^{197}Pt and a half life of 18.3 h such sources can be used for three or four days before they need to be irradiated again.

In the β^- decay of the ^{197}Pt, ^{197}Au is formed and accumulates in the source when the sources are frequently re-irradiated. The re-irradiation is, however, necessary because of the high price of enriched ^{196}Pt. By neutron activation of the radiogenic ^{197}Au, ^{198}Au is formed, which decays to mercury ^{198}Hg. In detail the following reactions take place:

$$^{196}\mathrm{Pt} + \mathrm{n} \longrightarrow {}^{197}\mathrm{Pt} \tag{3.1}$$

$$^{197}\mathrm{Pt} \xrightarrow{18.3\,\mathrm{h}} {}^{197}\mathrm{Au}^* + e^- + \overline{\nu}_e \tag{3.2}$$

$$^{197}\mathrm{Au}^* \longrightarrow {}^{197}\mathrm{Au} + \gamma_{77.3\,\mathrm{keV}} \tag{3.3}$$

$$^{197}\mathrm{Au} + \mathrm{n} \longrightarrow {}^{198m}\mathrm{Au} \xrightarrow{2.30\,\mathrm{d}} {}^{198}\mathrm{Au} + \gamma_{215\,\mathrm{keV}} \tag{3.4}$$

$$^{198}\mathrm{Au} \xrightarrow{2.69\,\mathrm{d}} {}^{198}\mathrm{Hg}^{*} + e^{-} + \overline{\nu}_{e} \tag{3.5}$$

$$^{198}\mathrm{Hg}^{*} \longrightarrow {}^{198}\mathrm{Hg} + \gamma_{412\,\mathrm{keV}} \tag{3.6}$$

For normal transmission experiments, the radiochemical impurities are not disturbing at all. In scattering experiments, however, they may lead to a disturbing backround of X-rays and Compton scattering. Since the half lives of the radioactive impurities are longer than that for the decay leading to the emission of the Mössbauer γ-rays it is preferable to use the fresh sources and avoid long measurement times with one source since the relative intensities of the backround radiation increases when the ^{197}Pt activity decays. This is of particular importance in the CEMS and backscattering mode, where the high energy events produce photo electrons and Compton scattered γ-rays respectively.

The sources are put into small lucite capsules and mounted in tantalum source holders, with an opening facing forward. Tantalum is particularly well suited for shielding the 77.3 keV γ-rays, since its K-absorption edge is below the γ-ray energy ($E_K = 67.4\,\mathrm{keV}$) and Ta metal is relatively cheap and easily machinable.

Since the emission of the Mössbauer γ-rays takes place in the cubic lattice of fcc Pt metal, which is not magnetic, one obtains a single line emission spectrum. All isomer shifts given in this work are reported with respect to the platinum metal source.

The sources for ^{119}Sn Mössbauer spectroscopy are produced by neutron activation of ^{118}Sn, yielding the long lived ^{119m}Sn in the second excited state with spin $11/2^{-}$. The second excited state decays with a half life of 250 days into the first excited $I = 3/2^{-}$state by a highly converted $M4$ transission. The Mössbauer radiation, with an energy of 23.9 keV, is emitted after the decay of the first excited state with a life time of 25.8 ns. For obtaining a single line source the ^{119}Sn is usually used in a $CaSnO_3$ matrix. Due to the small neutron capture cross section of ^{118}Sn of $\sigma = 0.016$ b and the long half life of the second excited state, the ^{118}Sn isotope has to be irradiated for a long time in a high neutron flux to obtain sufficiently strong sources. The sources are usually produced in research reactors in USA or Russia and are commercially available, for example, from Amersham Ltd or Chemo Trade Ltd. Typical initial activities are $5.5 \cdot 10^{8}$ Bq.

The source isotope for the ^{57}Fe Mössbauer spectroscopy is ^{57}Co, which is obtained, for instance, by proton irradiation of ^{58}Ni in a cyclotron, by the (p,2p) reaction. The ^{57}Co is then chemically separated from the target material and inevaporated into an appropriate matrix for use as a Mössbauer source. The sources used in this study were ^{57}Co in a rhodium matrix. The ^{57}Co decays to the second excited state of ^{57}Fe by K electron capture. The first excited state is reached, with an 8.6 ns half life and emission of a 123 keV γ-ray. The Mössbauer radiation of 14.4 keV energy is emitted with a life time of 141 ns. Like the tin sources, the iron sources are commercially available. The sources used in this work had an initial activity of $1.8 \cdot 10^{9}$ Bq. This sources can be used for several years.

3.3 The Thin Absorber Limit

As mentioned above, the density of the Mössbauer nuclei has to be sufficiently low in transmission experiments in order to avoid saturation effects. Actual thicknesses depend on the Mössbauer isotope and the temperature of the measurement, which influences the Lamb-Mössbauer factor.

In section 2.3 it was noted that an absorber can be considered as thin if, for a single line absorber, the effective thickness $t = n \cdot f_A \cdot z_A \cdot \sigma_0 \ll 1$. Then the lines in the Mössbauer pattern can be fitted with a lorentzian line shape, with a width of 2Γ, where $\Gamma = \hbar/\tau$ is the resonance width in both the source and the absorber. This is true in the absence of broadening effects arising from hyperfine interactions. The inhomogeneous broadening of the Mössbauer line can than often be described by a distribution of line positions. A simple distribution of line positions that is often a good approximation, is a gaussian distribution of the lorentzian resonance lines. Such lineshapes are called Voigt-profiles. They are frequently used in fitting routines. Generally the resonant cross section takes the form

$$\sigma(E) = \sigma_0 \int_0^\infty \rho(E_0) \frac{(\Gamma/2)^2}{(E - E_0)^2 + (\Gamma/2)^2} \mathrm{d}E_0, \tag{3.7}$$

with the normalization of the distribution function $\rho(E_0)$

$$\int_0^\infty \rho(E_0) \mathrm{d}E_0 = 1. \tag{3.8}$$

If $\rho(E_0)$ is a gaussian distribution, one has

$$\rho(E_0) = \frac{1}{\sqrt{2\pi}\sigma} \exp \frac{(E_0 - E)^2}{2\sigma^2}. \tag{3.9}$$

Here σ is the gaussian width or variance of the distribution.

3.4 Experimental Set-up

Figures 3.1 and 3.2 schematically show two Mössbauer spectrometer. Sources are mounted on the axis of a velocity drive, which works in principle like a loudspeaker system. The drives used in this work correspond in their properties to the MA-250 type velocity drive systems of FAST Comtec GmbH. The γ-radiation emitted by the source is collimated onto the sample, which should be homogeneous and without holes. The sample area is usually 1 or 2 cm^2. The detector is located behind the sample.

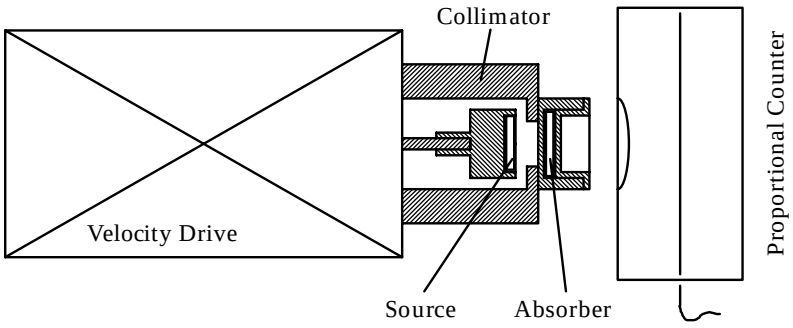

Fig. 3.1: Transmission Mössbauer spectrometer for measurements at room temperature.

Figure 3.2 shows a liquid helium bath cryostat, where source and sample are kept in liquid helium at a temperature of 4.2 K. Due to the low f-factor of ^{197}Au, all gold measurements were done in such cryostats. The sample is mounted in the drive tip and can be taken out from the cryostat together with the drive, even when there is liquid helium in the inner tank. To keep helium evaporation as small as possible an outer tank contains liquid nitrogen as a shield against heat radiation. The shield is automatically refilled with liquid nitrogen from a reservoir tank, while helium is refilled manually. Such cryostats work for about two to three days with one filling of helium. To change the sample one has to pre-cool the drive tip in liquid nitrogen before inserting it into the cryostat. The evaporated helium is collected in a helium recovery system and liquefied again.

Figure 3.3 gives a scheme of the electronic set-up for the collection of Mössbauer spectra.

The function generator (FG-2 from Halder Electronics) supplies an analog, sinusoidal output signal for the drive controller and correlated channel advance pulses for the multichannel storage device. One full period of the drive motion is usually divided in 512 or 1024 intervals, which is the number of channels in the multichannel storage device. After a full period of the oscillation one starts again with channel number 0.

The drive controller (MR-250 Halder Electronics) regulates the sinusoidal motion of the drive, based on the input from the function generator. The drive is calibrated using the well known magnetic hyperfine splitting of α-iron at room temperature. Since the alternating voltage induced in the pick up coil is directly proportional to the velocity, different maximum velocities can be realized by changing to the reference voltage, which is measured with a rms voltmeter.

For the detection of the 77.3 keV γ-ray of the ^{197}Au one uses a germanium semiconductor detector (IGP 705 Princton Gamma-Tech) with a transistor reset FET preamplifier. For the 14.4 keV γ-ray of the ^{57}Fe a gas proportional counter filled with krypton as the counter gas is used. The same counter can be used for the 23.9 keV Mössbauer radiation of ^{119m}Sn. An alternative for ^{119m}Sn is a scintilation detector, which has the advantage of having a higher detection efficiency.

The pulse amplification is done by a Ortec 440A linear amplifier with an amplifi-

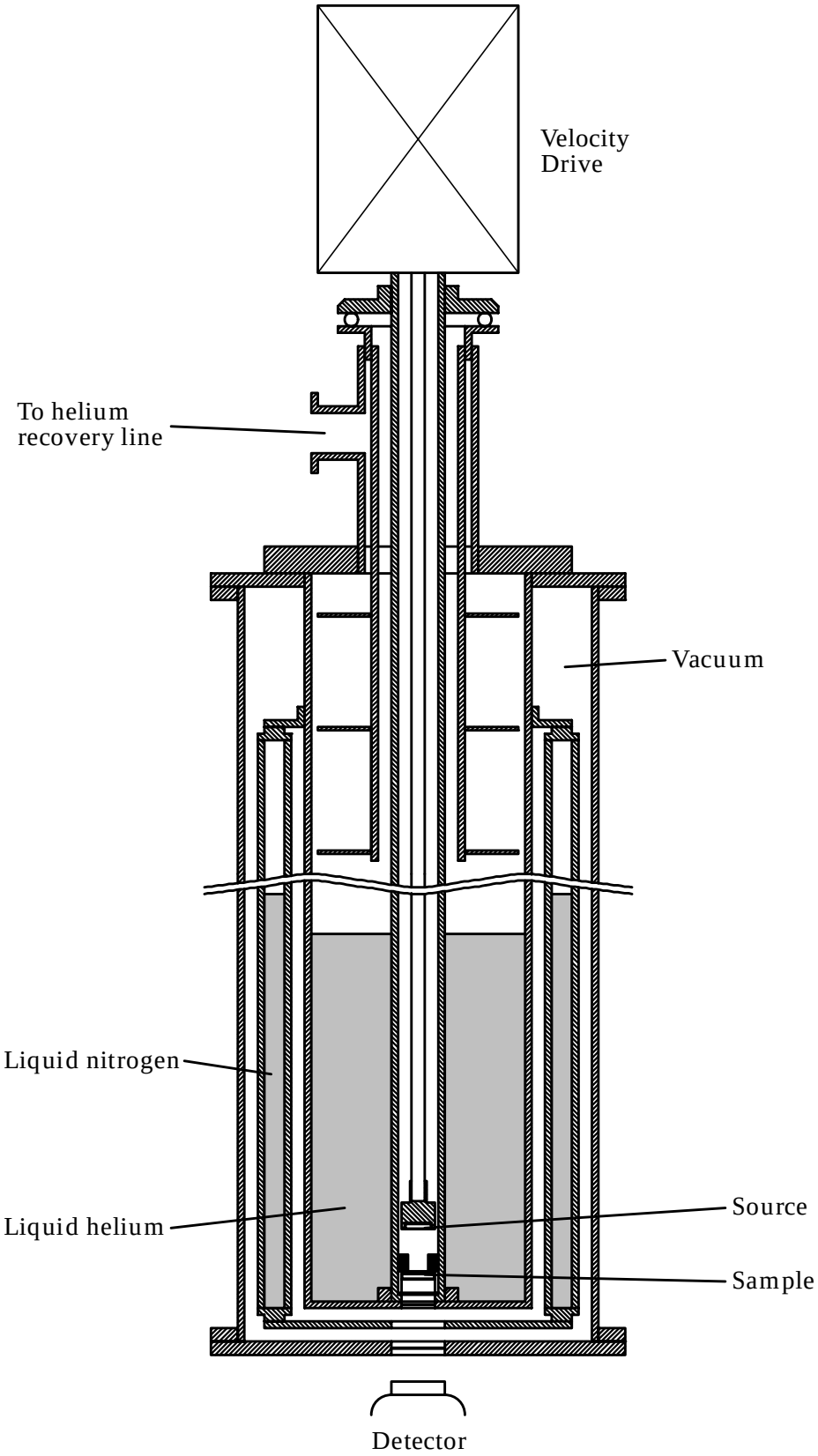

Fig. 3.2: Helium bath cryostat for transmission Mössbauer spectroscopy. Both source and sample are kept at 4.2 K.

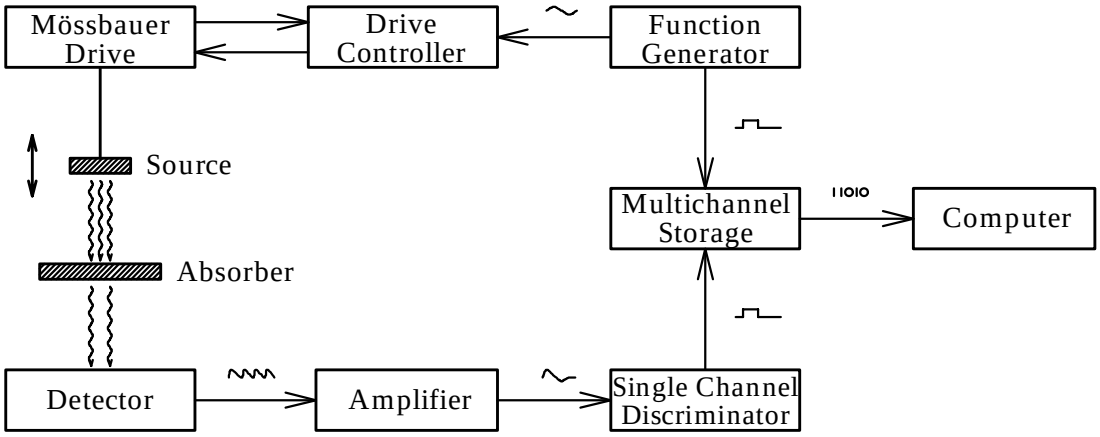

Fig. 3.3: Schematic Figure of the electronic set-up of a Mössbauer spectrometer.

cation factor of 350 and a typical shaping time of 0.5 μs. From the bipolar output of the main amplifier the single channel analyser (Timing SCA-102 Halder Electronics) selects the events lying in the pulse height window corresponding to the energy of the Mössbauer γ-ray. The counts in this energy window are then added to the contents of the momentarily open channel (which is corresponding to the momentary velocity of the drive) of the multichannel storage device (MCA-2 Halder Electronics). At the end of the measurement the contents of the multichannel storage device can be read out to a computer. Equivalent electronics are commercially available from FAST Comtec, Munich.

Theoretical curves corresponding to the adjustable hyperfine parameters are fitted to the measured spectra with the program Mos90 by Große (1992), which is available from FAST Comtec, Munich, as PCMOSII.

4 Conversion Electron Mössbauer Spectroscopy

4.1 Introduction

Conversion electron Mössbauer spectroscopy (CEMS) is a most surface sensitive method in Mössbauer spectroscopy with a probing depth equal to the range of the conversion electrons in the sample material. The conversion electrons are emitted from the atom in which the Mössbauer absorption takes place instead of the reemission of a γ-quantum. The conversion coefficient α gives the probability of a conversion process compared to the probability for gamma emission. Internal conversion is possible from all shells of the atom for which the binding energies are lower than the γ-ray energy. Different conversion coefficients for the individual shells and subshells describe the respective probabilities (Rose 1955). In internal conversion the energy of the transition energy of the nucleus is transferred to an electron from the atomic shell. The kinetic energy of the emitted electron is thus the energy of the Mössbauer transition minus the bonding energy of the respective electron. Since conversion only takes place after a Mössbauer absorption process the detection of conversion electrons is suitable good for detecting the Mössbauer absorption. That is, when the source is at resonance with the sample, the countrate in a counter detecting the conversion electrons increases.

The use of conversion electrons for the detection of the Mössbauer resonant absorption dates back to 1964, when Levy *et al.* (1964) published the application of a scintillation detector to CEMS measurements of ^{119}Sn. The same Mössbauer isotope was used by Bonchev *et al.* (1969) for DCEMS, a depth sensitive kind of CEMS using a detector system with high energy resolution. For CEMS measurements on ^{57}Fe Swanson and Spijkerman (1970) used a gas proportional counter at roomtemperature. Five years later Isozumi and Takafuchi (1975) and Sawicki *et al.* (1976) developed proportional counters for CEMS at low temperatures down to 77 K. Isozumi et al. (1987) operated their gas proportional counter also at 5 K, while Sawicki *et al.* (1981) startet to use a channeltron for the detection of the conversion electrons, which could also be cooled down to liquid helium temperature. Sawicki *et al.* (1983) also reported first CEMS measurements of ^{197}Au with a channeltron.

In this work as a detector for the conversion electrons a gas proportional counter was used.

4.2 Iron CEMS at Room Temperature

The experimental set-up varies for different purposes and Mössbauer isotopes. Figure 4.1 shows the CEMS set-up for ^{57}Fe at room temperature. In the case of ^{57}Fe the conversion electrons have an energy of 7.3 keV and $\sim$ 13.7 keV, from the K-shell and the L-shell, respectively (compare Table 2.1). Due to this low energy, the sample has to be mounted in the proportional chamber since the electrons could not pass through an entrance window. The drive unit stands on the counter chamber, which is 8 cm long and 2 cm broad. The counter wire is a gold-plated tungsten wire with 20 μm diameter. The counter gas is a mixture of He and 4% CH_4, where the methane is working as a quenching gas. The γ-radiation from the source falls through the counter gas without significant absorption onto the sample, while a conversion electron leaving the surface of the sample ionisizes the counter gas (primary ionisation). It is necessary to wash the counter chamber constantly in order to avoid contamination by oxygen or water vapour. The gas flow is controlled by a pressure regulator and a needle valve after the counter chamber, which lets the gas pass into a washing flask, filled with water or oil. The gas flux is set to about 3 bubbles per minute.

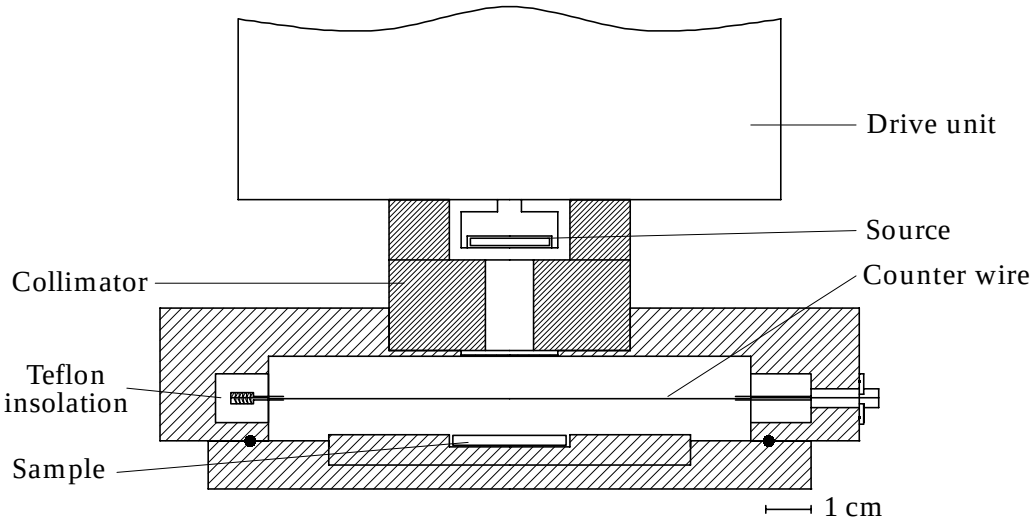

Fig. 4.1: Schematic view of a spectrometer for iron CEMS.

The preamplifier is mounted directly outside the chamber. The rest of the set-up corresponds to that for transmission mode. For the main amplifier an amplification of 135 at a shaping time of 1 μs was used for a high voltage of 1200 V. The output of the main amplifier can be fed into an analog-to-digital converter (ADC) to measure the pulse height spectrum with a multichannel analyzer, which gives the energy distribution of the electrons and photo electrons emitted from the sample. The photo electrons have the same energy like the conversion electrons from the according shell. So it can not be distinguished between photo electrons and conversion electrons. Figure 4.2 shows the pulse height spectrum from a pure ^{57}Fe-foil.

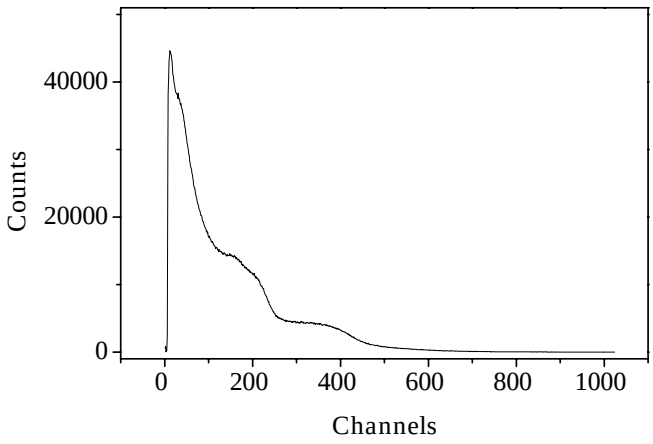

Fig. 4.2: Pulse height spectrum of the electrons emitted from a metallic ^{57}Fe sample.

Using a sample of isotopically enriched metallic ^{57}Fe for taking an energy spectrum of the electrons helps to decide where to set the window of the single channel analyzer, since photo electrons from other elements do not disturb the energy spectrum. Another possibility is to use a sample of stainless steel, enriched in ^{57}Fe. Stainless steel has a non-resolved doublet Mössbauer pattern with an isomer shift close to 0 (Figure 4.3).

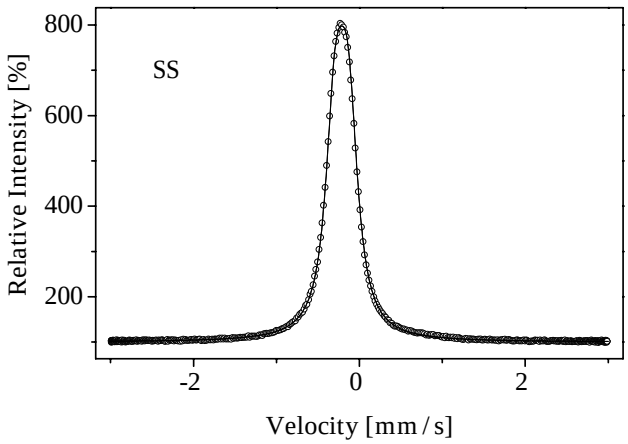

Fig. 4.3: Mössbauer pattern of stainless steel ($Fe_{55}Cr_{26}Ni_{19}$) enriched in ^{57}Fe.

If one takes a pulse height spectrum while running the Mössbauer spectrometer with a small maximum velocity of 0.2 mm/s only, the stainless steel sample will be in resonance with the source most of the time. So one gets mostly conversion electrons and only relatively few photo electrons in the pulse height spectrum. If the Mössbauer spectrometer is run at a large maximum velocity of, for example 20 mm/s the sample will be out of resonance most of the time and one gets mostly photo electrons in the pulse height spectrum. The difference of the two pulse height spectra are the conversion electrons and also Auger electrons. The Auger electrons are emitted after the internal conversion by transferring the energy of a subsequent X-ray transition directly to an electron. The Auger electrons are thus also emitted after a Mössbauer absorption pro-

cess. The pulse height spectra of stainless steel in and out of resonance are shown in Figure 4.4.

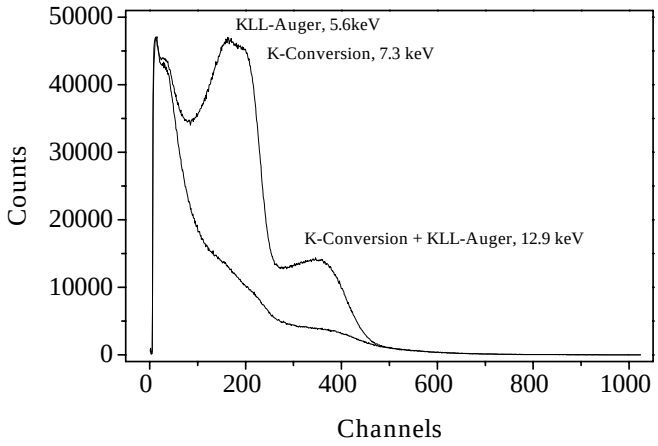

Fig. 4.4: Pulse height of electrons emitted from stainless steel, according to the Mössbauer spectrum in Figure 4.3, in and out of resonance.

In order to get a reasonable countrate in the window of the single channel analyzer one usually sets the lower level of the window just between the electronic noise and the KLL-Auger electrons at 5.6 keV, while the upper limit is set to the upper end of the pulse height spectrum. In this way one uses all events with an energy higher than about 3.5 keV for measuring the Mössbauer spectra. The countrate depends strongly on the ratio of ^{57}Fe to other elements and isotopes including ^{56}Fe. Usual countrates lie between about 1000 s^{-1} and over 10000 s^{-1} in the presence of heavy elements like gold, which contributes much to the photo electron noise.

4.3 Tin CEMS at Room Temperature

The set-up for iron CEMS can also be used for the Mössbauer isotope ^{119}Sn. Figure 4.5 shows the pulse height spectra of conversion electrons from tin dioxide, SnO_2. The Mössbauer spectrum of tin dioxide is a hardly resolved doublet near zero velocity, see Figure 4.6. One can therefore again measure the pulse height spectra of the conversion electrons with zero velocity and a large maximum velocity of, for example 20 mm/s to render the contribution of the conversion electrons visible in the pulse height spectra.

From Figure 4.5 one sees that the energy resolution is not as good as in the case of iron. This can be explained by the higher energy of the conversion electrons of ^{119}Sn, which is $E_\gamma - E_B = 19.4$ keV for the L_I-shell. The range of such electrons in the He counter gas is about 4 cm (c.f. Figure 4.7) and thus larger than the dimensions of the chamber, so that the electrons do not deposit their whole energy in the counter chamber through primary ionisation. The structure in the pulse height spectra in Figure 4.5 thus reflects only the dimensions of the counter chamber. The longer the path of the electrons

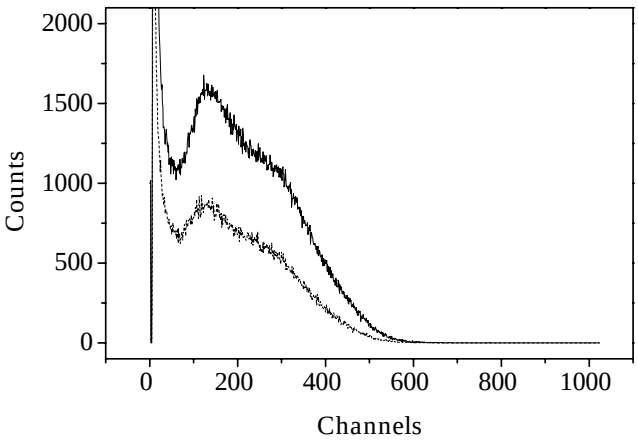

Fig. 4.5: Pulse height spectra of electrons emitted from a SnO_2 sample in and out of resonance.

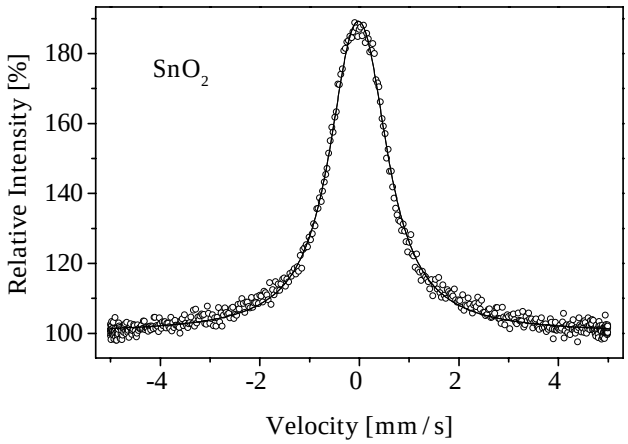

Fig. 4.6: Mössbauer pattern of SnO_2.

in the chamber before coming across the wall, the higher is the primary ionisation of the chamber. The first peak near channel 130 are electrons, which hit the wall opposite of the sample, while the peak near channel 300 are electrons, which go lengthwise the counter wire. However one will still get a Mössbauer spectrum by setting the lower level of the single channel analyzer just above the noise level.

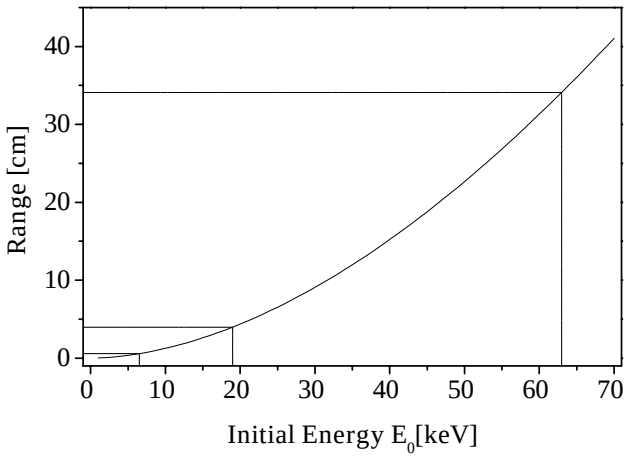

Fig. 4.7: Range (stretched trajectory) of electrons in He at normal conditions, calculated by integration $R = \int_{E_0}^{0} \frac{1}{\mathrm{d}E/\mathrm{d}s}\mathrm{d}E$, with $\mathrm{d}E/\mathrm{d}s$ according to Equation 4.10.

4.4 Gold CEMS at Liquid Helium Temperature

Due to the low f-factor of gold the source and the sample have to be kept at low temperatures. This means that the drive tip and the counter chamber for the detection of the conversion electrons should be mounted in liquid helium. Figure 4.8 shows the set-up of the cryostat for gold CEMS used in this work.

The counter chamber is filled with pure He as the counter gas. Since all other gases would freeze out at 4.2 K, one cannot add any quenching gas. He clusters are supposed to take over the function of the quenching gas (Kishimoto *et al.* 1987 and 1990, Isozumi *et al.* 1987 and 1989). After mounting the sample in the counter chamber and placing the container for the counter chamber into the liquid helium vessel of the cryostat (at room temperature), the counter chamber is connected to the gas handling system, which includes a gasreservoir with the same volume as the counter chamber. After evacuating the counter chamber and gas reservoir and filling it with He gas from a steel cylinder at least three times, the counter and the gas reservoir are filled with 1 bar of He. Then the cryostat is cooled down by first filling liquid nitrogen into the nitrogen tank. It then takes roughly two days for the inner parts of the cryostat to reach a temperature of around 100 K. When the counter chamber cools down, gas from the external gas reservoir enters the counter chamber. The pressure in the system falls below the initial one of 1 bar. After mounting the drive with a fresh source on top of the counter chamber, liquid helium is filled into the helium vessel of the cryostat, which takes about 20 minutes. Nearly all the He gas that had initially been in external reservoir will now be in the counter chamber so that at 4.2 K the helium gas in the counter chamber has about twice the density ($\rho_{\mathrm{He}} = 0.357\,\mathrm{mg/cm^3}$) of helium at 1 bar and 300 K, at a pressure of only about 28 mbar.

Due to the construction of the cryostat it is not possible to have the preamplifier less than half a meter from the counter chamber and the connection wire is therefore a source

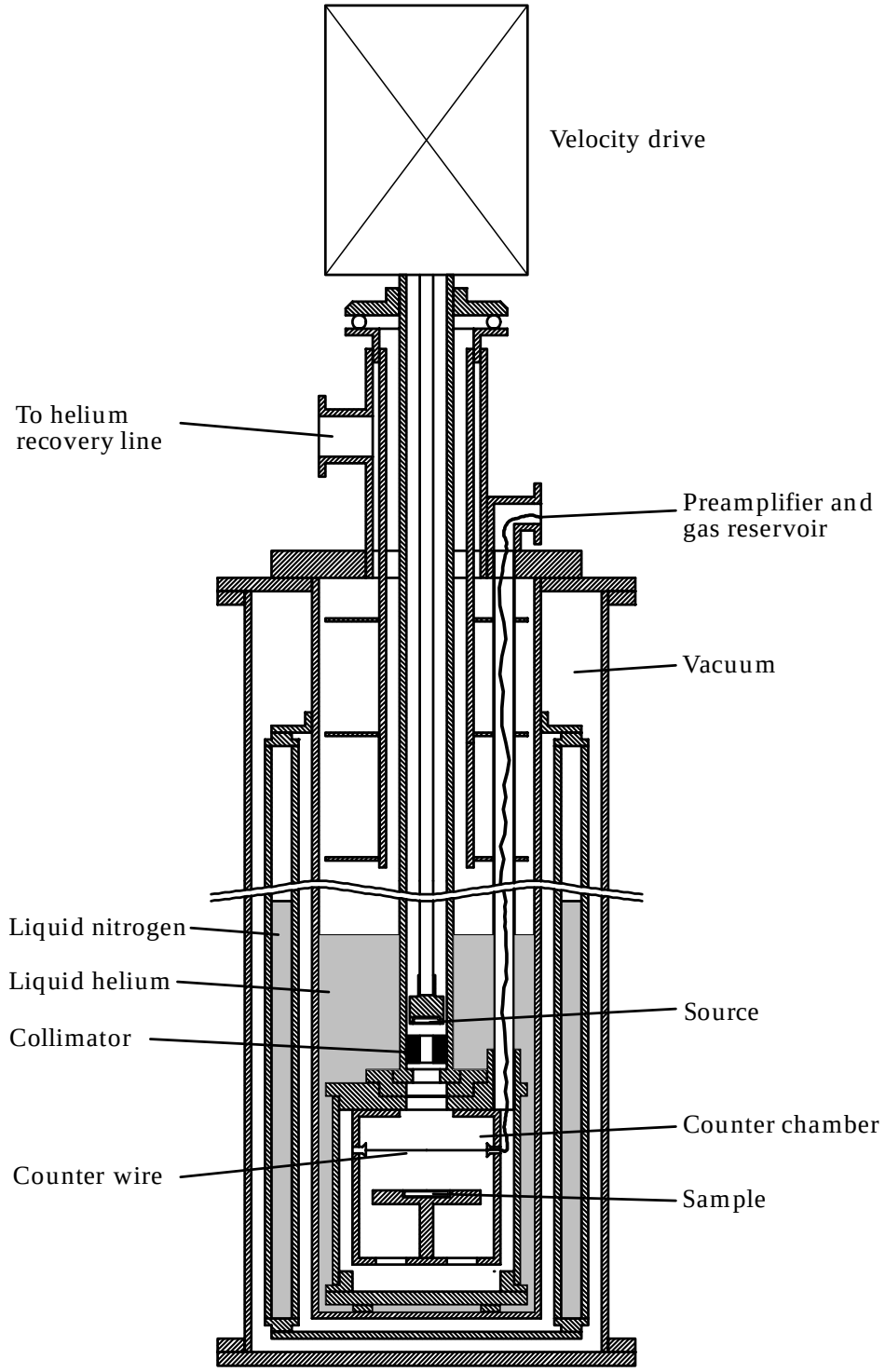

Fig. 4.8: Schematic view of a cryostat for CEMS with ^{197}Au.

of severe microphonic noise. It is necessary to protect the cryostat from electromagnetic waves and mechanical vibrations. One therefore should, for example, disconnect the cryostat completely from the vacuum pump for the time of measurement.

The signal from the proportional counter is processed by a MOSFET preamplifier (Canberra 2003) and a main amplifier (Canberra 2021) set to a shaping time of 12 μs and an amplification factor of 3000, when the detector is operated at a high voltage of 1200 V.

Since the detector is operated with pure He gas, the quenching is poor and the detector is susceptible to breakthrough and discharging. Once discharging has started, it can only be stopped by reduction of the high voltage. A safe permanent operation was only possible at a high voltage of about 1200 V. The gas amplification is then between about 50 and 100 (Regen 1994). The sensitivity to discharge was also found to depend on the count rate. The maximum sustainable count rate above the noise level was found to be about 600 s^{-1}, irrespective of the source strength. When the sources had been in use for two days the high voltage could, for instance, be increased to 1300 V. The count rate above the noise level then increased again to that obtained with the new source. It also turned out that conditioning the detector by provoking discharge after mounting a new source has a beneficial influence on further operation. To this end, the high voltage is increased until breakthrough occurs. It is then reduced again until the discharge stopped and then set to a reasonable value.

The pulse height spectrum does not show any significant structure because the range of the 63 keV L conversion electrons of the gold deposit only a fraction of their energy in the detector chamber (c.f. Figure 4.7). The range in He at the density used in the detector is about 17 cm, which is about three times the height or diameter (6 cm each) of the counter chamber. Thus the information about the energy of the electrons emerging from the target is largely lost in the insufficient primary ionisation of the counter gas. Figure 4.9 shows the pulse height spectrum in and out of resonance measured with a $Au_{70}Cu_{30}$ target. Figure 4.10 shows the CEMS spectrum. The count rate over noise level during this measurement was typically 500 s^{-1}. The $Au_{70}Cu_{30}$ alloy is particularly well suited for measuring pulse height spectra at and off resonance, because its resonance line is at zero velocity and one can measure at resonance when the source is not moved at all and off resonance when it is moved with a maximum velocity of, for instance, 30 mm/s.

In the case of gold CEMS the typical time for recording a spectrum is 24 h. It is advisable for CEMS measurements to use Pt-sources which have not been re-irradiated too often in order to avoid radiochemical poisoning of the source (c.f. Section 3.2). The source poisoning with ^{198}Au and subsequent ^{198} Hg increases the intensity of high energy gamma rays emitted by the source. These high energy gamma rays produce photo electrons with a correspondingly high energy. These photo electrons have a long range in the sample material and come from deeper layers in the sample than the conversion electrons of the 77.3 keV Mössbauer transition, and therefor contribute to the nonresonant backround countrate, thus decreasing the relative intensity of the resonance effect in the Mössbauer spectrum.

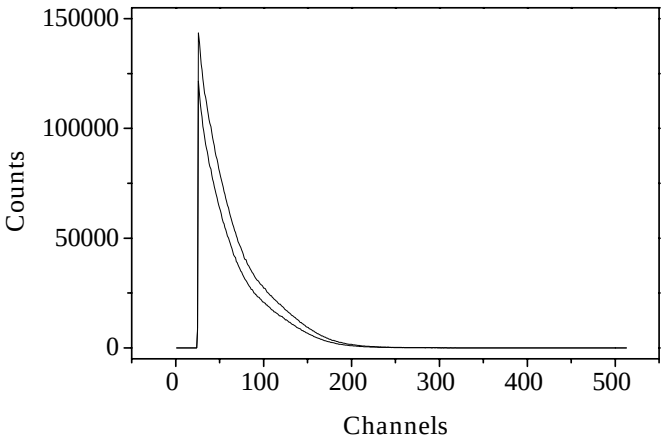

Fig. 4.9: Pulse height spectrum of $Au_{70}Cu_{30}$ at (maximum velocity $v_{max} = 0$) and off resonance ($v_{max} = 30\,mm/s$).

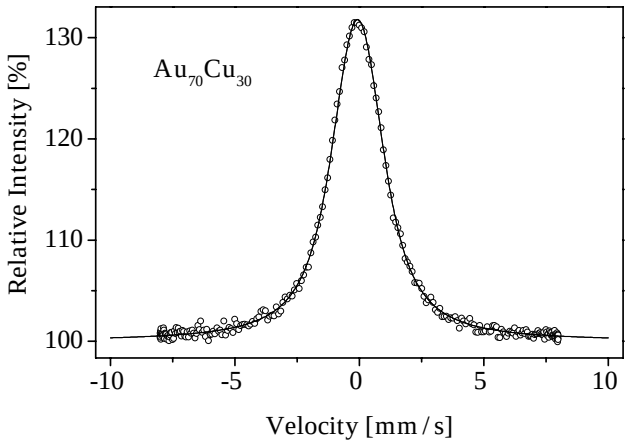

Fig. 4.10: Conversion electron Mössbauer spectrum of $Au_{70}Cu_{30}$ taken with a platinum metal source.

4.5 Monte Carlo Simulation

The Monte Carlo simulation of electron trajectories in the sample can be used to model the range of the electrons in the sample material in order to calculate the probing depth of the CEMS method. The Monte Carlo simulation describes single electron trajectories, where the interaction of the electron and the sample material is based on random selection of the different possible interaction events. When several thousand such electron trajectories have been calculated, one can derive, for instance, a depth profile of electrons which leave the sample with enough energy to be detected.

There are several different ways of simulating electron trajectories numerically, most of them based on a publication of Berger (1963). Various different computer programs have been written, which allow specific problems to be treated, for example SANDYL

by Colbert (1974). For the purpose of this study, a program, allowing the calculations to be made on a personal computer in a reasonable amount of time, was written in the C programming language. The program has been inspired by the most widely used models, but is focusing on the necessities of CEMS. A good review of electron transport in matter has been given by Thümmel (1974). For the generation of random numbers and numerical integration the program uses appropriate routines as described by Press *et al.* (1997).

4.5.1 Model of Electron Transport

The history of a single electron can be described by the following processes:

The conversion electron starts in a given depth with a certain energy, which is the energy of the Mössbauer transition minus the bonding energy of the electron in its shell. The site of electron birth is described by the coordinates x, y and z, where z is the axis perpendicular to the sample surface and therefore describes the depth of the electron in the sample (compare Figure 4.11). The starting direction of the conversion electron (polar angle Θ as angle to the z-axis and azimutal angle Φ) is arbitrary. The depth in the sample should not exceed the range of the electron, since it would than have no chance of leaving the sample.

After the creation of the electron two kinds of interaction with the sample material will influence its path: (1) Elastic scattering on the nuclei, which changes the direction of the electron and (2) inelastic scattering on the electrons bound in the different shells of the atom, which slows down the conversion electron from its starting energy. Elastic scattering on the nuclei, which is basically described by the Rutherford scattering cross section (Rutherford 1911), will determine the mean free path length λ between two such scattering events. Along this path length the electron will slow down without change of direction (Bethe 1930). For the cross sections the relativistic expressions were used.

Coordinate System

The coordinate system is shown in Figure 4.11. The z-axis is defined by the geometry and is perpendicular to the sample surface, which is also the direction of the axis of the CEMS counter chamber. Negative z-values stand for positions in the sample, positive ones for positions above the sample surface. The x and y axes are laying in the sample surface. The polar angle Θ is the angle between the direction s of the electron and the z-axis. The scattering events take place in the primed system, where z' is the primary flight direction of the electron. The direction of the scattered electron in the primed system is s'.

If the scattering angles ϑ and φ are known, the new direction, described by Θ_f and Φ_f in the unprimed system, can be calculated by projecting the primed system on the unprimed system:

$$\cos\Phi_f \sin\Theta_f = \cos\varphi \sin\vartheta \sin\Phi + \sin\varphi \sin\vartheta \cos\Phi \cos\Theta + \cos\vartheta \cos\Phi \sin\Theta \tag{4.1}$$

$$\sin\Phi_f \sin\Theta_f = -\cos\varphi \sin\vartheta \cos\Phi + \sin\varphi \sin\vartheta \sin\Phi \cos\Theta + \cos\vartheta \sin\Phi \sin\Theta \tag{4.2}$$

$$\cos\Theta_f = -\sin\varphi \sin\vartheta \sin\Theta + \cos\vartheta \cos\Theta, \tag{4.3}$$

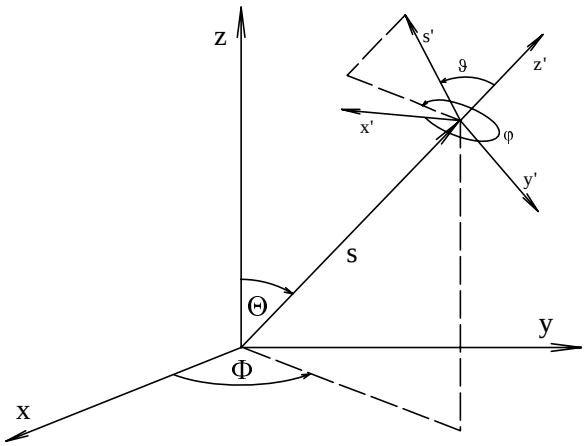

Fig. 4.11: Coordinate system for the calculation of electron trajectories.

where the last equation yields Θ_f and one of the others therewith Φ_f.

Elastic Scattering

The Rutherford cross section for scattering a charged particle (in this case the conversion electron) on a nucleus in the relativistic case is (Rutherford 1911, Thümmel 1974):

$$\frac{\mathrm{d}\sigma}{\mathrm{d}\vartheta} = \frac{r_0^2}{4} \cdot Z^2 \cdot \left(\frac{\varepsilon+1}{\varepsilon(\varepsilon+2)}\right)^2 \cdot \frac{2\pi \sin\vartheta}{\sin^4 \vartheta/2}, \tag{4.4}$$

where Z is the atomic number of the scattering element, $\varepsilon = E/m_0c^2$ the energy of the electron in units of its rest energy and ϑ the scattering polar angle with respect to the direction z' of the incident electron. $r_0 = e^2/(4\pi\varepsilon_0 m_0 c^2)$ is the classical electron radius.

For very small angles ϑ the Rutherford cross section becomes infinitely large and therewith also the total cross section, which is the integral over all possible scattering angles.

Thus various corrections may be added to this formula. The electron spin correction, as suggested by Mott (1929), is important for high energies and light elements, or in the case where $2Z/137\beta \ll 1$ (Thümmel 1974), which is rarely the case for the energy range we are dealing with. $\beta = v/c = \sqrt{\varepsilon(\varepsilon+2)}/(\varepsilon+1)$ is the velocity of the electron in units of the speed of light.

The nuclear size correction describes the entry of the electron into the nucleus for central collisions. It is only important for heavy nuclei and energies in the MeV range, since in this case the size of the nucleus and the DeBroglie wavelength of the electron are of the same order of magnitude: The parts of the DeBroglie wave of the electron which are scattered on different parts of the nucleus may interfere with each other and thus reduce the scattering cross section.

The screening correction takes into account the screening of the nucleus by the atomic electrons. Wenzel (1927) assumed an exponential decrease of the electronic charge density with the distance from the nucleus. He introduced a screening angle ϑ_1

with which Equation 4.4 becomes

$$\frac{\mathrm{d}\sigma}{\mathrm{d}\vartheta} = \frac{r_0^2}{4} \cdot Z^2 \cdot \left(\frac{\varepsilon+1}{\varepsilon(\varepsilon+2)}\right)^2 \cdot \frac{2\pi \sin\vartheta}{(\sin^2\vartheta/2 + \frac{1}{4}\vartheta_1^2)^2}. \tag{4.5}$$

The screening angle ϑ_1 is the ratio of the de Broglie wavelength of the incident electron and the effective atomic radius. For relativistic electrons one obtains (Thümmel 1974)

$$\vartheta_1 = \frac{Z^{1/3}}{137} \frac{1}{\sqrt{\varepsilon(\varepsilon+2)}}. \tag{4.6}$$

With the introduction of the screening angle the cross section becomes finite also for $\vartheta = 0$. Thus the total cross section

$$\Sigma = \int_0^\pi \frac{\mathrm{d}\sigma}{\mathrm{d}\vartheta}\mathrm{d}\vartheta \tag{4.7}$$

becomes finite. In a material with N atoms per unit volume this yields a mean free path length

$$\lambda = 1/(N \cdot \Sigma) \tag{4.8}$$

between two elastic scattering events.

In practice an average scattering angle $\overline{\vartheta}$ is calculated from the angular distribution of cross sections and the total cross section according to

$$\overline{\vartheta} = \frac{\int_0^\pi \vartheta \cdot \frac{\mathrm{d}\sigma}{\mathrm{d}\vartheta}\mathrm{d}\vartheta}{\Sigma}. \tag{4.9}$$

After scattering the new position of the electron is recalculated as a function of the polar scattering angle $\overline{\vartheta}$, the arbitrarily chosen azimutal scattering angle $0 \leq \varphi < 2\pi$ and a travelled path Δs, which is derived from the mean free path by $\Delta s = -\lambda \cdot \ln\xi$ (Berger 1963), where ξ is a random number between 0 and 1.

Inelastic Scattering – Slowing Down

The second kind of event is the interaction of the conversion electrons with the atomic electrons (ionisation and excitation). Assuming that the energy transfer on a single such event is small, the change in direction during this processes may be neglected and one can use the Bethe-Bloch formula (Bethe 1930, Evans 1955):

$$-\frac{\mathrm{d}E}{\mathrm{d}s} = 2\pi\rho\frac{r_0^2}{u}\frac{m_0c^2}{\beta^2} \cdot \frac{Z}{A} \cdot \left[\ln\left(\frac{\varepsilon(\varepsilon+2)}{(I/m_0c^2)^2} \cdot \frac{\varepsilon}{2}\right) + \frac{1+\frac{\varepsilon^2}{8} - (2\varepsilon+1)\ln 2}{(\varepsilon+1)^2}\right], \tag{4.10}$$

where ρ is the density of the sample material, $\beta = v/c = \sqrt{\varepsilon(\varepsilon+2)}/(\varepsilon+1)$ is the velocity of the electron in units of the speed of light and I is the average excitation energy of the atomic electrons. For I Sternheimer (1966) gave the relation

$$I = (9.76Z + 58.8Z^{0.19}) \cdot 10^{-3} \qquad [\mathrm{keV}]. \tag{4.11}$$

The travelled path Δs between two elastic scattering events is small enough that the change in energy can be written as

$$\Delta E = -\frac{\mathrm{d}E}{\mathrm{d}s} \cdot \Delta s. \tag{4.12}$$

Compound materials

The above descriptions are satisfying for homogenous samples consisting of a single element. In the more common cases of compounds and alloys some additional considerations are necessary: The total cross sections Σ_n and the mean free path length $\lambda_n = 1/(N_n \cdot \Sigma_n)$ for the n_0 different elements must be calculated individually. N_n is the number of atoms of the n-th element per unit volume. The mean free path λ is then calculated from

$$\frac{1}{\lambda} = \sum_{n=1}^{n_0} \frac{1}{\lambda_n} \tag{4.13}$$

and the travelled path $\Delta s = -\lambda \cdot \ln \xi$.

After the travelled path Δs the element n on which the electron scatters elastically is chosen by another random number ξ, according the atomic densities N_n of the n_0 elements. For the scattering angle $\overline{\vartheta} = \overline{\vartheta}_n$ is used.

The energy loss on the travelled path Δs is now

$$\Delta E = \Delta s \cdot \rho_c \sum_{n=1}^{n_0} \frac{-(\mathrm{d}E/\mathrm{d}s)_n}{\rho_n}, \tag{4.14}$$

where ρ_c is the density of the compound material.

Summarizing the path of a conversion electron can be described as follows: The site of birth of the electron is arbitrarily chosen, not to far from the surface, so there is a probability for the electron to get to the surface of the sample. The initial energy E_0 of the electron is given by the conversion process. The angle against the surface of the sample, with which the electron is emitted from the Mössbauer isotope are arbitrarely chosen as well. By travelling in the given direction a pathlength, which is calculated from the total cross section for elastic scattering (Equation 4.8), the conversion electron is slowed down according inelastic scattering, described by the Bethe-Bloch relation (Equation 4.10). After travelling this path, the conversion electron is elastically scattered on an atom of the sample, changing its direction (Equation 4.9). The path of the conversion electron is followed until it reaches the surface of the sample or until it lost its total energy. The path of the electron can be recorded. Of special interest are the depth of origin z of the conversion electron and its escape energy E, when leaving the sample at the surface.

4.5.2 Results

Figure 4.12 shows the paths of six conversion electrons in a metallic gold sample. The typical number of steps (elastic scattering) for this simulation was more then 3000 for the electrons loosing their total energy. Two of the conversion electrons in Figure 4.12 are leaving the sample at the surface. It can be clearly seen, how the paths of the electrons become scrambled at the end, due to the increasing probability for reflecting angles in elastic scattering events at small energies.

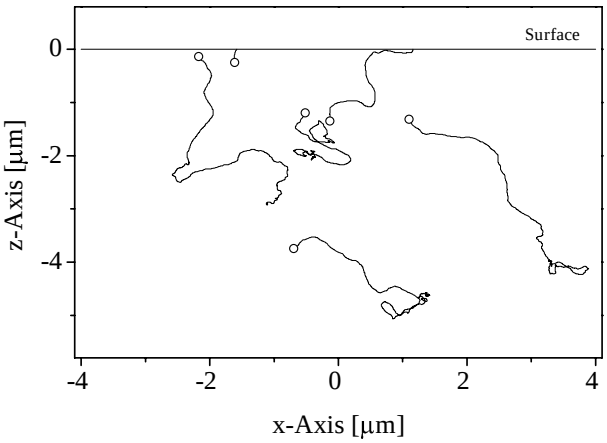

Fig. 4.12: Paths of six conversion electrons in a metallic gold sample. The site of birth of the electrons are marked with open circles. The third dimension (y-axis) is skipped in this figure.

To obtain statistical results from such Monte Carlo simulations of the trajectories of the conversion electrons it is necessary to record several ten thousand electrons. Thereby only those electrons are of interest, which are leaving the sample at the surface to be detected and therefore contribute to the signal in the Mössbauer spectrum. For the results, which are described in the following, the trajectories of 30000 conversion electrons were calculated for each of the three Mössbauer isotopes ^{197}Au, ^{119}Sn and ^{57}Fe. For gold and tin only L-conversion, for iron only K-conversion was considered. The samples were metallic gold, metallic tin and metallic iron. The number of electrons, which leave the sample at the surface were in this simulations 7241, 5707 and 4962, respectively. The time for the calculation for one isotope was typically one hour.

Figure 4.13 shows the depth of origin z of the conversion electrons as a function of the escape energy E in units of their initial energy E_0.

The simulation in Figure 4.13 shows for gold a deeper slope of the tangent to the data points compared to the slope for tin or iron. This reflects the higher capability of heavy nuclei for total reflection of electrons in a central collision: Conversion electrons, which start close to the surface in direction into the sample have in gold a higher probability for being totally reflected and subsequently getting to the surface, than in iron. This is also supported by the total numbers of electrons which leave the sample, as given above.

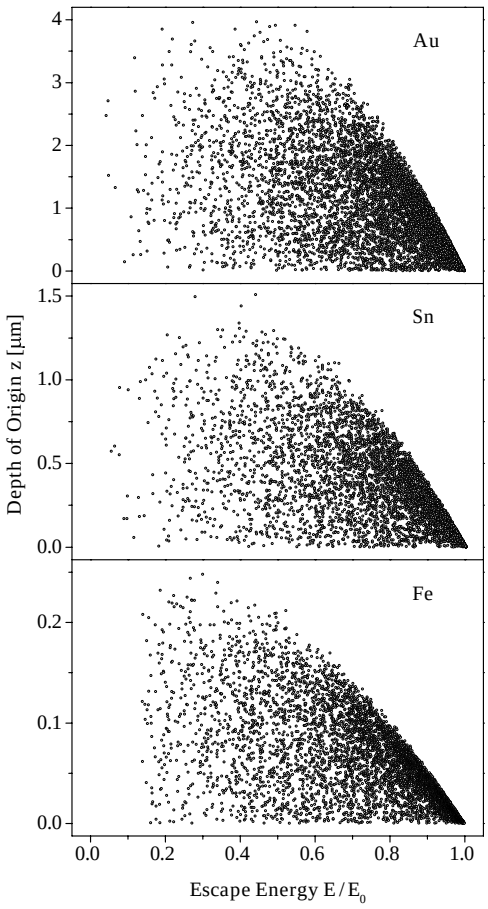

Fig. 4.13: Depth of origin z as a function of the relative escape energy E/E_0 of the electrons, when leaving the surface of the sample.

From the obtained data one can derive, for example, the distributions for the depth z of the origin of the electrons and for the energy E of the electrons, when leaving the surface of the sample. This distributions are shown in Figure 4.14.

The distribution for the depth z of the origin of the electrons leaving the sample can be used to calculate the probing depth of CEMS. Table 4.1 gives the thickness of the surface layer from which 50% and 90% of the total number of the electrons emerge. The values for the 90% emergence realistically approximate the probing depth of CEMS. For this calculations only the L-conversion for gold and tin and the K-conversion for iron were taken into account. The more rarely conversion from higher shells yields conversion electrons of higher starting energy and therewith higher contribution of deeper layers. Considering also Auger electrons, which have a smaller energy than the conversion electrons, would contribute to a higher escape rate from depths close to the surface.

Figure 4.13 already suggests a possible correlation between the depth z from which the conversion electron emerges and the escape energy E. Such correlations can be used for DCEMS, a depth sensitive kind of CEMS using a detector system with high energy resolution. The high energy resolution could be obtained by the separation of electrons of different energies by the application of electrical or electromagnetical filters. The

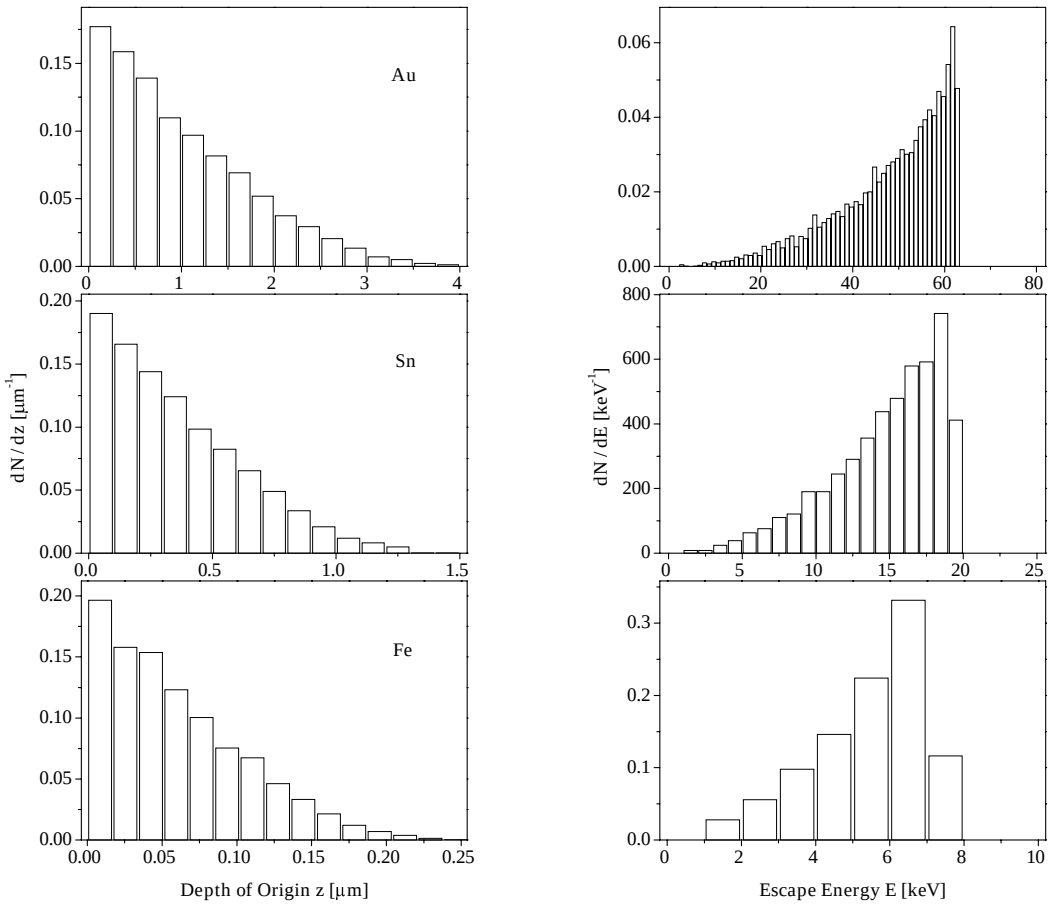

Fig. 4.14: Distributions of the depth of origin z (left) and the escape energy E (right) of conversion electrons leaving the sample: Metallic gold (top)(L-conversion only), metallic tin (middle)(L-conversion only) and metallic iron (bottom)(K-conversion only), according the Monte Carlo calculations shown in Figure 4.13.

Tab. 4.1: Thickness of the surface layer from which 50% and 90% of the conversion electrons emerge in Au, Sn and Fe CEMS, according to the Monte Carlo simulations shown in Figure 4.14.

Sample	50%	90%
metallic Au	0.8 μm	2.2 μm
metallic Sn	0.3 μm	0.8 μm
metallic Fe	0.05 μm	0.12 μm

single channel discriminator window is set to a certain electron energy in the electron pulse height spectrum and so one should obtain information from a certain depth in the sample. For the case of ^{57}Fe in metallic iron Figure 4.15 shows the distribution of the depth z of the origin of the K-conversion electrons for different energy windows.

As can be seen there is no unequivocal correlation between the energy and the origin depth of a electron leaving the sample: The distributions of neighbouring energy windows are widely overlapping, especially for energies below 7.0 keV. However, as can

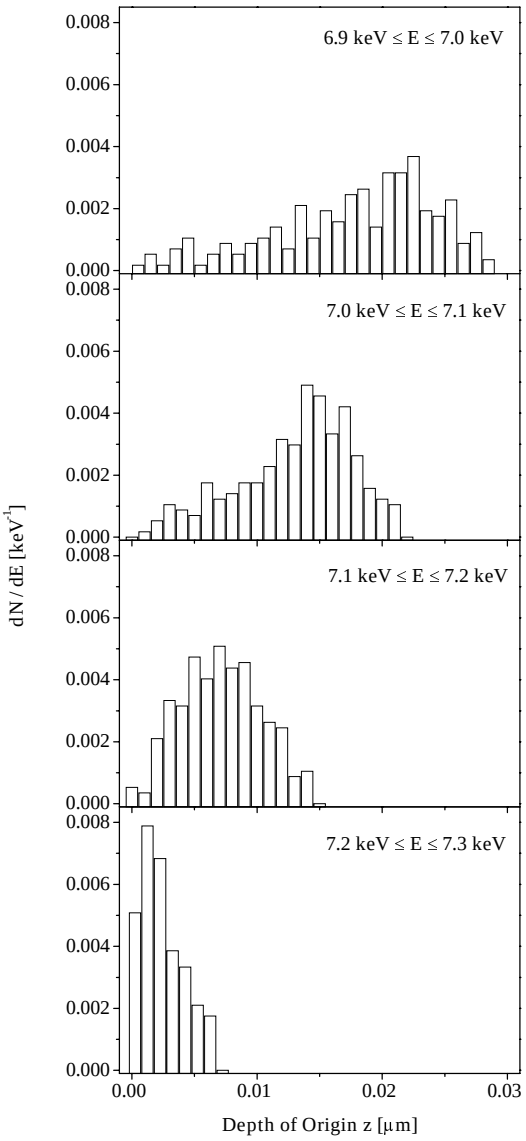

Fig. 4.15: Distributions of the depths z of origin of electrons leaving the surface of the sample within the indicated energy windows, according the simulation shown in Figure 4.?.

be seen from Figure 4.13, the maximum depth from which electrons with a certain energy may come from is well defined. So one might record Mössbauer spectra with energy windows set to $E_{\min} \leq E \leq E_0$, where $E_{\min}$ determines the maximum probing depth. The samples should be then thin enough, thus no conversion electrons from higher shells, which lost already energy in the sample, would contribute to the countrate in the set energy window.

At the end of this chapter an experiment should be described, which demonstrates the reliability of the Monte Carlo simulation method. For gold it is possible to experimentally examine the depth sensitivity: For this gold leaves were put on a $AuAl_2$ substrate and for each layer a CEMS spectrum was taken. The signal from the substrate can be well distinguished from the metallic gold layer by the large isomer shift of 6.03 mm/s for $AuAl_2$. The handmade leaves had a thickness between 0.125 μm and

0.166 μm only. The 18 spectra are shown in Figure 4.16.

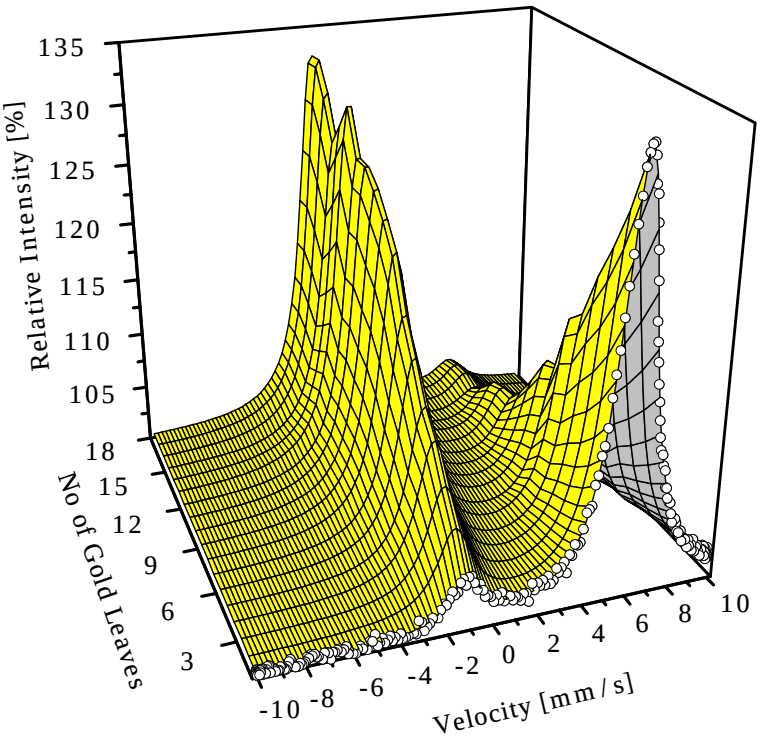

Fig. 4.16: CEMS spectra of 18 gold layers on a $AuAl_2$ substrate. The single line at 6.03 mm/s, whose intensity decreases with the thickness of the gold layer, arises from the $AuAl_2$ substrate; the intensity of the single line at -1.23 mm/s increases with the thickness of the gold metal layer. The figure shows raw data. Irregularities in the increasing and decreasing peak are due to changes in the total area, which arise from instabilities in the counter operation. For the calculations only the relative areas of the two peaks were used.

Figure 4.17 shows the relative intensity of the metallic gold line as a function of the thickness of the gold layer. It also shows the result of a Monte Carlo simulation. For this Monte Carlo simulation the following additional assumptions were made: For the emission of the conversion electron the f-factor of gold in $AuAl_2$, which is 1.13 times the f-factor of metallic gold, is taken into account as well as the lower density of gold due to the low density of $AuAl_2$, $\rho_{AuAl_2} = 7.729\,g/cm^3$. Electrons moving from the gold layer towards the $AuAl_2$ substrate are terminated, because they have only very little chance to be totally reflected and leave the sample. Electrons originating from the $AuAl_2$ substrate have to pass the gold layer, before getting out. The electrons which are leaving the sample surface are assumed to be detected irrespective of their escape energy.

Figure 4.17 shows that the results of the experiment and the Monte Carlo simulation are in good agreement, but there is a small overestimation of the contribution of metallic Au by the Monte Carlo simulation around an overlayer thickness of 0.8 μm. Such differences may arise from the varying thicknesses of the individual gold leaves. The total amount of metallic gold from the 18 layers was verified by a transmission experiment to be 2.64(4) μm yielding an average thickness of the single Au leaf of 0.147 μm.

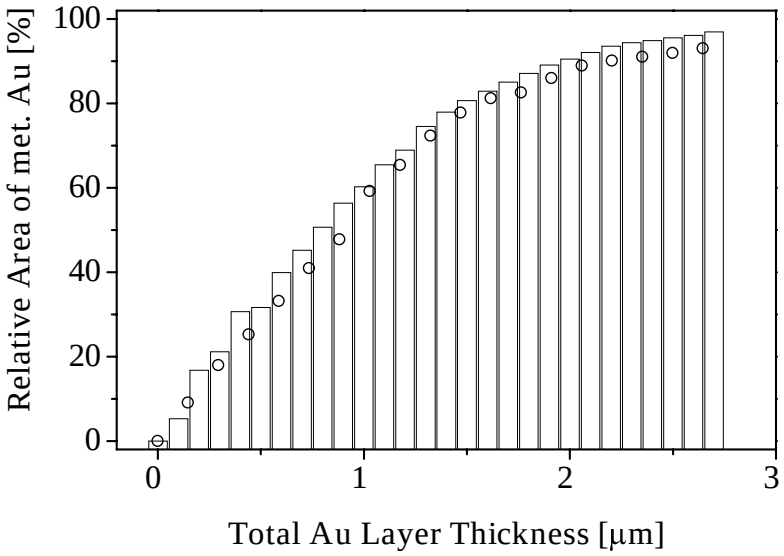

Fig. 4.17: Relative intensity of the gold metal peak as a function of the thickness of the gold layer. Circles show measured data as in Figure 4.16, bars show the results of the Monte Carlo simulation.

4.6 Summary and Conclusions

Conversion electron Mössbauer spectroscopy is a most sensitive technique for studying surface layers by Mössbauer spectroscopy, since the probing depth is defined by the rather short range of the conversion electrons in the sample material. The probing depths for tin and iron are typically in the range of some tenths of a micrometer and up to several micrometers for gold (Table 4.1).

The set-ups for CEMS with different Mössbauer isotopes require special considerations. The size of the counter chamber and the He gas density should be chosen so that the conversion electrons are completely stopped in the chamber. In this way the maximum pulse height is achieved and so one most successfully discriminates pulses from noise. The samples have to be mounted within the counter chamber. For non-destructive studies, this requires a small sample size of $1 - 2\,\mathrm{cm}$ in diameter. At room temperature it might also be possible in some cases to attach the open chamber to the object and seal it with silicon gel.

In archaeometallurgy, where one is primarily interested in the properties of the original (bulk) material, it should be considered that any kind of surface contamination and especially oxidation may influence the results of the measurement. In the case of gold coins (Chapter 6) the surface sensitivity yields interesting information, while for other cases like steel (Chapter 7) and bronze objects the study of the corrosion products on the surface is usually of no particular interest.

5 Mössbauer Spectroscopy in the Backscattering Mode

5.1 Introduction

As in the case of CEMS, Mössbauer spectroscopy in the backscattering mode is a non-destructive method suitable for samples which are too thick for transmission measurements.

For the detection of the Mössbauer absorption one uses the γ-rays emitted when the excited nuclei decay back to the ground state or the emitted X-rays emitted after resonant γ-ray absorption and subsequent internal conversion.

The probing depth depends on the attenuation of the incident γ-rays in the absorber by resonant as well as photoelectric absorption and on the attenuation of the γ-rays or X-rays that leave the sample.

First measurements in backscattering mode were performed by Major (1962) using the back scattered 14.4 keV γ-rays of ^{57}Fe for the detection of the Mössbauer absorption. Hershkowitz and Walker (1967) counted the X-rays after internal conversion in a forward scattering geometry. One of the first backscattering experiments with X-rays was reported by Swanson and Spijkerman (1970). ^{197}Au Mössbauer spectroscopy in backscattering mode is published the first time in the present work.

5.2 Experimental Set-Up for ^{57}Fe

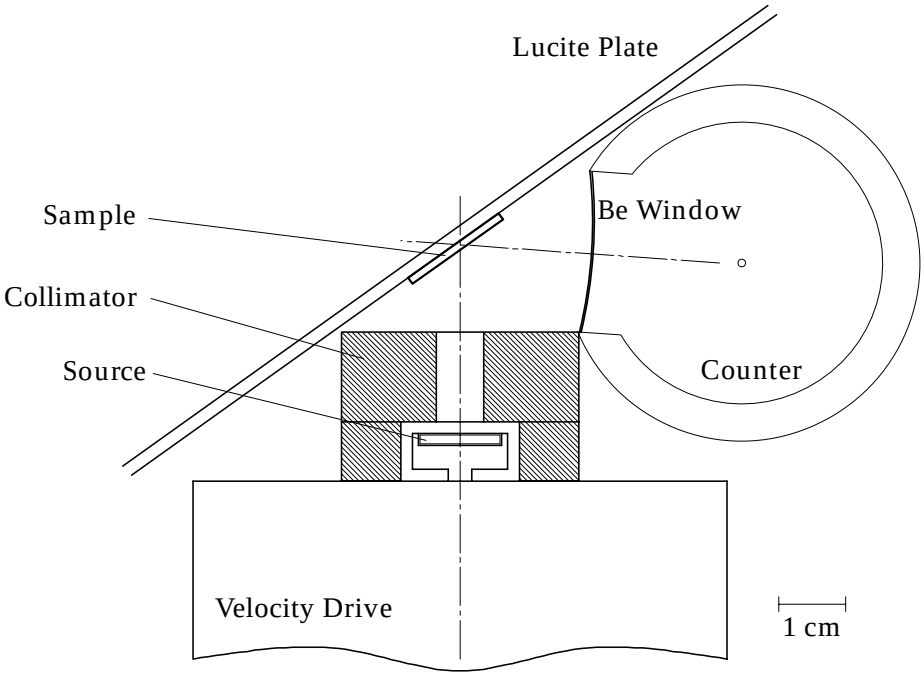

Fig. 5.1: Schematic view of the geometry used for iron backscattering.

The set-up used in this work for room temperature measurements is very simple (Figure 5.1). The source is mounted on the velocity drive and its radiation is strongly collimated to a diameter of 8 mm as in CEMS. The sample is mounted on a lucite plate on the axes of the velocity drive in front of the collimator in such a way that the sample is at an angle of about 45^o to the radiation. Using a low Z material like lucite as the sample carrier helps to avoid non-resonant scattering of γ-rays. Radiation scattered by an angle of about 90^o reaches the krypton filled proportional counter, which is shielded from the direct radiation from the source by the lead collimator.

For finding the optimum adjustment of the single channel analyser one can use the same method used for CEMS: One measures the pulse height spectrum of a stainless steel foil enriched in ^{57}Fe in and out of resonance (c.f. Figure 4.3), i.e. with a velocity of 0 and 20 mm/s, respectively (Figure 5.2).

The difference of these two spectra shows the regions in the γ-ray spectra containing counts, which can be used for detecting resonant absorption. In case of the iron it is most efficient to set the single channel analyser window to the 6.4 keV X-ray peak of iron. One should then avoid any other source of 6.4 keV radiation. It is impossible to avoid the X-rays stemming from the photo absorption of 14.4 keV γ-rays in the sample. What one can avoid, however, are 6.4 keV iron X-rays emitted by the source after

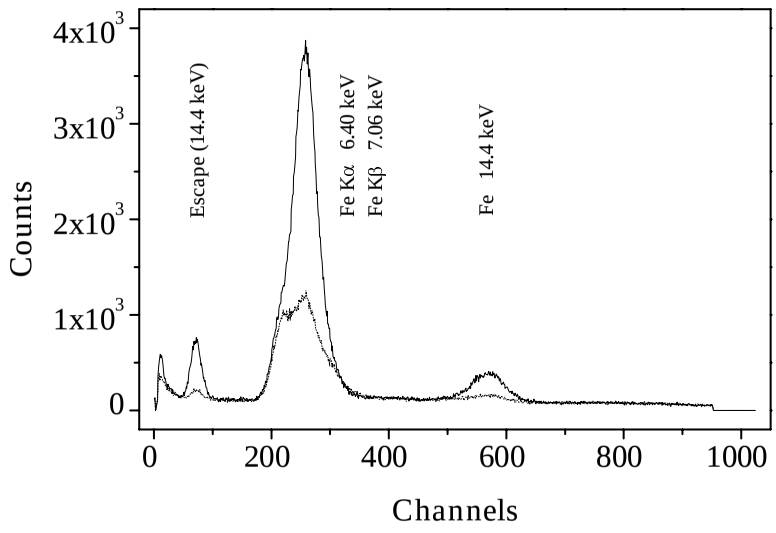

Fig. 5.2: Pulse height spectrum of X-rays back scattered from a stainless steel sample in and out of resonance. The time of measurement is 120 s lifetime.

internal conversion process and Rayleigh scattered in the sample. This can be done by placing a vanadium foil of about 7 μm thickness between source and sample. With a total absorption coefficient of 370 cm^2/g (interpolated data from Storm 1970) at 6.4 keV it absorbs nearly 80% of the 6.4 keV X-rays coming from the source, while 81% of the 14.4 keV γ-rays get through.

5.3 Experimental Set-Up for ^{119}Sn

The set-up for iron can also be used for tin. Like in the CEMS experiments SnO_2 (c.f. Figure 4.6) was used to find the regions in the pulse height spectrum which contain the information on resonant absorption (Figure 5.3). In the case of tin, the back scattered 23.9 keV γ-rays are preferable for detecting Mössbauer absorption. For a quick adjustment of the single channel analyser it is helpful to use direct radiation from the source. The 23.9 keV Mössbauer γ-rays also give rise to a escape peak of the Kr countergas at 11.3 keV. A single channel window was set on both peaks, 23.9 keV and 11.3 keV, and the output pulses of both single channel analysers were used for measuring the Mössbauer spectra. Despite the high conversion rate of $\alpha = 5.1$ the Sn L X-rays do not contribute much to the pulse height spectrum, because of the strong absorption of this low energy radiation in the sample itself.

Here too, a filter between source and sample is useful: The 25.2 keV K_α X-rays from the ^{119}Sn source are very close to the resonant γ-radiation and may reach the detector after being Compton or Rayleigh scattered in the sample. In the case of Compton scattering the energy of the X-ray shifts, but depending on the angle and the energy resolution of the detector it may still fall into the single channel window. For a scattering angle of 90^o the energy of the Compton scattered K X-ray will be 24.0 keV (c.f. Equation

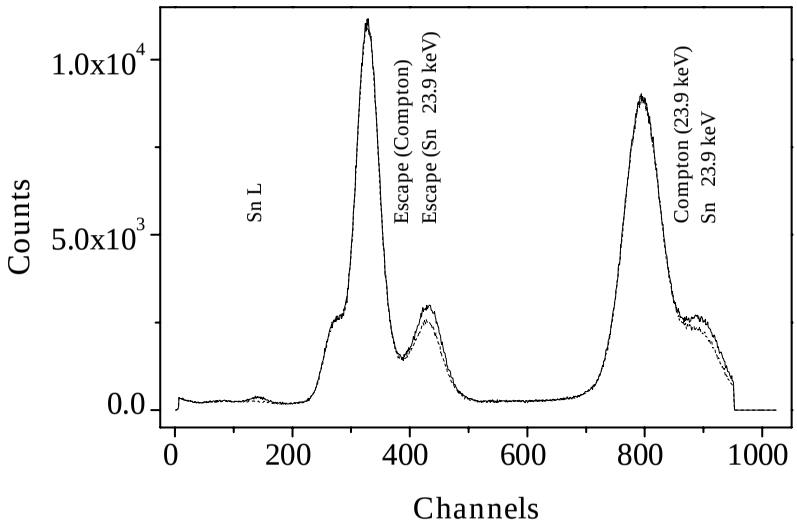

Fig. 5.3: Pulse height spectrum of γ-rays back scattered from a tindioxide sample in and out of resonance. The time of measurement is 1000 s lifetime.

5.11). To avoid this one can use a 35 μm palladium foil, which has its K absorption edge at 24.35 keV, i.e. a position between the resonant γ-ray and the disturbing K_α X-ray.

5.4 Experimental Set-Up for ^{197}Au

As has already been mentioned, in scattering experiments with ^{197}Au both the source and the sample have to be kept at liquid helium temperature. The cryostat that was available for the experiments described here was the one shown in Figure 3.2. The drive tip (Figure 5.4) holding the source and the absorber therefore had to be redesigned for a backscattering geometry. The new drive tip was made out of lucite to avoid Rayleigh and Compton scattering of the γ-rays on heavy elements, which would contribute to the backround under the resonant scattering events.

The γ-rays emitted by the source in an upward direction under an angle Θ to the vertical are scattered vertically downwards and reach the detector through the window in the bottom of the cryostat. The source in its lucite holder is mounted in a massive tantalum cylinder, which shields (with an total absorption coefficient of 8.5 cm^2/g at 77.3 keV (Storm 1970)) the detector from direct γ radiation from the source. The source is at rest, while the sample is vibrated by the velocity drive. Figure 5.5 shows the optical path in this backscattering geometry.

Figure 5.6 shows the pulse height scattering spectrum of a metallic Au foil of 56 μm thickness, taken with source and absorber at 4.2 K. The detector was a 8 mm thick planar germanium detector mounted outside the cryostat as in the transmission. The main peak in Figure 5.6 is from Compton backscattering of the 77.3 keV γ-rays, but above the Compton scattering peak the Au $K_{\alpha 1,2}$ X-ray lines and the resonantly

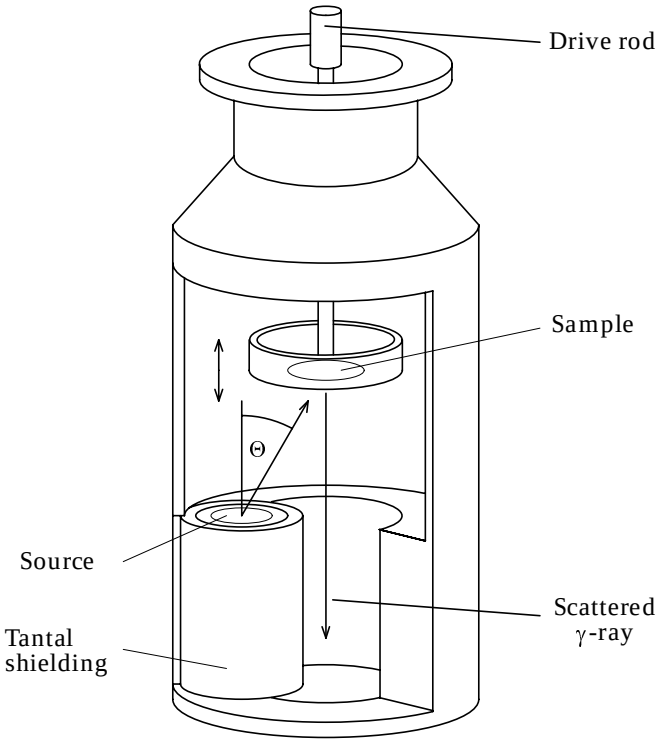

Fig. 5.4: Drive tip for γ-ray backscattering experiments in the liquid helium bath cryostat.

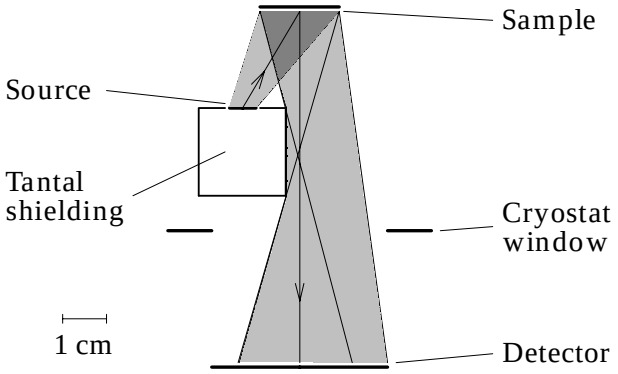

Fig. 5.5: Optical path in the backscattering geometry in the liquid helium bath cryostat.

scattered 77.3 keV γ-rays can also be seen. The last three peaks were used for the energy calibration of the detector. The energy resolution is about 1 keV.

The geometry used for the scattering experiment bears the disadvantage that the effective velocity of the Doppler motion of the scatterer in the direction of the incident γ-rays is

$$v_D = v_G \cdot \cos\Theta, \tag{5.1}$$

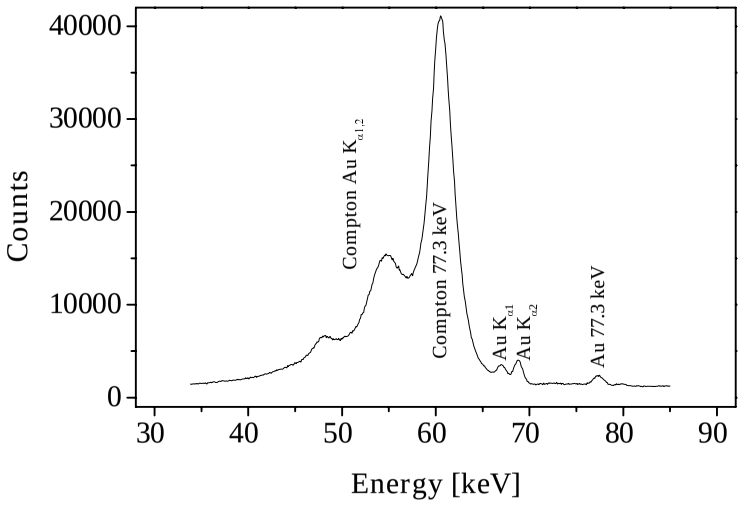

Fig. 5.6: Pulse height spectrum of the back scattered radiation of a Au foil. Time of measurement is 3000 s lifetime, with a moved source.

where v_G is the actual drive velocity. A lorentzian line can therefor be written as

$$S(v_D) = \frac{1}{1+\left(\frac{v_D - IS}{LW/2}\right)^2} = \frac{1}{1+\left(\frac{v_G \cdot \cos\Theta - IS}{LW/2}\right)^2} = \frac{1}{1+\left(\frac{v_G - IS/\cos\Theta}{\frac{LW/\cos\Theta}{2}}\right)^2}. \tag{5.2}$$

Thus one expects a shift of a line at a position IS to a position

$$P = \frac{IS}{\cos\Theta} \tag{5.3}$$

and a broadening from the linewidth LW observed in a standard absorption experiment to a width

$$W = \frac{LW}{\cos\Theta}. \tag{5.4}$$

Moreover, the finite size of source and scatterer defines a distribution of possible Θ values, which leads to additional broadening. A mathematical solution of this problem turns out to be difficult, requiring a six fold integral over the areas of the source and the sample, the thickness of the sample and the energy. For use in a least squares fitting procedure this would have to be calculated for a whole range of different velocities. It also needs as an input parameter the distance between source and sample which may vary slightly from experiment to experiment and is difficult to measure exactly because the position conditions of the drive rod after mounting the sample may change slightly.

A practical solution is the simultaneous measurement of a reference sample, in this case an $AuAl_2$ ring with an isomer shift of $IS = 6.03$ mm/s (Figure 5.7).

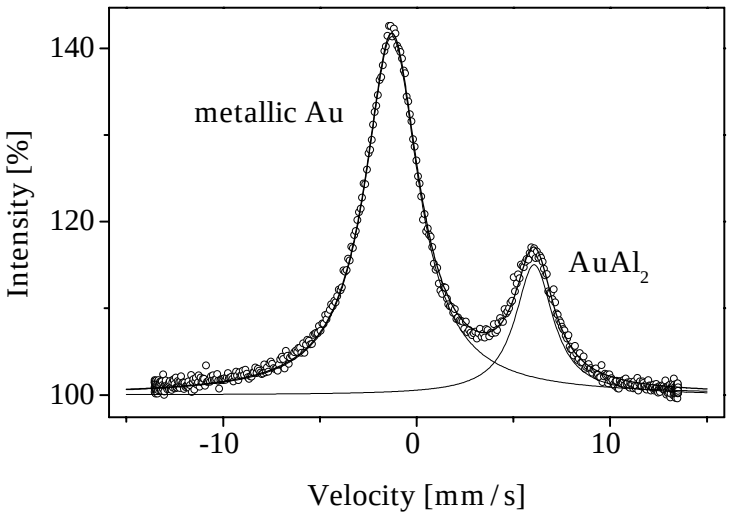

Fig. 5.7: Back-scattered Mössbauer spectrum of a metallic gold sample and the $AuAl_2$ reference sample, corrected to the Doppler maximum velocity. The time of measurement was one day.

In a first approximation only the maximum velocity has to be recalculated in order to readjust the line of $AuAl_2$ to its real isomer shift. In this way the position of the lines of alloys of known composition is successfully corrected to its real value, as shown in Figure 5.7 for a sample of metallic gold. Although the geometry is not ideal because of the distribution of possible values of Θ this method can be used to determine isomer shifts of samples of unknown composition. The $AuAl_2$ line can be fitted with the sample and later subtracted from the spectrum.

5.5 Probing Depth

As has already been mentioned, the probing depth in the case of backscattering of γ-rays is due to the absorption of the resonant γ-ray. The total photoelectric cross section σ_p has to be taken into account as well as the total resonant cross section σ_0 (Equation 2.12). Both can also be described as absorption coefficients for a given sample material.

Tab. 5.1: Total photoelectric absorption coefficient μ_p and total resonant absorption coefficient $\mu_0 = \sigma_0 \cdot f \cdot n$ for different systems and their appropriate energies. f is the Lamb Mössbauer factor (c.f. Figure 2.3) of the sample material and n the density of Mössbauer nuclei. μ_p is calculated from values given in Storm (1970).

System	f-factor	μ_p $[\mathrm{cm}^{-1}]$	μ_0 $[\mathrm{cm}^{-1}]$
metallic Au (77.3 keV)	0.18 at 4.2 K	32.1	411
metallic Sn (23.9 keV)	0.16 at RT	111	708
metallic Fe (14.4 keV)	0.81 at RT	493	3392

As can be seen from Table 5.1 the total resonant absorption coefficient is significantly higher than the total photoelectric absorption coefficient, hence resonant absorption is the dominant process in these systems. For real samples, the situation may change if there are heavy elements present, particularly in the case of ^{57}Fe and ^{119m}Sn. This may increase the total photoelectric absorption dramatically, while the total resonant absorption will decrease due to lower density of the Mössbauer nuclei compared to the pure system. Furthermore, especially in the case of iron, magnetic splitting may also decrease the total resonant absorption coefficient for the single lines and thus increase penetration depth.

According to Equation 2.10 the energy spectrum emitted by the source moving at a velocity v can be written as

$$S(E,v) = \frac{S_0}{1+\left(\frac{E-v}{LW/2}\right)^2}, \tag{5.5}$$

where all the constants are represented by S_0, while the linewidth LW and the energy E (both in mm/s) are defined as $LW := \Gamma \cdot c/E_0$ and $E := \Delta E \cdot c/E_0$. In a similar way the resonant absorption cross section in the sample (c.f. Equation 2.11) can be given as

$$\sigma_r(E) = \frac{\sigma_0}{1+\left(\frac{E-IS}{LW/2}\right)^2}. \tag{5.6}$$

The absorption coefficient is thus a sum of the coefficient for resonant absorption, $\mu_a(E) = \sigma_r(E) \cdot f \cdot n$, and for photoelectric absorption, μ_p. At a depth z in the sample, the incident intensity is

$$S(E,v,z) = S(E,v) \cdot \exp\left(-(\mu_a(E)+\mu_p)\cdot z\right). \tag{5.7}$$

According to Equation 2.13, the amount of radiation absorbed in a thin layer dz at a depth z in the absorber is

$$S_a(E,v,z)\mathrm{d}z = S(E,v,z)\cdot\mu_a(E)\cdot\mathrm{d}z. \tag{5.8}$$

The re-emission may occur in any direction, and the fraction scattered into the solid angle covered by the detector is determined by the experimental set-up. Another factor is the decay channel (γ-ray scattering or X-ray re-emission after a preceeding conversion process) observed in the experiment. Both factors are constant for the measurement and need not be considered for the calculation of the probing depth. The radiation re-emitted in a depth z will be attenuated by absorption on the way out of the sample before reaching the detector. Resonantly re-emitted γ-quanta may be absorbed both resonantly and photoelectrically, while the non-resonant γ-quanta can only be absorbed photoelectrically. The intensity eventually reaching the detector after having been resonantly scattered in a depth z is therefore proportional to

$$S_D(E,v,z) = S_a(E,v,z)\cdot\left[f\cdot\exp\left(-(\mu_a(E)+\mu_p)z\right) + (1-f)\cdot\exp\left(-\mu_p z\right)\right] \tag{5.9}$$

In the case of iron, where the K X-rays emitted after internal conversion are best detected because of the large conversion coefficient, the factor in brackets has to be changed to $[\exp(-\mu_{px} \cdot z)]$, where μ_{px} is the total photoelectric absorption coefficient for the 6.4 keV X-rays in the sample material.

To obtain the count rate of the detector as a function of the velocity v one now has to integrate over the whole energy range and the thickness z_A of the sample:

$$S(v) = \int_0^{z_A} \int_{-\infty}^{+\infty} S_D(E, v, z) \mathrm{d}E \mathrm{d}z. \tag{5.10}$$

For gold it is possible to do backscattering experiments on metallic gold foils of different thicknesses, as well as simulate the spectra of such gold foils. Figure 5.8 shows simulated spectra according to Equation 5.10 for backscattering on foils of various thicknesses. The solid lines are lorentzians fitted to the simulated spectra. These fit well and are used for comparing the areas of the different spectra. The saturation can be clearly seen with increasing foil thickness.

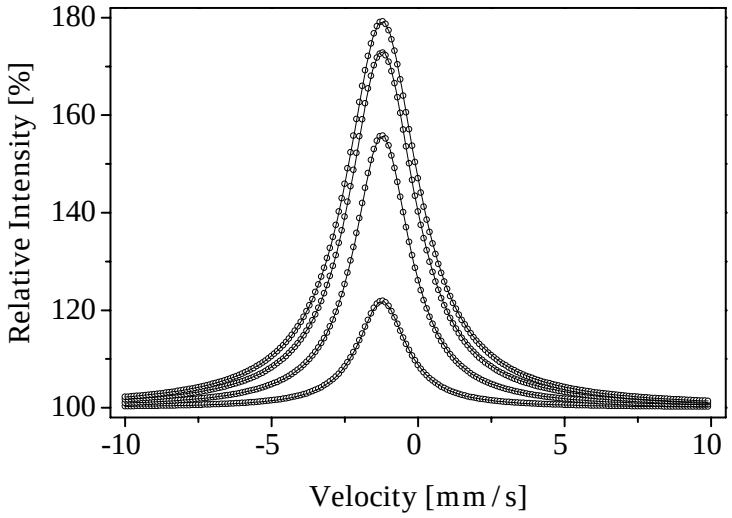

Fig. 5.8: Simulated back-scattered Mössbauer spectra for metallic gold foils of z_A =10, 40, 100 and 200 μm thickness. The solid lines are fitted lorentzians. One sees that with increasing sample thickness both the intensity and the linewidth increases.

For the following discussion the area of the spectra was normalised to the area of the spectrum for an infinitely thick sample. In the case of gold saturation has practically been reached for a thickness of 500 μm. In this way, measured spectra can be compared to the simulated spectra. For the measured spectra the signal from a $AuAl_2$ ring as a reference sample was used to make the different measurements comparable. Figure 5.9 shows the normalised areas from measured foils and the simulated data according to Equation 5.10 as a function of sample thickness z_A. The experimental linewidths and the simulated linewidths are compared in Figure 5.10.

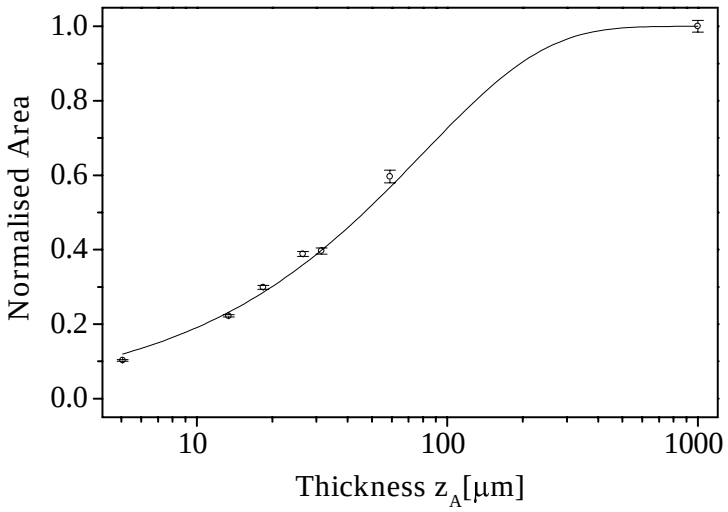

Fig. 5.9: Normalised areas of the backscattering Mössbauer spectra from gold foils of different thicknesses. The solid line is simulated according to Equation 5.10 and Figure 5.8.

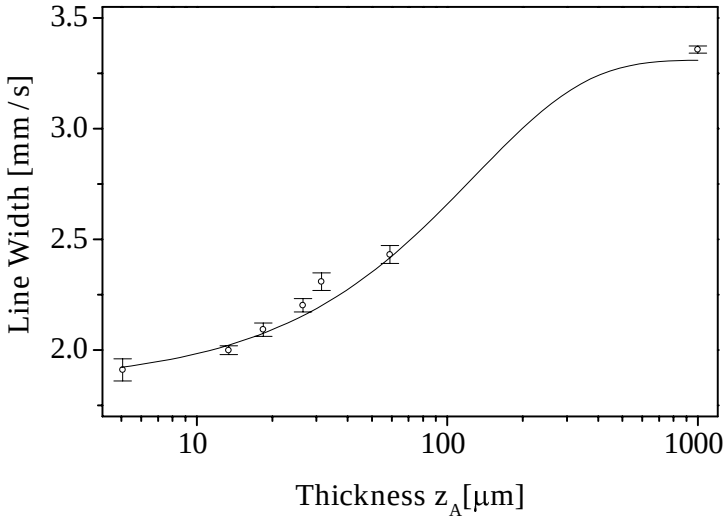

Fig. 5.10: Experimental and simulated lorentzian line widths for gold foils of different thicknesses. The solid line is simulated according to Equation 5.10 and Figure 5.8.

For both the area and the linewidth the simulated values fit the data very well. For the line width, one also may expect an additional geometrical broadening due to the finite size of the sample and the source and therewith a distribution of values for the angle Θ. However, as can be seen from Figure 5.10, the additional broadening from saturation seems to be much stronger than the additional geometrical broadening, which would appear as a constant distance of the data points beyond the theoretical curve.

Equivalent to the probing depth given in the CEMS method (c.f. Section 4.3.2) the probing depth for the backscattering mode can be defined as the depth from which 90% of the resonantly scattered γ-rays emerge. From Figure 5.9 one can directly take the sampling depth of backscattering Mössbauer spectroscopy in the case of metallic

gold. The results are compiled in Table 5.2 together with the results for metallic tin and metallic iron, which were also calculated according Equation 5.10.

Tab. 5.2: Thickness of the surface layer from which 50% and 90% of the back scattered γ- and X-rays emerge in Au, Sn and Fe backscattering Mössbauer spectroscopy. Calculated values according to Equation 5.10.

Sample	50%	90%
metallic Au	46 μm	200 μm
metallic Sn	18.2 μm	72 μm
metallic Fe	5.5 μm	18.6 μm

The results clearly show how the higher energy γ-rays of gold penetrate deeper into the sample compared to the γ-rays of tin and iron. For samples consisting of alloys or compounds, the penetration depth has to be calculated taking into account the f-factor, the density of the Mössbauer nuclei and the total photoelectric absorption coefficient of the particular sample material. Especially for tin compounds at room temperature the f-factor is usually much higher than for the very soft metallic tin, while the total photoelectric absorption coefficient depends mainly on the presence of high Z elements.

5.6 The Compton Trick

In case of gold Mössbauer spectroscopy in the backscattering mode, where the spectrum is distorted due to geometry effects, there is also an additional possibility to correctly interpret the measured data, without using $AuAl_2$ as a reference sample.

Figure 5.6 shows the energy spectrum of the detector in the backscattering geometry for a measurement with a 56 μm thick gold foil. The Compton backscattering peak of the 77.3 keV γ-rays can now be used to determine the distribution of scattering angles, since the Compton scattered γ-rays follow the same geometry as the resonantly back scattered radiation. The energy E' of the Compton scattered γ-rays is (Schwabl 1993)

$$\frac{1}{E'} - \frac{1}{E} = \frac{2}{mc^2} \sin^2 \frac{\Theta'}{2}, \tag{5.11}$$

where $E = 77.3\,\mathrm{keV}$ is the energy before scattering and Θ' is the Compton scattering angle. Θ' is in first approximation related to Θ by $\Theta' \approx 180^o - \Theta$ (c.f. Figure 5.4 and 5.5). Here the assumption was made, that back scattered γ-rays run parallel to the symmetry axis of the spectrometer from the sample towards the detector.

The asymmetric Compton peak of the 77.3 keV γ-rays in figure 5.6 can be well fitted by the sum of two gaussian distributions, which can be transformed into an angular distribution for Θ' with the help of Equation 5.11 and the Klein-Nishina cross section for Compton scattering (Davisson 1955)

$$\frac{\mathrm{d}\sigma}{\mathrm{d}\cos(\Theta')} = 2\pi \frac{r_0^2}{2} \left(\frac{E'}{E}\right)^2 \left(\frac{E}{E'} + \frac{E'}{E} - \sin^2\Theta'\right), \tag{5.12}$$

where r_0 is the classical electron radius. The resulting distribution for $\cos\Theta$ is shown in Figure 5.11. Using Equations 5.3 and 5.4, one may now calculate the line positions and line widths corresponding to the different values of $\cos\Theta$ and so create a distribution of lorentzian lines with the relative areas according to Figure 5.11.

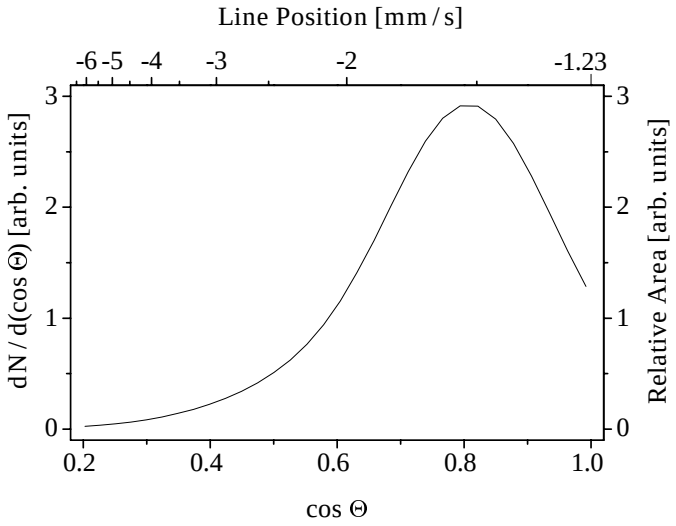

Fig. 5.11: Angular distribution $\mathrm{d}N/\mathrm{d}(\cos\Theta)$ for the γ-rays emitted from the source under the angle Θ and being detected after Compton scattering on the sample. The positions of the Mössbauer line of metallic gold corresponding to the $\cos\Theta$ values is given on the top of the plot.

Figure 5.12 shows the Mössbauer spectrum of a metallic gold foil for which measurement also the pulse height spectrum shown in Figure 5.6 was taken. A distribution of lorentzians according Figure 5.11 was fitted to the Mössbauer pattern in order to obtain the shown envelope. The procedure yielded an isomer shift and a lorentzian line width for the metallic gold foil of $-1.19(1)\,\mathrm{mm/s}$ and $2.36(1)\,\mathrm{mm/s}$, respectively. The isomer shift is in reasonable good agreement with the theoretical value of $-1.23\,\mathrm{mm/s}$. For the interpretation of the line width the broadening by the saturation effect because of the finite sample thickness has to be taken into account. According the simulation shown in Figure 5.10 one expects for this particular foil with a thickness of $56\,\mu\mathrm{m}$ a linewidth of $2.40\,\mathrm{mm/s}$, which is also close to the fitted value.

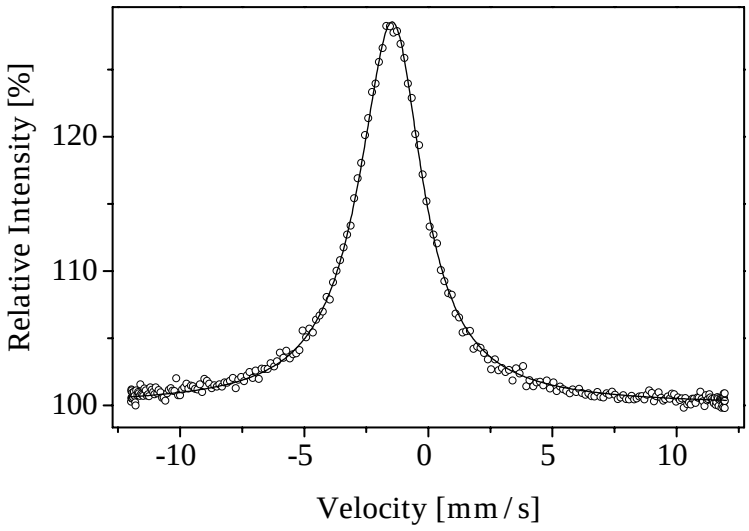

Fig. 5.12: Mössbauer spectrum of a gold foil in backscattering geometry. The fitting procedure is described in the text.

5.7 Magnetic Sextets

In the case of magnetic sextets the total resonant absorption cross section is split into six lines. Usually owing to the random orientation of magnetic domains, the ratio of the intensities from the outer to the inner lines is 3:2:1 (c.f. Section 2.4.2) In the case of backscattering, the different cross sections for the different lines also results in a different probing depth, since for smaller cross sections the saturation depth is reached only in deeper layers. This again results in a change of line intensities, because, for example, the probing volume for the inner lines is bigger than for the outer lines, which leads to an overestimation of the inner lines. A simulation of the magnetic sextet of metallic iron starting with the intensity ratio 3:2:1 for the resonant cross section changes to 2.47:1.78:1 in backscattering mode, which agrees with the experimental result for a metallic iron sample, where the ratio was found to fit to 2.41(3):1.77(3):1.00(1) (c.f. Figure 5.13).

The probing depth is not any more clearly defined in the case of magnetically split spectra, since it is different for the different lines. From the simulation for metallic iron the following can be given: 90% of the total signal are caused by scattering in depths smaller than 20.0 μm and 50% in depths smaller than 5.5 μm.

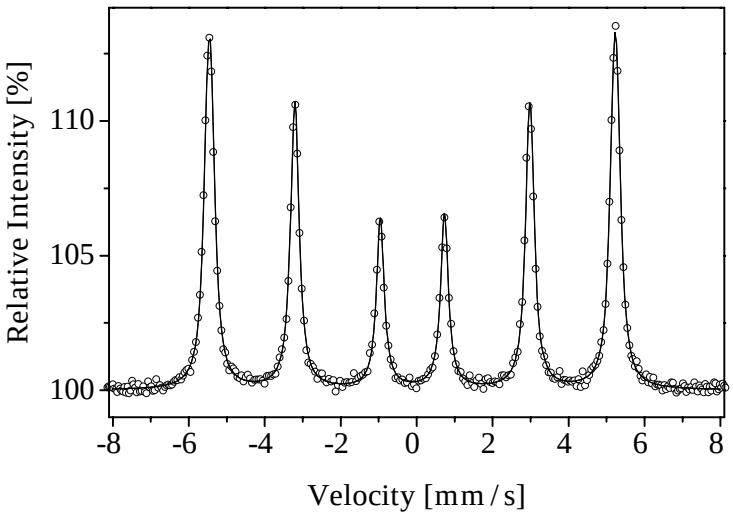

Fig. 5.13: Mössbauer spectrum of natural α-iron in backscattering mode. Purity is 99.998 %, thickness of the foil is 75 μm.

5.8 Summary and Conclusions

Compared to CEMS, Mössbauer spectroscopy in the backscattering mode yields information about a layer which is typically two orders of magnitude larger in thickness and therefore already representative of the bulk material. The probing depths for different materials are compiled in Table 5.2 (c.f. also Table 4.1 for CEMS). In studies of archaeological artefacts, γ-ray backscattering Mössbauer spectroscopy is well suitable to yield information on the bulk material. However, with heavy surface corrosion of an archaeological object cleaning of the surface may be necessary.

The set-ups for the different Mössbauer isotopes are mainly determined by the temperature at which the measurement is performed. Most convenient, in terms of cost and experimental sophistication, are measurements at room temperature, but in the case of gold the measurements have to be done at liquid helium temperature (c.f. Section 2.2). As in the case of CEMS the quality of the spectra depends on the energy resolution of the detector. The better the signal to noise ratio in the pulse height spectrum, the larger the effect in the Mössbauer spectrum. Different filters between source and sample may help to reduce the backscattering of non-resonant radiation into the detector.

The Mössbauer spectra measured in backscattering mode have to be treated carefully because of geometry effects, especially for measurements in the geometry in the liquid helium bath cryostat. In magnetically split spectra, saturation effects must be considered with care.

6 Celtic Gold Coins

6.1 Introduction

Celtic gold coins are among the earliest in central Europe. Most of the coins date back to the Latène age (480-15 BC), which is the apogee of the Celtic culture. Celtic coins provide important information on trade in the Celtic world and on the metallurgical procedures used by the Celts (Ziegaus 1993). This study focuses mainly on the metallurgical aspects of the Celtic gold coinage.

Most of the examined coins were found in Bavaria, southern Germany, and belong to the Prehistoric State Collection, Munich (Kellner 1990, Polenz 1982). They are rainbow cup staters with a usual weight of 7.5(5) g made from Au-Ag-Cu alloys with up to 30 at% silver and copper (Forrer 1908, Paulsen 1933) (Figure 6.1). Not all Celtic gold coins have such high silver and copper contents. However, as will be described later, coins containing much silver and, particularly, copper are of special interest, because both metals must have been added intentionally, and also because peculiarities of the Au-Ag-Cu alloy system must already have played a major role in the making of these coins. The present study tries to contribute to our understanding of how the Celtic metal workers dealt with these problems.

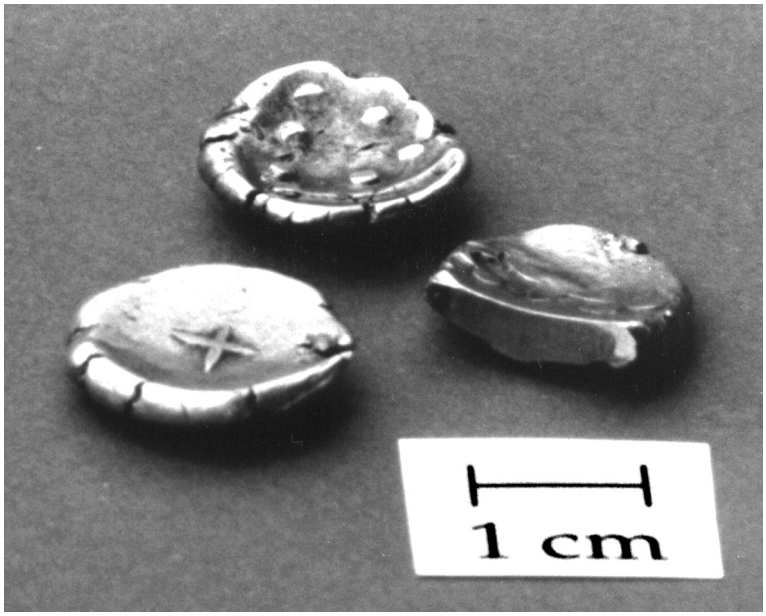

Fig. 6.1: Celtic gold coins S 8.159 (left), No. 2 (right) and G 175 (back).

The blanks, from which Celtic gold coins were struck, were melted individually in coin moulds (Figure 6.2). Usually the measured density of highly alloyed gold coins is smaller than the calculated density from XRF data, which is probing only a surface layer of several micrometer thickness. This indicates a gold enrichment at the surface (Morteani and Martinek 1997, Martinek 1997). In such coins the electron microprobe analysis indeed reveals a depletion of silver and copper in a surface layer of, in some cases, more than 100 μm (Lehrberger 1997). Up to now it is not clear whether the depletion is up to a special treatment during the production of the coins, or to leaching of the less noble metals during underground burial. To elucidate this point has been one of the maintains of the present study.

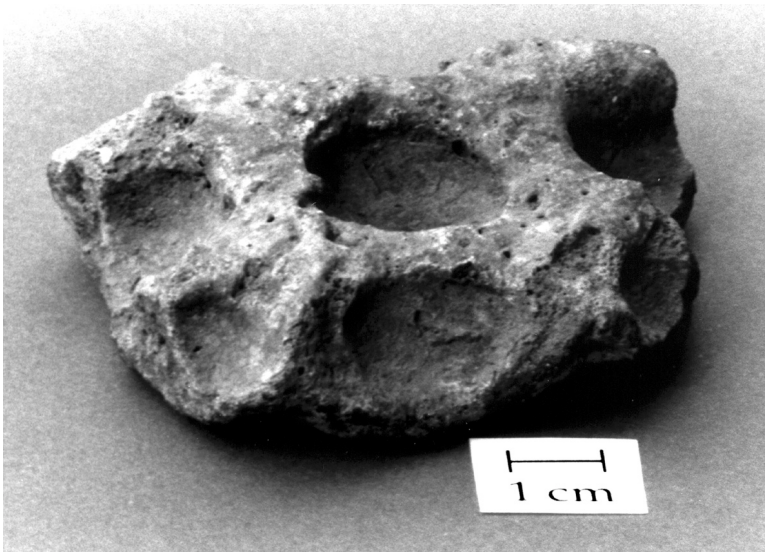

Fig. 6.2: Fragment of a mould used for the production of Celtic gold coins.

An introduction to the alloys from which the coins are made, will be followed by a description how Mössbauer spectroscopy can be used to study these alloys. Then a hypothesis will be presented how the coins were produced from the blanks. To support this hypothesis the results of Mössbauer measurements and other techniques on Celtic Gold coins are then compiled and compared with results of measurements on some reference materials.

6.2 Gold-Silver-Copper Alloys

6.2.1 Ternary Phase Diagram and Crystal Structure

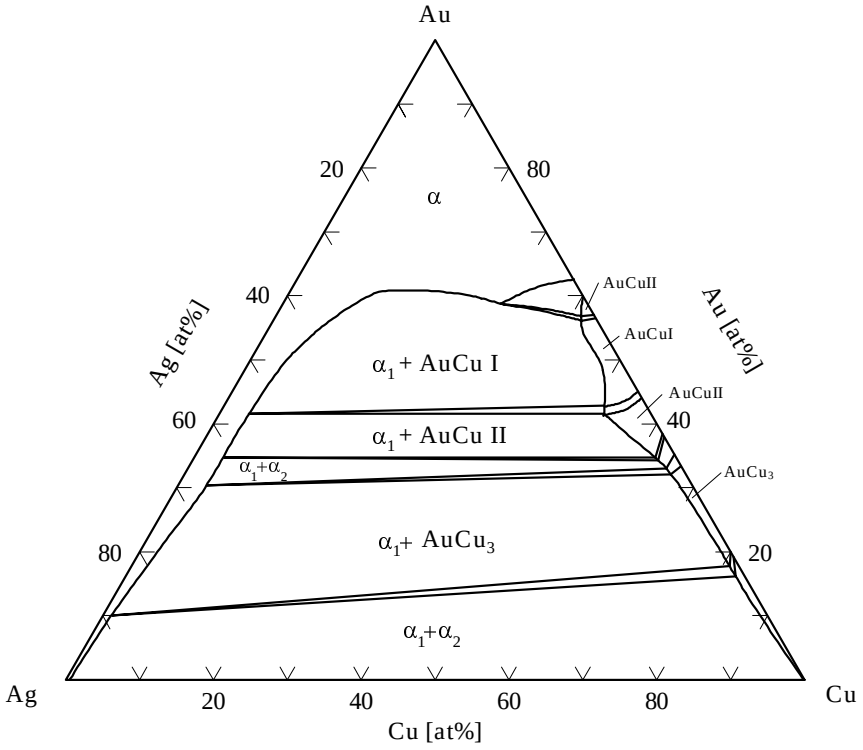

Fig. 6.3: Ternary phase diagram at 300 °C for Au-Ag-Cu alloys adapted from Prince *et al.* (1990). α: disordered alloy, α_1: silver rich disordered alloy, α_2: copper rich disordered alloy.

While binary Au-Ag alloys form a continuous series of solid solutions at all temperatures above 300 K (Hansen 1958), the Ag-Cu system exhibits a miscibility gap below 779.1 °C (Subramanian and Perepezko 1993). These properties of the binary systems are reflected by the ternary phase diagram of the Au-Ag-Cu system, which has been reviewed by Prince *et al.*(1990). Figure 6.3 shows the equilibrium phase diagram at 300 °C. One sees how the miscibility gap in the Ag-Cu system spills over into the ternary phase diagram, so that there happens a phase separation of the high temperature α-phase alloy into a silver rich phase α_1 and a copper rich phase α_2 below temperatures of 767 °C. The structure of the disordered alloys α, α_1 and α_2 is face centred cubic, with the lines of constant lattice parameter running virtually parallel to the Ag-Au edge in the ternary phase diagram (Prince *et al.* 1990). Therefore Vegard's law (Vegard 1928) gives a good approximation for the lattice constant as a function of the atomic composition of the alloy: Since the lattice parameter of pure Au ($a = 4.078$ Å) and of pure Ag ($a = 4.086$ Å) (Prince *et al.*1990) are close to each other, the lattice constant

depends to a good approximation only on the copper content. For pure Cu the lattice constant ($a = 3.615\,\text{Å}$) is about 10% smaller than for Au and Ag. With 4 atoms per unit cell and the densities of the pure elements ($\rho_{\text{Au}} = 19.32\,\text{g/cm}^3$, $\rho_{\text{Ag}} = 10.50\,\text{g/cm}^3$ and $\rho_{\text{Cu}} = 8.95\,\text{g/cm}^3$ (Stöcker 1993)), one can obtain the expected lattice parameter (or better yet, the unit cell volume) as a function of the silver and copper content:

$$a^3 = 4u \cdot \left(z\frac{A_{\text{Au}}}{\rho_{\text{Au}}} + x\frac{A_{\text{Ag}}}{\rho_{\text{Ag}}} + y\frac{A_{\text{Cu}}}{\rho_{\text{Cu}}} \right), \tag{6.1}$$

where $u = 1.66054 \cdot 10^{-24}\,\text{g}$ is the atomic mass unit, $A_{\text{Au}} = 196.97$, $A_{\text{Ag}} = 107.87$ and $A_{\text{Cu}} = 63.55$ are the atomic weights of the three elements in multiples of the atomic mass unit and z, x and y are the atomic contents in $\text{Au}_z\text{Ag}_x\text{Cu}_y$ alloys, with $x + y + z = 1$. Inserting the numerical values of the constants the above formula can also be written as

$$a^3 = 67.72 + 0.52 \cdot x - 20.55 \cdot y \qquad [\text{Å}]. \tag{6.2}$$

From this relation one directly sees the minor dependence of a^3 on the silver content compared to the dependence on the copper content. From the fcc crystal structure of the Au-Ag-Cu disordered alloys one expects a typical 5 line X-ray diffraction pattern, with lines at $a/\sqrt{3}$, $a/\sqrt{4}$, $a/\sqrt{8}$, $a/\sqrt{11}$, $a/\sqrt{12}$, where a is the lattice parameter.

Below 390 °C Au-Cu intermetallics may precipitate from the copper rich alloy α_2. This usually coincides with a purification of copper rich α_2-phase from dissolved silver. In detail the reactions are $\alpha_2 \rightleftharpoons \alpha_1 + \text{AuCu}_3$ at 387 °C, $\alpha_2 \rightleftharpoons \alpha_1 + \text{AuCuII}$ at 374 °C and $\text{AuCuII} \rightleftharpoons \alpha_1 + \text{AuCuI}$ at 358 °C. A remainder of α_2 may also decay in a ternary four-phase reaction $\alpha_2 \rightleftharpoons \alpha_1 + \text{AuCuII} + \text{AuCu}_3$ at 280 °C (for details see Prince *et al.*(1990) and the references therein). Small amounts of silver are soluble in the intermetallic compounds, lowering the precipitation temperatures as compared to the binary Au-Cu system (Hultgren and Tarnopol 1939, Kogachi and Nakhigashi 1985).

AuCu I has a face centred tetragonal structure, where alternate (002) planes are occupied either only by gold or by copper atoms. AuCu II has a faulted AuCu I structure (Pearson 1967). It may be thought of as consisting of 10 tetragonal AuCu I unit cells placed side by side in the b-direction, with the occupancy of (001) planes changing from all gold atoms to all copper atoms halfway along the new long cell (Yasuda 1987). AuCu_3 has a face centred cubic structure with copper on the face sites.

According Yasuda (1987) the precipitation of Au-Cu intermetallics is responsible for the age-hardening phenomenon, which occurs when Cu-rich Au-Ag-Cu alloys are annealed at temperatures around 300 °C.

6.2.2 ^{197}Au Mössbauer Pattern

The charge density at a given gold nucleus depends mainly on the population of the nearest neighbour sites around the gold nucleus. For a gold nucleus in a disordered ternary alloy with a cubic structure this yields a dependence of the isomer shift on the number of Au, Ag and Cu atoms on the 12 nearest neighbour sites. Although the fcc crystal structure is per se highly symmetric the local symmetry around a gold atom

may be distorted because of the different sizes of the Au, Ag and Cu nuclei. This would yield a field gradient at the gold nucleus and therefore a quadrupole splitting in the Mössbauer pattern. However, it turns out that this quadrupole splittings are small enough in a way that the Mössbauer spectra can be well described as a single line (Figure 6.4).

To determine the dependence of the mean isomer shift and the broadening of the Mössbauer line on the Ag and Cu concentrations, seventeen different alloys were melted in an arc furnace and cold rolled to foils with a total thickness of several 10 mg/cm^2. The isomer shifts IS and gaussian broadening σ of the fitted voigt profile (c.f. Section 3.3) are given in Table 6.1. The lorentzian width was assumed to be 1.89 mm/s, which is the natural linewidth according the half life of the first excited state of the gold nucleus.

Tab. 6.1: Isomer shift IS, gaussian broadening σ, Au-content of the sample and relative f-factor f_{rel} as compared to metallic gold for various Au-Ag-Cu alloys.

Alloy	IS [mm/s]	σ [mm/s]	Au-content [mg/cm^2]	f_{rel}
Au_{100}	−1.233(3)	0.13(2)	25.0(2)	1
$Au_{96}Cu_4$	−1.108(2)	0.373(6)	29(1)	-
$Au_{79}Ag_8Cu_{13}$	−0.597(4)	0.508(8)	21.8(3)	-
$Au_{75}Ag_{25}$	−0.772(4)	0.38(1)	6.7(2)	1.13(3)
$Au_{74}Cu_{26}$	−0.273(2)	0.603(4)	22.3(3)	-
$Au_{59}Ag_{29}Cu_{12}$	−0.198(3)	0.551(6)	23.4(9)	0.96(4)
$Au_{56}Ag_{21}Cu_{23}$	0.076(2)	0.631(4)	22.4(5)	0.97(2)
$Au_{41}Ag_{43}Cu_{16}$	0.253(5)	0.577(8)	21(1)	0.94(5)
$Au_{39}Ag_{37}Cu_{24}$	0.449(5)	0.601(8)	21.2(4)	0.95(2)
$Au_{38}Ag_{31}Cu_{31}$	0.629(3)	0.635(5)	24(1)	0.92(4)
$Au_{35}Ag_{65}$	0.086(9)	0.41(2)	6.2(2)	1.09(3)
$Au_{33}Ag_{33}Cu_{34}$	0.801(3)	0.623(5)	18.2(4)	0.99(3)
$Au_{25}Ag_{75}$	0.286(9)	0.39(2)	7.7(2)	1.02(3)
$Au_{25}Ag_{60}Cu_{15}$	0.544(4)	0.523(9)	14.0(8)	-
$Au_{25}Ag_{40}Cu_{35}$	1.035(3)	0.680(4)	18.3(6)	-
$Au_{25}Ag_{20}Cu_{55}$	1.446(3)	0.644(6)	20.4(5)	1.09(3)
Au_4Cu_{96}	2.701(1)	0.285(7)	9.5(4)	-

The isomer shift of the alloys can be fitted linearly to the silver and copper concentrations, x and y:

$$IS = -1.23 + 1.99(3) \cdot x + 4.06(4) \cdot y \qquad \text{[mm/s]} \tag{6.3}$$

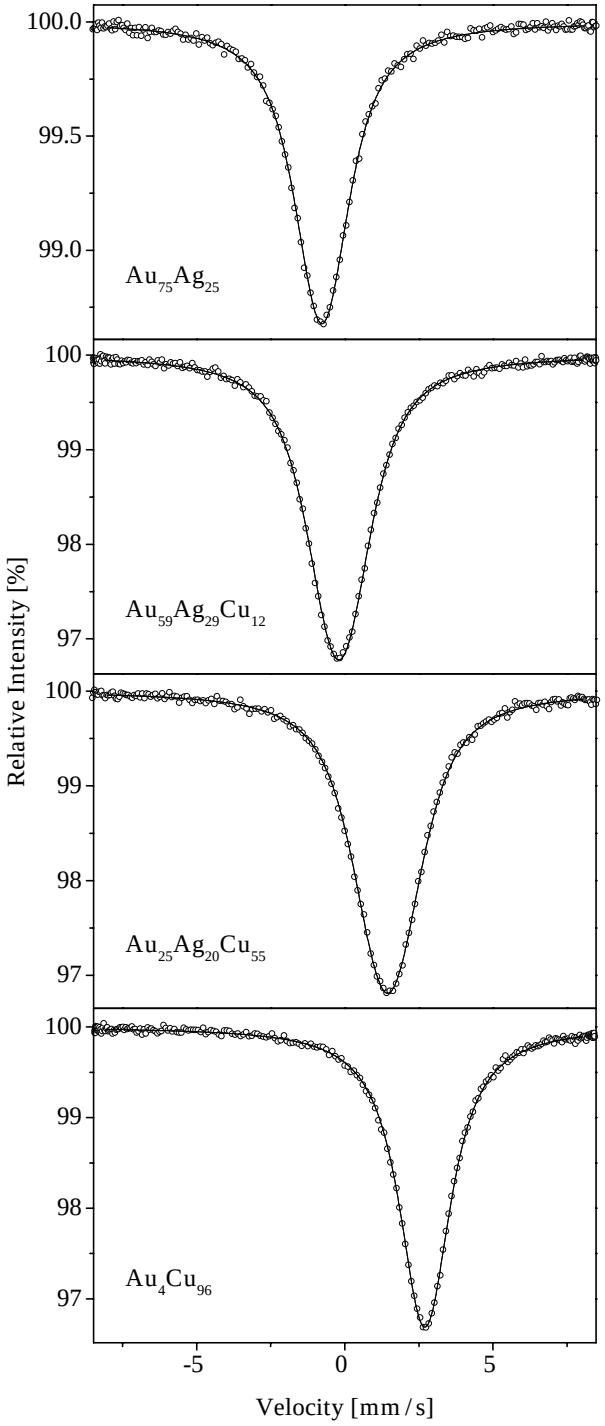

Fig. 6.4: Transmission Mössbauer spectra of four different gold alloys, melted in an arc furnace and cold rolled to foils.

The isomer shift of pure gold ($x = y = 0$) is $-1.23\,\mathrm{mm/s}$ (Cohen 1978).

For binary Au-Ag and Au-Cu alloys Huray *et al.* (1971) already gave an explanation of the linear dependence of the isomer shift on the alloy composition in terms of average atomic volume. Basing on this work Kuhn *et al.* (1994) explained the isomer shift in

such binary alloys as an effect of a redistribution of 5d electrons of the gold to the 6s state. However, with the results compiled in Table 6.1 it can be shown that also for ternary alloys the isomer shift can be given as a linear function of both, the silver and the copper content (Equation 6.3). Obviously the presence of silver does not influence the change in the electron charge density at the probe nucleus caused by copper and vice versa.

For the line shape a more detailed model than fitting voigt profiles can be implemented by fitting a trinomial distribution of lorentzian lines to the broadened single line. This model assumes that (i) only nearest neighbours affect the isomer shift of any gold atom in the alloy, that (ii) the shift induced by any neighbour depends only on which element (Au,Ag or Cu) the neighbour is, but not on the other neighbours and that (iii) there is no short range order. The model further neglects quadrupole splittings arising from the non-cubic environment that possibly results from the distribution of different elements around the probe atom. In the disordered alloy a gold atom is surrounded by a certain configuration of gold, silver and copper atoms, the number of which are trinomially distributed. For a total number n of equivalent sites the occupation of a certain number of sites i_j with the element $j = 1, \ldots, k$ has to fulfil the relation (Graham *et al.* 1990)

$$1 = (x_1 + \ldots + x_k)^n = \sum_{\substack{0 \le i_1, \ldots, i_k \le n \\ i_1 + \cdots + i_k = n}} \binom{n}{i_1, \ldots, i_k} \cdot {x_1}^{i_1} \cdots {x_k}^{i_k}. \tag{6.4}$$

The $x_1, \ldots, x_k$ are the probabilities for a certain element j to occupy a certain site with $\sum_{j=1}^{k} x_j = 1$. For the i_j the relation $\sum_{j=1}^{k} i_j = n$ must hold. The multinomial coefficient can be written as a product of binomial coefficients:

$$\binom{\mathrm{n}}{\mathrm{i}_1, \ldots, \mathrm{i}_\mathrm{k}} = \frac{\mathrm{n}!}{\mathrm{i}_1! \cdots \mathrm{i}_\mathrm{k}!} = \binom{\mathrm{i}_1 + \cdots + \mathrm{i}_\mathrm{k}}{\mathrm{i}_2 + \cdots + \mathrm{i}_\mathrm{k}} \binom{\mathrm{i}_2 + \cdots + \mathrm{i}_\mathrm{k}}{\mathrm{i}_3 + \cdots + \mathrm{i}_\mathrm{k}} \cdots \binom{\mathrm{i}_{\mathrm{k}-1} + \mathrm{i}_\mathrm{k}}{\mathrm{i}_\mathrm{k}}. \tag{6.5}$$

In the case of ternary gold alloys there are $n = 12$ equivalent sites in the nearest neighbourhood of any gold atom and $k = 3$ for a Au-Ag-Cu alloy. The probabilities x_{Au}, x_{Ag} and x_{Cu} are identical with the z, x and y values defining the alloy composition.

From Equation 6.4 the probability w for a special occupation of the next neighbourhood sites by i_{Au} gold, i_{Ag} silver and i_{Cu} copper neighbours ($i_{\mathrm{Au}} + i_{\mathrm{Ag}} + i_{\mathrm{Cu}} = 12$) becomes:

$$w(i_{\mathrm{Au}}, i_{\mathrm{Ag}}, i_{\mathrm{Cu}}) = \binom{12}{i_{\mathrm{Au}}} \binom{12 - i_{\mathrm{Au}}}{i_{\mathrm{Ag}}} {x_{\mathrm{Au}}}^{i_{\mathrm{Au}}} {x_{\mathrm{Ag}}}^{i_{\mathrm{Ag}}} {x_{\mathrm{Cu}}}^{i_{\mathrm{Cu}}} \tag{6.6}$$

For the isomer shift of a gold atom with such a neighbourhood one expects a lorentzian line with a fraction of the total intensity of $w(i_{\mathrm{Au}}, i_{\mathrm{Ag}}, i_{\mathrm{Cu}})$ at a position

$$IS'(i_{\mathrm{Au}}, i_{\mathrm{Ag}}, i_{\mathrm{Cu}}) = -1.23 + a' \cdot \frac{i_{\mathrm{Ag}}}{12} + b' \cdot \frac{i_{\mathrm{Cu}}}{12} \qquad [\mathrm{mm/s}]. \tag{6.7}$$

Ninety-one different nearest neighbour configurations are possible, each of which contributes to the measured Mössbauer line with the respective intensity $w(i_{\mathrm{Au}}, i_{\mathrm{Ag}}, i_{\mathrm{Cu}})$.

A simultaneous fit of the spectra of the seventeen alloys given in Table 6.1 with the constants a' and b' as common parameters yields these constants as

$$a' = 1.978(3) \qquad \text{and} \qquad b' = 4.060(2). \tag{6.8}$$

The broadening of the lines is now explained by the different positions of the ninety-one contributions to the total lineshape. From the common fit one also finds that the best value for the lorentzian linewidth is $LW = 2.061(3)$ mm/s, which is slightly more than the natural linewidth of 1.89 mm/s (c.f. Table 2.1). The larger actual linewidth may be due to broadening by finite absorber thickness of the foils.

The f-factor of ^{197}Au bound in such ternary alloys was also determined in frame of this work by the use of a reference absorber, but no unequivocal correlation was found between the f-factor and the silver and copper content. The f-factor was found to be within the range of $\pm 10\,\%$ of the f-factor of metallic gold (Table 6.1).

AuCu (I and II) and $AuCu_3$

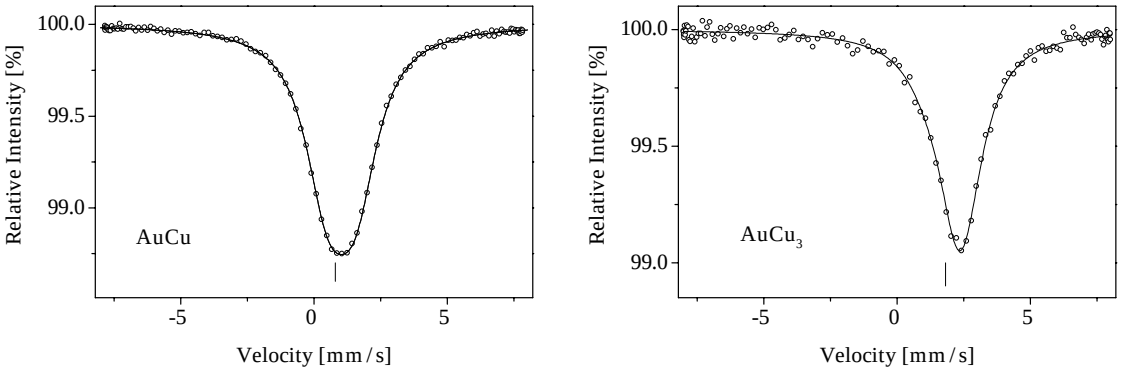

Fig. 6.5: Mössbauer pattern of the ordered AuCu and $AuCu_3$ intermetallics. The small lines at 0.8 mm/s and at 1.8 mm/s indicate the position of the lines as expected from Equation 6.3 for the disordered alloys of same composition. Compared to the narrow line of $AuCu_3$, the Mössbauer pattern for AuCu clearly exhibits a unresolved doublet structure.

Due to previously discussed short range order the Mössbauer pattern of the intermetallic Au-Cu compounds cannot be explained by Equation 6.3. One can not distinguish between AuCu I and AuCu II, however, since Mössbauer spectroscopy is not sensitive to long range order effects. Due to the broken cubic symmetry of the lattice, the electric field gradient will not vanish, although the actual quadrupole splittings may be small like in the disordered Au-Ag-Cu alloys, where the cubic symmetry is also broken due to the random distribution of the three elements. For the compositions of AuCu and $AuCu_3$ foils were prepared as described above, but finally annealed in an argon atmosphere for 2 h at 410 °C and at 400 °C, respectively. The gold content of the two samples were 10.1(2) mg/cm^2 and 4.4(1) mg/cm^2, respectively. The spectra are shown in Figure 6.5. AuCu was found to have an isomer shift of 1.026(4) mm/s and a quadrupole splitting of 1.04(1) mm/s. The gaussian broadening of the fitted voigt profile was 0.21(2) mm/s, with a lorentzian width fixed to 1.89 mm/s. The structure of $AuCu_3$ is cubic, so one

still expects a single line. The isomer shift of Au in $AuCu_3$ was 2.36(3) mm/s and the gaussian width 0.15(9) mm/s, with a lorentzian width again fixed to 1.89 mm/s. The isomer shifts for AuCu and $AuCu_3$ found in this work agree well with the isomer shifts that were obtained by Huray *et al.* (1971). However, this authors do not give any value for the quadrupole splitting in AuCu.

6.2.3 Combined Techniques

As can be seen from Equations 6.2 and 6.3, both the lattice parameter and the isomer shift are functions of the silver and the copper concentration. Figure 6.2 shows lines of constant lattice parameters a and constant isomer shifts IS, as well as lines of constant density ρ in the ternary phase diagram, as calculated from Equations 6.2 and 6.3.

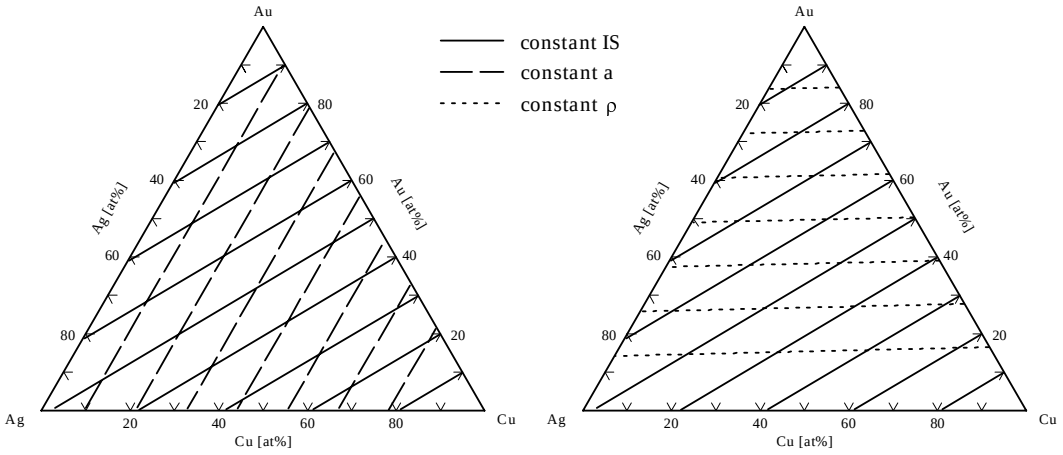

Fig. 6.6: Ternary phase diagram for Au-Ag-Cu alloys with lines of constant isomer shift IS and constant lattice parameters a (left) and constant isomer shift IS and constant density ρ (right).

For the determination of the composition of the bulk material in the interior of the coin, which can be thought of as representing the initial alloy composition before any kind of surface treatment, one may measure two of the three mentioned quantities and obtain the composition from the point of intersection of the corresponding lines in Figure 6.6. The knowledge of the bulk composition is important for a correct interpretation of the results from surface sensitive probing techniques, like XRF or CEMS. The difficulties which arise in assessing the bulk properties will be discussed later.

6.3 Model for the Production of Celtic Gold Coins

Gebhard *et al.* (1997) give a description of the production of the blanks from which the Celtic gold coins were struck: Small pieces of raw alloy and/or more or less pure gold, silver, and copper or bronze were put into moulds of a diameter of about 2 cm, which were made of clay (c.f. Figure 6.2). The moulds were covered with glowing charcoal and put into a furnace, into which air could be blown with bellows. After a few minutes the metal melted and formed small ingots of the right size for a coin. After cooling these ingots could be flattened with a hammer. For the further processing of such blanks into coins the following hypothetical model is proposed here, which explains the surface enrichment of gold in alloyed coins as resulting from the procedures used in the manufacture of the coins.

The blanks were left in the furnace until this was cooled down completely. After the flattening with the hammer, some of the blanks were re-heated for some hours at temperatures about $700 - 800\,^{\circ}\mathrm{C}$ in contact with sodium chloride to deplete them from silver and copper. The depleted blank was struck between a front and a back stamp to get it into its final shape which is typical for the rainbow cup staters. The coins were polished, annealed again in the fire and quenched. Quenching into an acidic solution would remove remainders of metallic or oxcidic copper from the surface.

For the acidic solution there are two possibilities suggested (Rauscher 1996): Sulphuric acid, for example from a mixture of alumn and sodium chloride, or organic acids from fruits also with addition of sodium chloride.

6.4 Measurements on Gold Coins

The studied coins were selected from the inventory of the Prehistoric State Collection Munich for their high copper and silver content, as well as for a large difference in density measured gravimetrically and that calculated from XRF data for their composition. The data from Morteani and Martinek (1997) and Lehrberger (1997) for this coins are compiled in Table 6.2. The coins are parts of hoards as indicated in Table 6.2 (Sontheim: Ziegaus 1993b, Großbissendorf: Ziegaus 1995, Wallersdorf: unpublished). Coin No. 2 is without archaeological context. It was bought for an earlier project (Morteani and Martinek 1997) and cut for having a look onto the bulk of the coin. The coins S 8.159, No. 2 and G 175 are shown in Figure 6.1.

The ^{197}Au Mössbauer spectra were taken at 4.2 K in liquid helium bath cryostats. Since the studies had to be non-destructive and the coins were too thick for transmission experiments, backscattering (BS) experiments detecting the resonantly scattered 77.3 keV gamma rays (c.f. Chapter 5), and conversion electron Mössbauer studies (CEMS) (c.f. Chapter 4) were performed.

Figure 6.7 shows the CEMS and backscattering spectra of four typical Celtic gold coins.

Tab. 6.2: Composition, densities and weight of the studied Celtic gold coins. ρ_{XRF} is the density calculated from the XRF composition, ρ_{A} is the density measured gravimetrically.

Coin	Au [at%]	Ag [at%]	Cu [at%]	ρ_{XRF} [g/cm^3]	ρ_{A} [g/cm^3]	m [g]
No. 2	40	36	24	14.0	13.2	7.504
Sontheim S 1.2	60	27	13	15.86	14.89	7.731
Sontheim S 3.44	61	27	12	15.93	14.60	7.835
Sontheim S 4.71	50	31	19	14.94	14.46	7.772
Sontheim S 4.74	54	28	18	15.26	13.93	7.859
Sontheim S 4.75	55	28	17	15.40	12.92	7.804
Sontheim S 8.159	54	28	18	15.27	10.83	6.601
Großbissendorf G 175	55	28	17	15.42	13.21	7.143
Wallersdorf W 175$_{K3436}$	60	26	14	15.82	15.67	7.875

The CEMS spectra consist of an alloy component near zero velocity and a shoulder at $-1.23\,\mathrm{mm/s}$, the isomer shift of metallic gold. The probing depth in CEMS is about $2.2\,\mu\mathrm{m}$ (c.f. Section 4.3.2). The backscattering spectra appear as a broadened single line and the component attributable to metallic gold is missing. The broadening exceeds the values given in Table 6.1 and is due to saturation effects (c.f. Chapter 5).

In the backscattering mode the coins were measured together with a $AuAl_2$ reference (c.f. Figure 5.7), whose contribution has been subtracted in Figure 6.7 for the sake of clarity. The relative area of the alloy component of all coins as compared to the area of the component due to the $AuAl_2$ reference was 70(2)%, which is 88(3)% of the signal measured for a 0.5 mm thick scatterer of metallic gold replacing the coins (79.5(2)% relative effect) in the same geometry. This decreased effect can be explained by the lower gold concentration in the coins. When the gold content is lower the total photo absorption mechanism becomes more important compared to the resonant absorption. For a reference alloy with the composition $Au_{54}Ag_{27}Cu_{19}$, which is similar to that of most of the examined coins, the density of gold nuclei is only 54% compared to metallic gold, while the total photo absorption coefficient $30.15\,\mathrm{cm}^{-1}$ (calculated from the data given by Storm 1970) is only slightly decreased compared to the value for metallic gold (c.f. Table 5.1). Using these values to calculate the magnitude of the resonance effect according to Section 5.5, it turns out that the saturation effect is indeed 89% of the effect calculated for metallic gold, although the saturation depth is larger, since the γ-rays penetrate further into the material with the smaller total absorption coefficient. When the probing depth in such highly alloyed coins is calculated according Section 5.5, the thickness of the layer from which 50 and 90% of the signal emerge is 66 and $302\,\mu\mathrm{m}$, respectively. The corresponding values for pure metallic gold are given in Table 5.2.

Since the shoulder in the CEMS spectra due to pure gold is absent in the backscattering spectra, it must arise from metallic gold at the surface of the coins. This gold would give only an insignificantly small contribution to the γ-ray backscattering and hence be practically invisible in the γ-ray backscattering spectra. To test this proposition, coin No. 2 was covered in two CEMS experiments with a 10 and $30\,\mu\mathrm{m}$ thick mylar

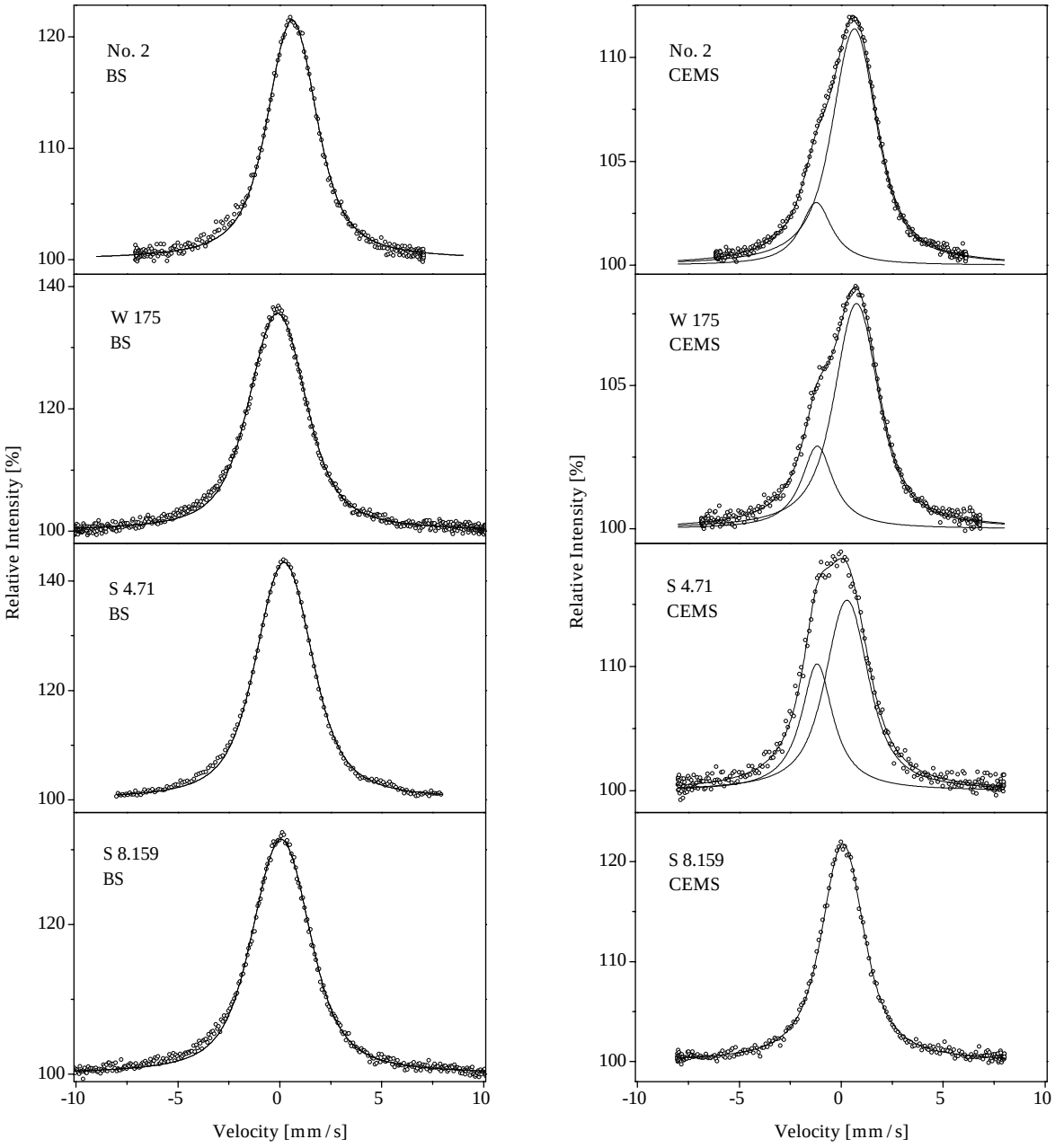

Fig. 6.7: γ-ray backscattering (BS) and conversion electron (CEMS) Mössbauer spectra of the Celtic gold coins No.2, W 175, S 4.74 and S 8.159.

foil, respectively. The idea behind this experiments was that electrons which come from deeper layers and lost already some energy, will be stopped in the mylar, so that the technique becomes even more surface sensitive. A problem is that the overall effect also decreases. Indeed in the measurements with the foils the contribution of the metallic gold signal to the spectrum raises from 22(1)% (without foil) to 26(1)% (10 μm foil) and 29(1)% (30 μm foil), respectively. This results confirm the notion that the metallic gold is sitting directly on the surface, but does not cover it totally, otherwise one would expect a stronger effect for the experiment with the 30 μm foil compared to the

experiment with the 10 μm foil. Assuming a homogenous surface layer of metallic gold, this layer would have to be only about 0.3 μm thick (compare section 4.3.2). Moreover, also in the electron microscope the regions, where the alloy is depleted of silver and copper could be seen in the back scattered electron image as light areas (Figure 6.8). A grey scale analysis of Figure 6.8 yields that the gold rich areas covers about 1/3 of the evaluated surface areas of the coin, which is in agreement with the CEMS covering experiments.

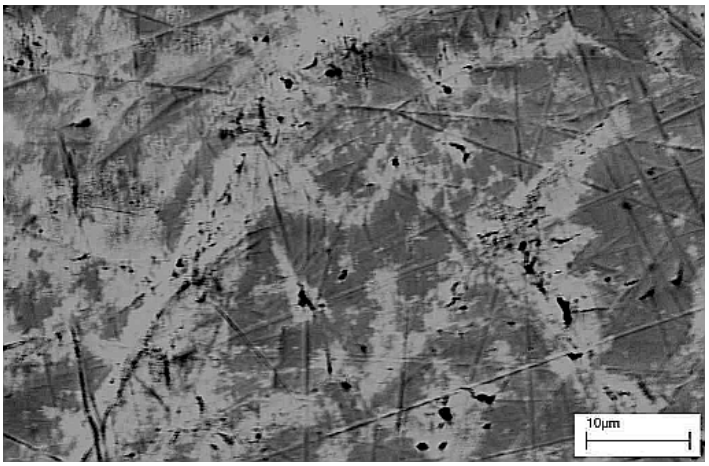

Fig. 6.8: Back scattered electron image in the scanning electron microscope from coin No. 2. Light areas are rich in heavy elements, dark areas rich in light elements. By electron microprobe analysis the light areas could be proofed to consist of nearly pure metallic gold, with only insignificant traces of silver and copper.

Table 6.3 gives the composition of the coins from XRF (Morteani and Martinek 1997) and the measured isomer shifts.

For the reference alloy $Au_{54}Ag_{27}Cu_{19}$ the penetration depth of the rhodium K_α radiation, which was used by Morteani and Martinek (1997) for the XRF analysis, can be calculated with the data given in Storm (1970) to be 20 μm. Thus XRF probes a depth of about 20 μm. The isomer shifts calculated from the XRF composition and Equation 6.3 are in most cases closer to the isomer shifts of metallic gold than the isomer shifts from the Mössbauer backscattering experiments, which practically probe the bulk. This again demonstrates the enrichment of gold near the surface.

Another interesting feature can be seen in Table 6.2: The isomer shift IS_{CEMS} of the alloy component in CEMS is often more positive than IS_{BS} in backscattering mode. The precipitation of metallic gold on the surface from the initially disordered alloy, leaves a rest of alloy, which is depleted in gold and thus has a more positive isomer shift. In particular cases this may depend on whether the formation of the metallic gold layer was going along with a loss of copper through oxidation.

The gold shoulder in the CEMS spectra has also been seen in the X-ray diffraction pattern of coin No. 2 (Figure 6.9). Fitting this pattern with two fcc components yields lattice parameters of 3.9536(1) Å and 4.07332(7) Å, respectively. The latter value is close to the lattice parameter of metallic gold (4.078 Å, Prince *et al.* 1990). For the

Tab. 6.3: Composition and isomer shifts of Celtic gold coins. The isomer shift IS_{XRF} is calculated with Formula 6.3 from the XRF composition. ΔIS is the difference of IS_{BS} (BS for back-scattering) and IS_{XRF} and $\mathrm{Au}_{\mathrm{CEMS}}$ the contribution of metallic gold to the CEMS spectrum.

Coin	Au [at%]	Ag [at%]	Cu [at%]	IS_{XRF} [mm/s]	IS_{CEMS} [mm/s]	IS_{BS} [mm/s]	ΔIS [mm/s]	$\mathrm{Au}_{\mathrm{CEMS}}$ [%]
No. 2	40	36	24	0.49	0.73(1)	0.60(1)	0.11(1)	22(1)
S 1.2	60	27	13	−0.17	−0.20(5)	−0.10(1)	0.07(1)	23(4)
S 3.44	61	27	12	−0.21	−0.16(7)	−0.09(1)	0.12(1)	16(6)
S 4.71	50	31	19	0.15	0.23(2)	0.21(1)	0.06(1)	32(1)
S 4.74	54	28	18	0.07	0.20(1)	0.15(1)	0.08(1)	20(1)
S 4.75	55	28	17	0.01	0.21(2)	0.15(1)	0.14(1)	12(1)
S 8.159	54	28	18	0.05	0.08(1)	0.06(1)	0.01(1)	-
G 175	55	28	17	0.01	0.03(1)	0.02(1)	0.01(1)	-
W 175	60	26	14	−0.13	−0.12(3)	−0.12(1)	0.01(1)	3(2)

cut coin No. 2 also a X-ray diffraction pattern of a cut face could be taken from the bulk. This was a single phase fcc-pattern with a lattice parameter of 3.97434(8) mm/s. According Section 6.2.3 this yields together with the isomer shift from the backscattering experiment a composition of the bulk material of $\mathrm{Au}_{0.340(9)}\mathrm{Ag}_{0.409(5)}\mathrm{Cu}_{0.251(7)}$.

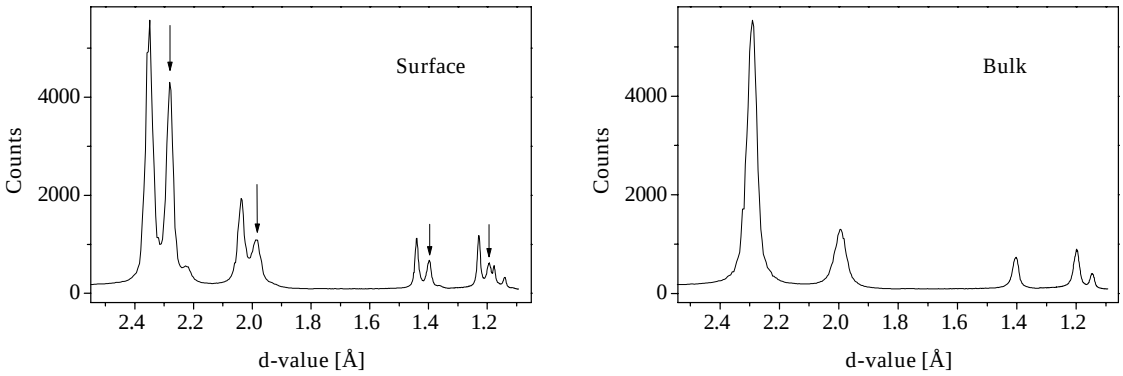

Fig. 6.9: X-ray diffraction pattern of the surface and the bulk of the Celtic gold coin No. 2. The the main peaks at higher d-values are due to metallic gold on the surface. The peaks indicated with an arrow are due to an alloy phase. The diffractograms were taken on a Siemens GADDS system.

From an earlier project (Morteani and Martinek 1997) there were also some sliced coins on which line scans with an electron microprobe were performed perpendicular to the surface of the coin. One of these scans is shown in Figure 6.10. One clearly sees that gold is enriched in the uppermost 20 μm.

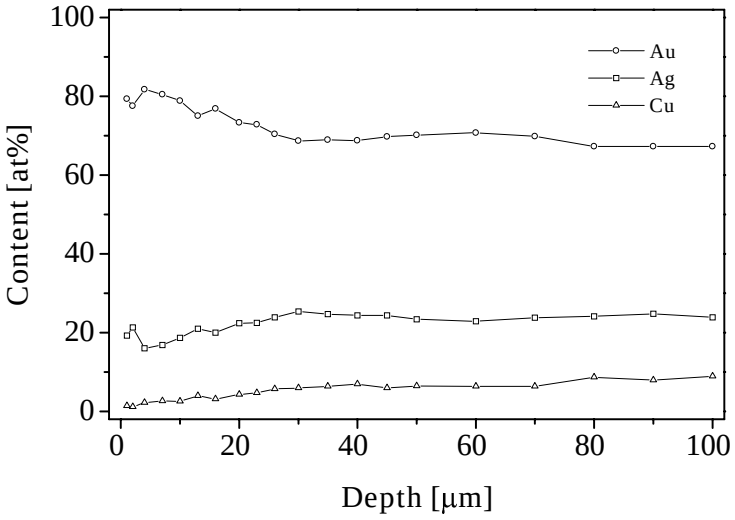

Fig. 6.10: Depth profile of electron microprobe analysis data on a sliced coin (from Lehrberger 1997).

6.4.1 Density Measurements

According to Equation 6.3, the differences in the isomer shifts ΔIS, calculated from the XRF composition and measured in the Mössbauer backscattering experiments, of generally less than $IS = 0.1\,\mathrm{mm/s}$ (Table 6.2) can be explained by a difference in the copper content of about 2.5 at% or a difference in the silver content of about 5 at%, which does not explain the observed low densities in a satisfactory manner. Presumably, light inclusions and voids in the bulk of the coins often tend to lead to erroneous values for the bulk density.

Lehrberger *et al* (1997) measured the densities gravimetrically of the coins by Archimede's principle. In a number of cases (c.f. Table 6.2), these densities are so much lower than those calculated from the XRF analysis of the coin surfaces that a certain amount of porosity must be assumed to explain them. Therefore for some coins the density was re-measured in the present work by a different technique based on the displacement of helium gas for measuring the volume of the coins. The advantage of helium gas is that it will readily enter at least those pores in the coin material that are connected to the surface by cracks or capillaries. The device used for this measurements is shown schematically in Figure 6.5.

The procedure of a measurement was as follows: After evacuating the whole system carefully for 30 min to remove all air from accessible pores, it was refilled to about 1 bar with helium gas. This pressure p_i was measured with a MKS Baratron Pressure Meter 170M unit with a MKS 310BHS-10000 Pressure Head. Then valve 1 was closed and the rest of the system (including the manometer) was again evacuated. Valve 2 was then closed and valve 1 was opened so that the gas in the sample chamber $(V_i - V_{\mathrm{Coin}})$ could expand also into the rest of the system and the manometer with the total Volume V_f, which gave the final pressure p_f. Boyle-Mariotte's law yields:

$$p_i \cdot (V_i - V_{\mathrm{Coin}}) = p_f \cdot (V_f - V_{\mathrm{Coin}}) \tag{6.9}$$

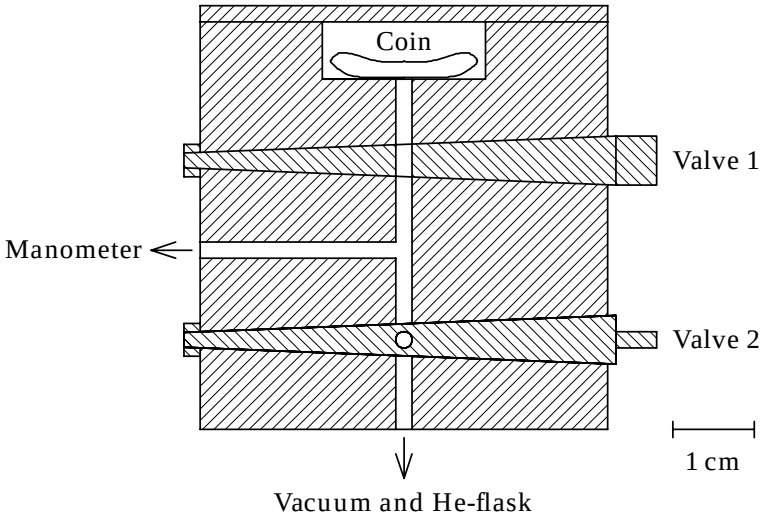

Fig. 6.11: Device for the determination of the volume of coins.

or

$$V_{\mathrm{Coin}} = \frac{V_i p_i - V_f p_f}{p_i - p_f}. \tag{6.10}$$

The constant volumes V_i and V_f can be derived from calibration measurements with objects of known volume. For the particular set-up used one thus obtains:

$$V_{\mathrm{Coin}} = \frac{3.170\,\mathrm{cm}^3 \cdot p_i - 21.93\,\mathrm{cm}^3 \cdot p_f}{p_i - p_f} \tag{6.11}$$

The standard derivation for repeated measurements of the resulting density of standards and coins was about $0.1 - 0.2\,\mathrm{g/cm}^3$.

Coin No. 2 is a coin that was cut once. The electron microprobe analysis of the bulk material gives an average density of $\rho_{\mathrm{bulk}} = 13.5\,\mathrm{g/cm}^3$. The measured density from this set-up was also $13.5\,\mathrm{g/cm}^3$.

The coins S 8.159 and G 175 are remarkable because here the calculated isomer shift from the XRF and the measured isomer shift in the Mössbauer backscattering mode nearly coincide, which indicates a homogenous material. Both coins do not show a significant shoulder contributable to metallic gold in the CEMS spectrum. Table 6.4 gives the densities of this coins.

Tab. 6.4: Densities for the three Celtic gold coins for which the density was determined by the He gas method. ρ_{XRF} is the calculated density from X-ray fluorescence analysis, ρ_{A} is the density measured by Lehrberger *et al* (1997) and ρ_{He} is the density measured in this work.

Coin	ρ_{XRF} [g/cm^3]	ρ_{A} [g/cm^3]	ρ_{He} [g/cm^3]
no.2	14.0	13.2	13.5
G 175	15.4	13.2	14.1
S 8.159	15.3	10.8	13.9

Coin S 8.159 was outgassing: In repeated experiments, the final pressure continued to increase over a period of more than 10 minutes, which means that the coin had He gas inclusions from which the gas was emitted slowly through capillaries. Isolated gas inclusions would not be observed by this method. The measured density will then be smaller than the density calculated from XRF data. Such gas inclusions are probably the reason why the densities of the coins S 8.159 and G 175 do not reach the expected value from the material analysis, although these coins do not exhibit any appreciable surface enrichment of gold. In the cases, like those of G 175 and S 8.159, it is always helpful to have at least two independent methods (for example X-ray fluorescence analysis and Mössbauer spectroscopy) to check, as far as possible, the homogeneity of the alloys.

6.4.2 Summary of Experimental Results on Celtic Gold Coins

In summary, the following effects can be observed for Celtic gold coins:

- The measured density does not agree with the density calculated from XRF data. This is in part due to the surface enrichment of the gold, but probably in many cases even more to pores and voids.
- Microprobe line profiles on the cut face of a coin show enrichment of gold within several 10 μm of the surface.
- The line observed in Mössbauer backscattering mode is at higher isomer shift than suggested by the XRF analysis. This is due to the larger probing depth of Mössbauer backscattering.
- In most cases a shoulder appears at the low velocity side of the CEMS spectra. This shoulder is attributable to the formation of metallic gold on the surface.
- Covering experiments in CEMS and backscattered electron images from electron microscopy show that the metallic gold does not cover the surface completely, but only a minor fraction. This suggests that there probably happened a phase separation into a copper rich phase and a silver rich phase, where the copper from the copper rich phase partially oxcidiced and metallic gold remained.
- The two phases on the surface can also be seen in XRD patterns, while a XRD bulk measurement is in agreement with the Mössbauer backscattering pattern, which show a single phase for the bulk.

It is worth mentioning that neither in backscattering mode nor in CEMS measurements was there any segregation observed of a AuCu ordered phase due to age-hardening as indicated by Yasuda (1987). Also in the X-ray diffraction patterns of coin No. 2, such ordered phases could not be seen.

6.5 Measurements on Reference Materials

For the formation of the metallic gold component on the surface of some of the Celtic gold coins, there are two conceivable classes of mechanisms that should be considered, namely (i) an intentional or unintentional treatment by man, or (ii) the influence of the moist soil during two thousand years of burial. The former would include phase separation due to heat treatment during the production of the coins and leaching effects due to the reaction of the alloy with acidic fluids. By various physical and chemical treatments of model Au-Ag-Cu alloys, one can try to obtain the surface enrichment of gold observed for the Celtic coins. Some experiments of this kind will be described in the following sections.

6.5.1 Heating in Sodium Chloride or Pickling

Three foils with a thickness of about 30 μm and two ingots of about 5 mm size were kept in intimate contact with powdered sodium chloride at 600 °C for 2 and 18 hours, respectively. After this treatment electron microprobe line scans across the polished cut face perpendicular to the surface, and transmission Mössbauer spectra were taken of the foils. The compositions of the foils were $Au_{80}Ag_{20}$, $Au_{80}Cu_{20}$ and $Au_{50}Ag_{30}Cu_{20}$. Figure 6.12 shows the shift of the Mössbauer line towards metallic gold over time with the treatment.

Table 6.5 gives the average composition of the foils from the electron microprobe line scans and the isomer shifts. Both techniques show that after 18 h the copper has been almost completely removed, while a substantial amount of silver still remains.

Tab. 6.5: Average composition (from electron microprobe) and isomer shifts of alloys after treatment in NaCl at 600 °C.

Alloy	IS [mm/s]	after 2h	IS (2h) [mm/s]	after 18h	IS (18h) [mm/s]
$Au_{80}Cu_{20}$	-0.496(2)	$Au_{90}Cu_{10}$	-0.7352(7)	$Au_{98}Cu_2$	-1.1704(7)
$Au_{80}Ag_{20}$	-0.851(2)	$Au_{91}Ag_9$	-0.938(1)	$Au_{93}Ag_7$	-1.030(1)
$Au_{50}Ag_{30}Cu_{20}$	0.166(2)	$Au_{63}Ag_{27}Cu_{10}$	-0.220(1)	$Au_{84}Ag_{15}Cu_1$	-0.691(1)

In the ingots the situation is different in that there is a practically inexhaustible reservoir of Cu and Ag in the interior. This situation is certainly closer to that in a coin than the thin foils can be. Figure 6.13 shows an electron microprobe line scan perpendicular to a pickled ingot surface (18 h at 600 °C in NaCl). The pickled ingot of Figure 6.13 had the same initial composition as the coin of Figure 6.10. The similarity of the effect of pickling on the ingot with what is observed for the Celtic gold coin is obvious.

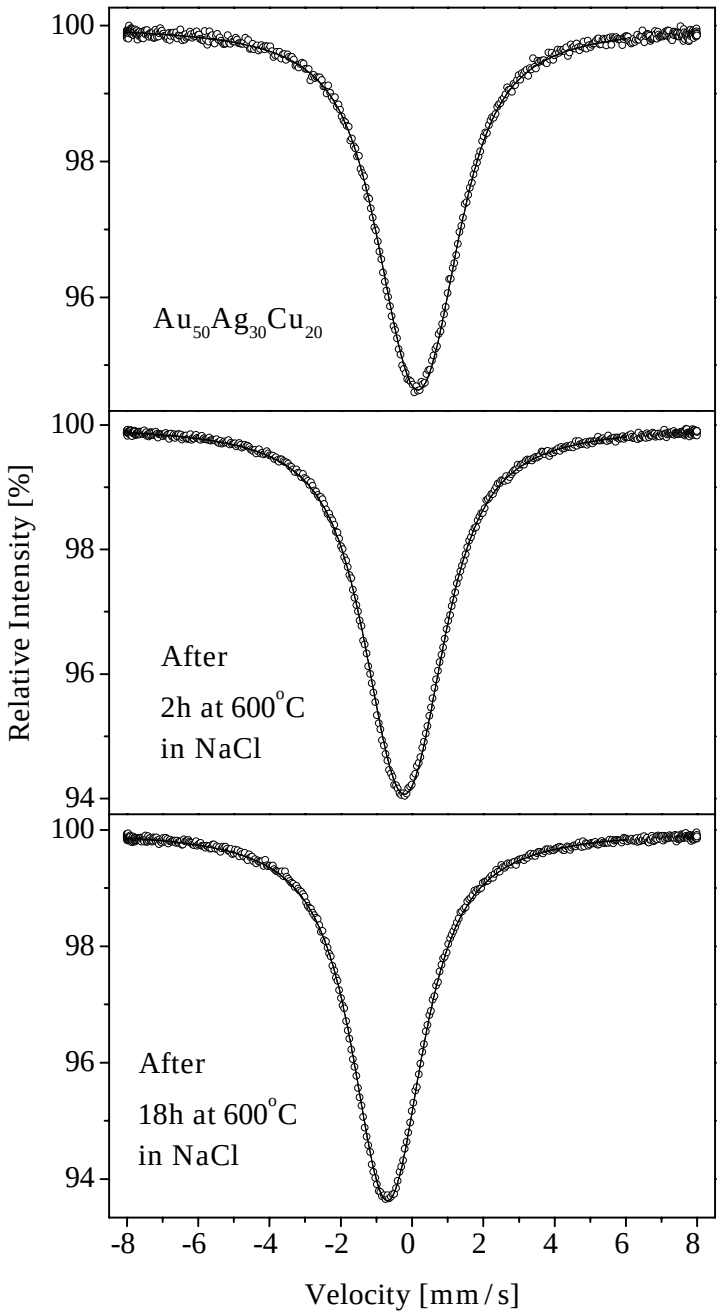

Fig. 6.12: Transmission Mössbauer spectra of $Au_{50}Ag_{30}Cu_{20}$ treated at 600 °C in NaCl.

Oxidation at 600 °C in air without the presence of NaCl was found to remove the copper, which forms an oxide layer on the surface, but not the silver: Five alloys (Table 6.6) were oxidiced in air for 5 min at 600 °C. After this the copper oxide was washed of from the foils with nitric acid and electron microprobe linescans were taken on the surface. The resulting Au:Ag:Cu ratios are given in Table 6.6. After oxidation there is typically an overestimation of the silver content as compared to the gold content. This means that the silver is not necessarily removed at all by the oxidation process and even more that some gold must have been removed. This can be explained by the

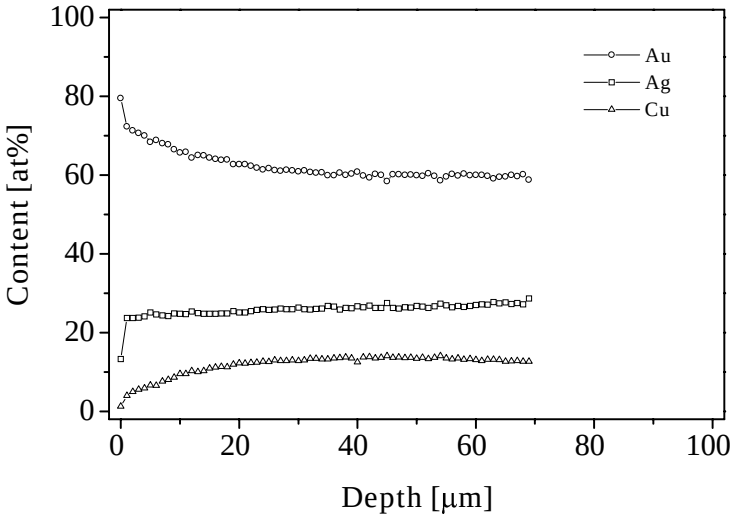

Fig. 6.13: Composition from an electron microprobe line scan perpendicular to the pickled surface of a nugget.

assumption that the oxidation of the copper takes place preferably in regions of high copper concentration. Here also small amounts of gold will be washed of together with the copper oxide. In regions with a high silver concentration the oxidation would be neglegible.

Tab. 6.6: Au:Ag:Cu ratios as determined by electron microprobe measurements of five ternary alloys before and after oxidation in air. The values are normaliced to the atomic gold concentration.

Alloy	Au:Ag:Cu before oxidation	Au:Ag:Cu after oxidation
$Au_{40}Ag_{20}Cu_{40}$	1.00(28):0.48(21):1.03(29)	1.00(24):0.70(20):0.09(08)
$Au_{40}Ag_{30}Cu_{30}$	1.00(10):0.70(10):0.70(10)	1.00(14):0.87(13):0.13(04)
$Au_{40}Ag_{40}Cu_{20}$	1.00(16):0.94(16):0.52(12)	1.00(21):1.00(21):0.08(07)
$Au_{50}Ag_{20}Cu_{30}$	1.00(14):0.37(09):0.64(11)	1.00(22):0.48(15):0.06(07)
$Au_{50}Ag_{30}Cu_{20}$	1.00(13):0.57(10):0.39(09)	1.00(30):0.60(23):0.05(12)

Thus the surface depletion of both copper and silver observed frequently for Celtic gold coins (Lehrberger 1997) can be emulated by pickling the alloy in sodium chloride, but not merely by heating in air. In other experiments it could be shown that leaching in nitric or sulphuric acids does not remove the silver or copper from the disordered ternary alloy. Figure 6.14 shows the two spectra of $Au_{25}Ag_{60}Cu_{15}$ before and after washing in 1 molar (!) nitric acid for 19 h. The hyperfine parameters are equal within the experimental error. Especially there is no shift, broadening or asymmetry observed. Obviously the acid has no effect on the disordered ternary alloy.

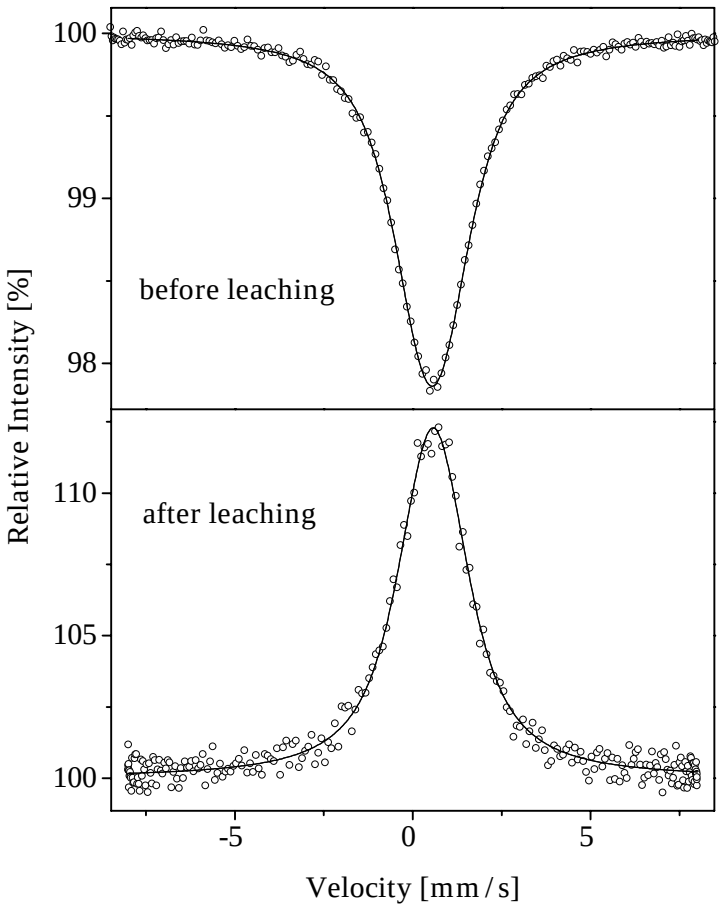

Fig. 6.14: Transmission Mössbauer spectrum of $Au_{25}Ag_{60}Cu_{15}$ before leaching and CEMS data of the same alloy after 19 h leaching in 1 molar nitric acid.

6.5.2 Annealing

By annealing ternary Au-Ag-Cu alloys, one expects to induce a phase separation into a silver rich and a copper rich phase according to the ternary phase diagram (Figure 6.3). To study this, five arc melted alloys (Table 6.7) were cold rolled and sealed into quartz tubes under hydrogen gas to avoid any oxidation of the surface. They were put into a furnace at 750 °C and then slowly cooled down with a cooling rate of about 100 °C/h. This would approximately be the cooling rate if coin blanks in the coin moulds were left to cool inside the furnace after the melting. Isomer shifts of the foils before and after annealing are given in Table 6.7. After annealing the samples were measured in CEMS experiments to avoid line broadening due to sample thickness.

Since the mean silver and copper content of the samples is constant under the conditions of annealing, the shift to more positive velocities can only be due to the concentration of the gold in a phase or phases richer in copper than the starting alloys, for instance as a consequence of the formation of AuCu and/or $AuCu_3$. That AuCu is, indeed, formed, can also be shown by X-ray diffraction: After annealing all the samples show diffraction peaks from the intermetallic compound AuCu II. (Figure 6.15

Tab. 6.7: Isomer shifts of 5 alloys before and after heating to 750 °C and slow cooling to room temperature.

Alloy	IS (cold rolled) [mm/s]	IS (annealed) [mm/s]
$Au_{40}Ag_{20}Cu_{40}$	0.780(6)	0.972(5)
$Au_{40}Ag_{30}Cu_{30}$	0.573(6)	0.708(5)
$Au_{40}Ag_{40}Cu_{20}$	0.356(7)	0.460(7)
$Au_{50}Ag_{20}Cu_{30}$	0.40(2)	0.491(6)
$Au_{50}Ag_{30}Cu_{20}$	0.147(5)	0.248(6)

and Figure 6.16, right).

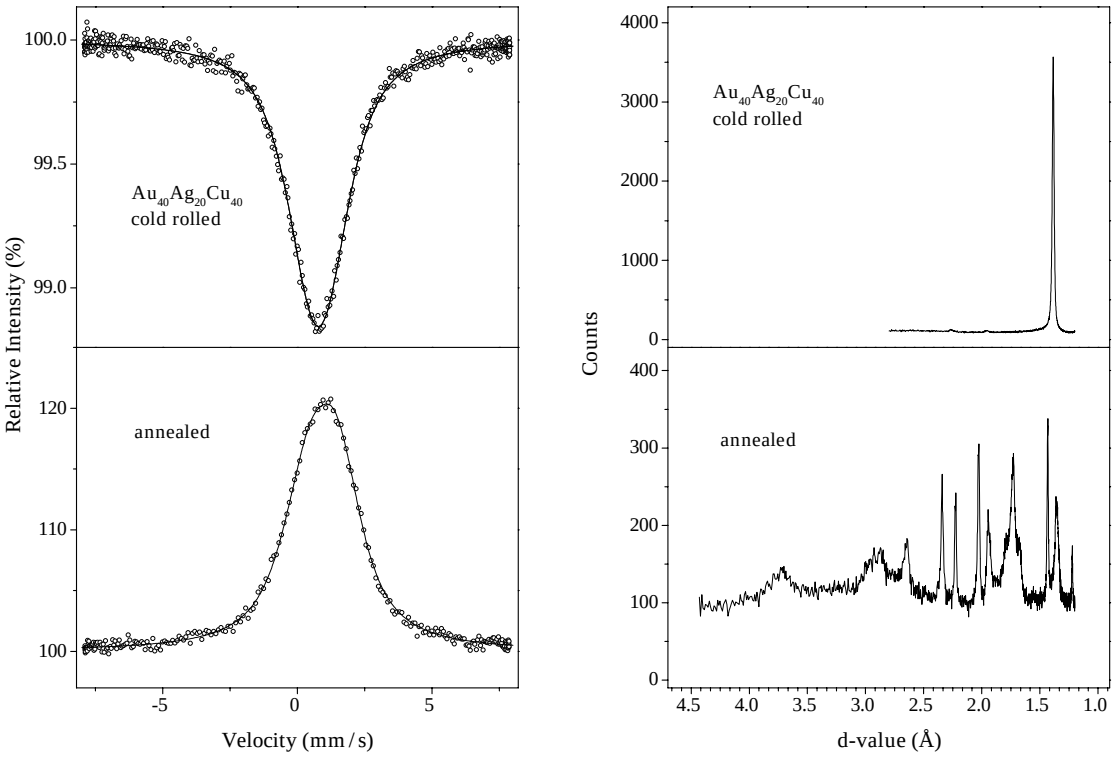

Fig. 6.15: CEMS spectra and XRD patterns of the alloy $Au_{40}Ag_{20}Cu_{40}$ before and after annealing.

Since there was evidence for the presence of AuCu II, the CEMS spectra were also fitted on the basis of the following model: For all the spectra a common component was assumed, which should describe the AuCu II phase. A further component in each spectrum should describe the remaining alloy. The isomer shift and the quadrupole splitting obtained for the AuCu II phase were 1.02(5) mm/s and 1.07(5) mm/s. This values are identical with the values given for the AuCu intermetallic compound in Section 6.2.2. Table 6.8 gives the area of AuCu II and the isomer shift of the remaining alloy after annealing. The fitted spectra are shown in Figure 6.16, left.

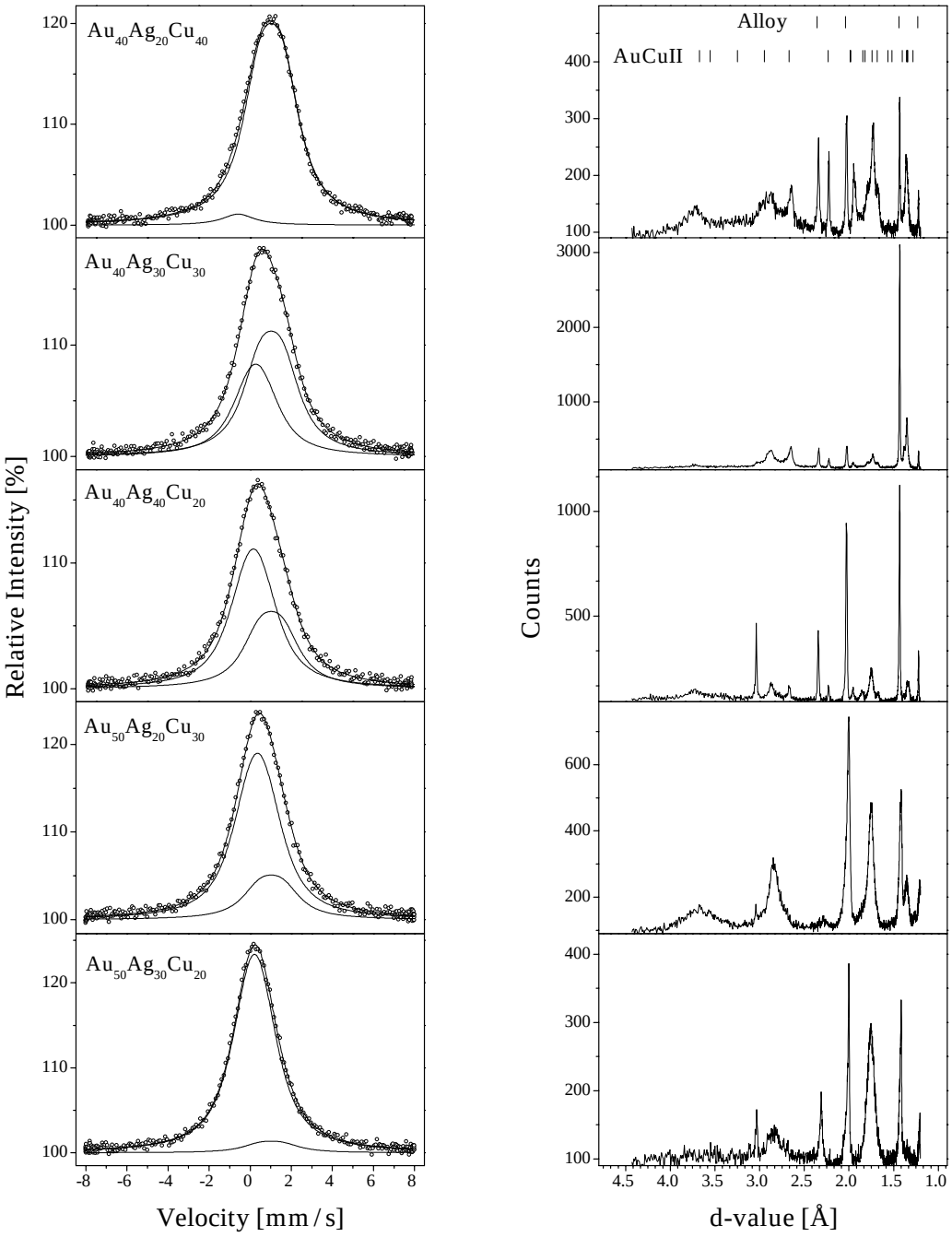

Fig. 6.16: CEMS spectra and XRD patterns of the alloys according Table 6.3 after beeing annealed. The peak in the XRD patterns at 3 Å is due to oxidiced copper.

The results are qualitatively in agreement with the ternary phase diagram. Apparently the AuCu intermetallic is formed more efficiently when the amounts of Au and Cu become equal. When there is much less Cu than Au, the AuCu does not seem to form easily. A quantitative evaluation is difficult due to the possibly different f-factors of the components.

The formation of the copper rich phases may be important for understanding the

Tab. 6.8: Areas of the AuCu II peak in the Mössbauer pattern of the annealed alloys and the isomer shift of the rest that has remained a disordered alloy component.

Alloy	Area [%] AuCu	IS [mm/s] Rest
$Au_{40}Ag_{20}Cu_{40}$	96(4)	-0.6(5)
$Au_{40}Ag_{30}Cu_{30}$	60(3)	0.27(7)
$Au_{40}Ag_{40}Cu_{20}$	38(3)	0.16(4)
$Au_{50}Ag_{20}Cu_{30}$	22(4)	0.35(4)
$Au_{50}Ag_{30}Cu_{20}$	6(3)	0.21(2)

mechanism of forming the pure metallic gold on the surface of the coins: While homogenous Au-Ag-Cu alloys are not affected within a reasonable time by any kind of treatment below 280 °C, the copper rich phases, like the intermetallic AuCu, are. For instance, it was found by CEMS Mössbauer spectroscopy that copper can be leached from the surface of a AuCu foil by boiling for 40 min in sulphuric acid (Figure 6.17).

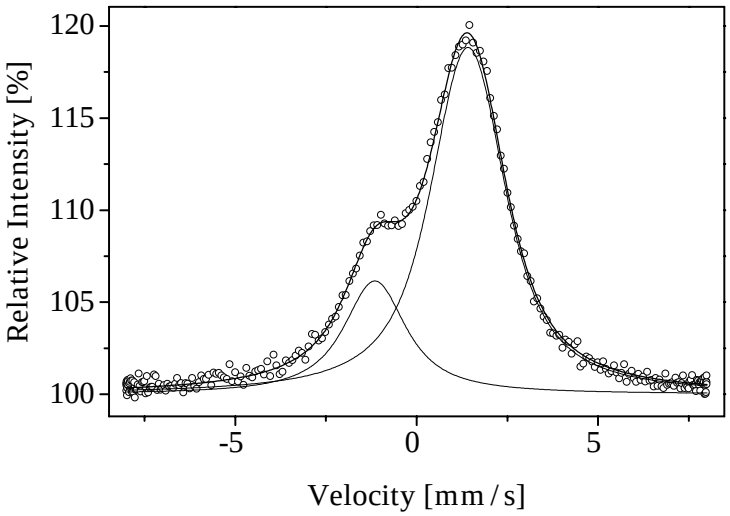

Fig. 6.17: CEMS spectrum of AuCu after boiling for 40 min in H_2SO_4.

6.5.3 Conclusions

The following conclusions can be drawn from the described experiments on reference materials:

- Oxidation of Au-Ag-Cu alloys in air at 600 °C only affects the copper, not the silver.
- Silver can be removed from the initial alloy by heating in contact with sodium chloride, for some hours at 600 °C. The results one gets from this experiment on ingots are very similar to those one gets for Celtic gold coins.
- Leaching in acids does not affect disordered alloys.
- Slow cooling of alloys leads to the precipitation of a AuCu intermetallic compound.

- The copper in the AuCu intermetallic compound can be removed by leaching and/or oxidation, with metallic gold remaining on the surface.

6.6 Summary

Mössbauer studies of Celtic gold coins in the CEMS and BS mode yield information on the alloy composition at the surface and in the bulk. Together with other methods, Mössbauer spectroscopy may also point towards possible mechanisms for the enrichment of gold at the surface of the coins, be it due to special treatments during the production of the coins, or to leaching during underground burial. The CEMS Mössbauer measurements show that typically the coins show a discontinuous layer of pure metallic gold on the surface. A shift of the resonant line observed in BS towards more positive velocities in comparison to the line positions calculated from the XRF composition data can be attributed to higher concentrations of silver and copper in the bulk material.

However, the increased concentration of the less noble components in the bulk compared to the surface explains only a minor part of the difference between the measured mass densities and those calculated from the composition data obtained by XRF. The major reason for the difference in measured and calculated densities seems to be the presence of voids in the coins. This notion is supported by densities determined with a device that works on the basis of helium gas displacement.

The intermetallic compound AuCu was not found in the coins as would be expected from the ternary phase diagram and studies on the age-hardening of Au-Ag-Cu alloys (Yasuda 1987). This shows that one of the last steps in the work of the Celtic craftsmen must have involved quenching from a temperature of about 700 °C. The thin layer of virtually pure metallic gold on the surface of the coins, which gives rise to the shoulder in the CEMS spectra (Figure 6.3) and which has a thickness of some tenths of a micrometer only, would have been worn off in everyday use. This means that either the gold layer formed during the two millennia of underground burial, with acidic solutions in the soil leaching the copper from copper rich phases on the surface, or the coins were not used as currency at all, but only produced as parts of hoards. In the latter case, the gold layer may have resulted from special treatments during the coin production. The majority of Celtic gold coins are, indeed, found in hoards (Ziegaus 1993). There are coins from one and the same hoard and of similar composition, which do not show a significant gold enrichment at the surface (e.g. Coin S 8.159, Table 6.3), while others do. This would indicate that the gold enrichment at the surface occurred during the making of the coins, since it is not plausible that some of the coins in the same hoard have been leached during burial while others have not.

Referring to the hypothetical model for the coin production in Section 6.3 this can now be supported as follows: The slow cooling in the furnace induces a phase separation into a silver rich phase α_1 and a copper rich phase α_2, as well as the precipitation of the AuCu intermetallic compound, according to the ternary phase diagram (Figure 6.3). Heating the blank in contact with sodium chloride would deplete it of silver and copper,

which would explain the electron microprobe line scans given by Lehrberger (1997). After the blank was brought into the the final shape for the rainbow cup stater, it was annealed again in the fire. During this heating the copper at the surface would be oxidised from the copper rich phase and nearly poor metallic gold would remain in these areas. This gold causes the metallic gold shoulder in the CEMS spectra. During the final annealing step the ordered phases would disorder again and homogenize and after quenching the material would stay in the disordered, homogenized state. Quenching into acids would clean the surface from oxidic and metallic copper on the surface.

Finally there are two arguments which indicate that the observed phenomena were intentionally done by the Celtic craftsmen and are not a result of two thousand years of underground burial: (i) The precipitation of AuCu, as referred to as age-hardening, was not observed in the bulk of the examined coins although it would be a necessary preliminary process for the enrichment of the gold on the surface and (ii) there are coins from one and the same hoard, which do not show any leaching effects and for which XRF analysis and Mössbauer spectroscopy are in perfect agreement, while other coins in the hoard show strong effects of surface gold enrichment. Therefore pickling effects due to some kind of intentional treatment as described above have to be considered as the cause of the gold rich surfaces of Celtic gold coins.

7 Ancient Steel

7.1 Introduction

Iron has been used widely for the past three millennia and by many civilisations. Despite attrition by rusting, many iron artefacts for instance from Celtic and Roman times, have survived. Archaeological finds are often heavily corroded, but below layers of iron oxides, the metal is often still present and accessible to scientific studies after removal of the rust.

Until the end of the 19th century AD, practically all the iron was non-alloyed, i.e., no other metals were added to modify its properties, as is usually done today. The mechanical properties of ancient iron and steel were therefore determined solely by the amount of carbon present in the material and by the way in which the iron was worked and heat-treated.

By adding voluntarily or involuntarily carbon to iron, the material becomes harder and is then usually called steel, although the term steel is often used merely as a synonym for iron and not refering to special properties. One composition is of special interest: Pearlitic steel with a carbon content of 3.62 at%. At this composition one gets special properties due to a lamellar microstructure, which is built up of α-Fe and Fe_3C: The material is hard enough for giving a hard blow without breaking and still is easy to forge without burning in the fire.

The methods used by ancient iron makers have, to a large extent, influenced the composition and microstructure of ancient steels. Scientific and metallurgical studies of ancient iron artefacts are therefore of interest to archaeologists. This field has perhaps not found sufficient attention so far. It is therefore surprising that Mössbauer spectroscopy whose most useful isotope is ^{57}Fe, has not been used to study ancient iron artefacts, although it has found wide use in studies of ancient ceramics and has also been used to study the remains of ancient iron-working furnaces (Wagner 2000).

As has already been mentioned, pre-industrial steels are in their vast majority carbon steels. The results of any studies on such steels must therefore be considered with reference to the iron-carbon system and the various stable and metastable phases existing in it. These phases have only been studied with scientific rigour since the late 19th century. Methods of steel working used in earlier times were based entirely and exclusively on the experience of ancient smiths, who kept their crafts often secret. The reconstruction of ancient methods of iron working would appear an important subject for archaeometry, in which metallurgists and scientists should join.

In this chapter a first exploratory Mössbauer study of iron-artefacts from pre-industrial times is presented. The experiments were performed in the backscattering mode using Fe K_α X-rays for detection, since this method, with a probing depth of about 20 μm, is insensitive to thin oxide layers of a few nanometers thickness, which would be present on all iron surfaces exposed to air and influence the results of CEMS experiments decisively. Thicker corrosion layers must, however, always be removed. Mössbauer spectroscopy in backscattering geometry has the further advantage of being non-destructive. Whole iron artefacts like swords can be studied. The backscattering technique avoids not only the removal of a sample from the artefact under study, but also avoids any filing of rolling to produce fine powders or foils for making suitable Mössbauer absorbers. Such mechanical treatments might change the microstructure of the iron in an utterly undesired way.

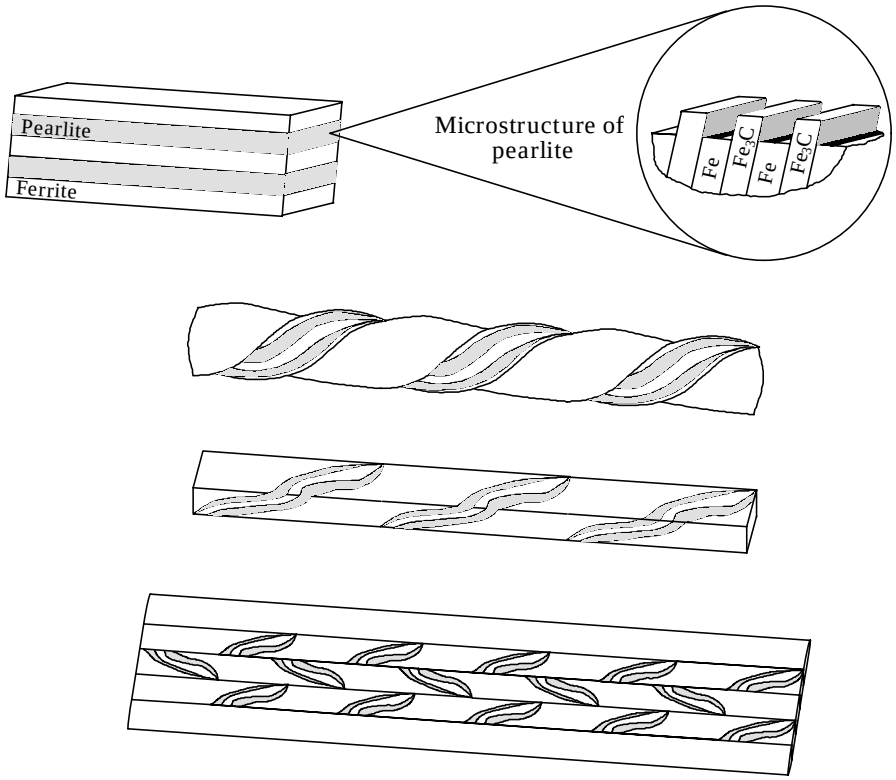

Fig. 7.1: Schematic drawing of the welding of a Damascus steel plate.

A fascinating type of ancient steel is what is now called Damascus steel, which is a composite material of different types of steel, usually of ferrite and pearlite (Höper 1987) in the sense that ferritic layers and pearlitic layers are welded together to form a single bar. Such bars were then often twisted and combined to form plates (Figure 7.1). The combination of soft ferrite and hard pearlite promises a long lasting sword that retains a sharp edge. It is too soft to break and still hard enough not to twist. The ratio of ferrite to pearlite was usually close to one to one, taking for example five ferritic layers and four pearlitic layers. Since pearlite itself contains 3.62 at% carbon bound

in Fe_3C one expects 11.3 at% of the iron bound in Fe_3C, while the rest of the iron in pearlite is ferritic. Combining this pearlite one to one with ferrite one gets 5.7 at% of the iron in Fe_3C only and even less in a combination ratio of five to four.

The term welding is used here in a different sense than it is mostly used in modern iron technology, where it refers to the joining of iron parts by melting the iron locally with a blow torch or an electric arc. The welding of different types of iron to composite steels like Damascus steel is rather done by heating in a charcoal fire and hammering in the hot state, which joins the metal by local sintering processes.

For the description of early steel production see Tylecote (1992). A excellent description of Damascus steel has been given by Sachse (1994).

7.2 The Fe-Fe_3C Phase Diagram

The alloying element, which has the strongest influence on the mechanical properties of steel is carbon. Its importance for the structure of iron at different temperatures can be seen in the iron-carbon phase diagram. Carbon can be either dissolved in the different modifications of iron or it can be in the elementary form as graphite or bound in iron carbide *cementite* Fe_3C, depending on the production process of the steel. Figure 7.2 shows the phase diagram of the metastable Fe-Fe_3C system (Hansen 1958).

The phase diagram of Figure 7.2 illustrates the equilibrium state of the Fe-Fe_3C system and does not take into account the different velocities of quenching which are of much importance in practice. The fcc γ-phase is called *austenite*, the bcc α-phase *ferrite*. Any carbon in excess of the amount soluble in austenite and ferrite will precipitate as the metastable cementite phase. On annealing at temperatures above the line GSK the steel is in the austenitic state. From steel with less than 3.61 at% ferrite precipitates at temperatures between the GS and the PS line, during cooling down from the γ-area. The remaining austenite gets richer in carbon up to the eutectic composition with 3.61 at% carbon and changes to a eutectic mixture with a lamillar structure of ferrite and cementite. This structure is called *pearlite*. Steel with a carbon content higher than 3.61 at% contains cementite already in the temperature range above the GSK line. This dissolves in the austenite or in the melt only at temperatures exceeding the SED line. Cooling this high carbon austenite below the SEF line leads to a precipitation of secondary cementite at the grain boundaries until the carbon content of the austenite is reduced to 3.61 at% at 723 °C. Below the SK line the austenite with the eutectic composition transforms to pearlite. Steels with a carbon content of 3.61 at% cooled down from the γ-area change their structure from austenite to pearlite without a preceding precipitation. All these procedures require a carbon diffusion in the austenite, yielding ferrite in the areas which are poor in carbon and yielding cementite in the areas with high carbon content. When the cooling is too rapid for these diffusion processes to take place, the austenite becomes undercooled. When it eventually transforms to the ferritic structure, the carbon remains in solution and causes a distortion of the lattice from the bcc structure to a body centred tetragonal (bct) one. This phase is called *martensite*.

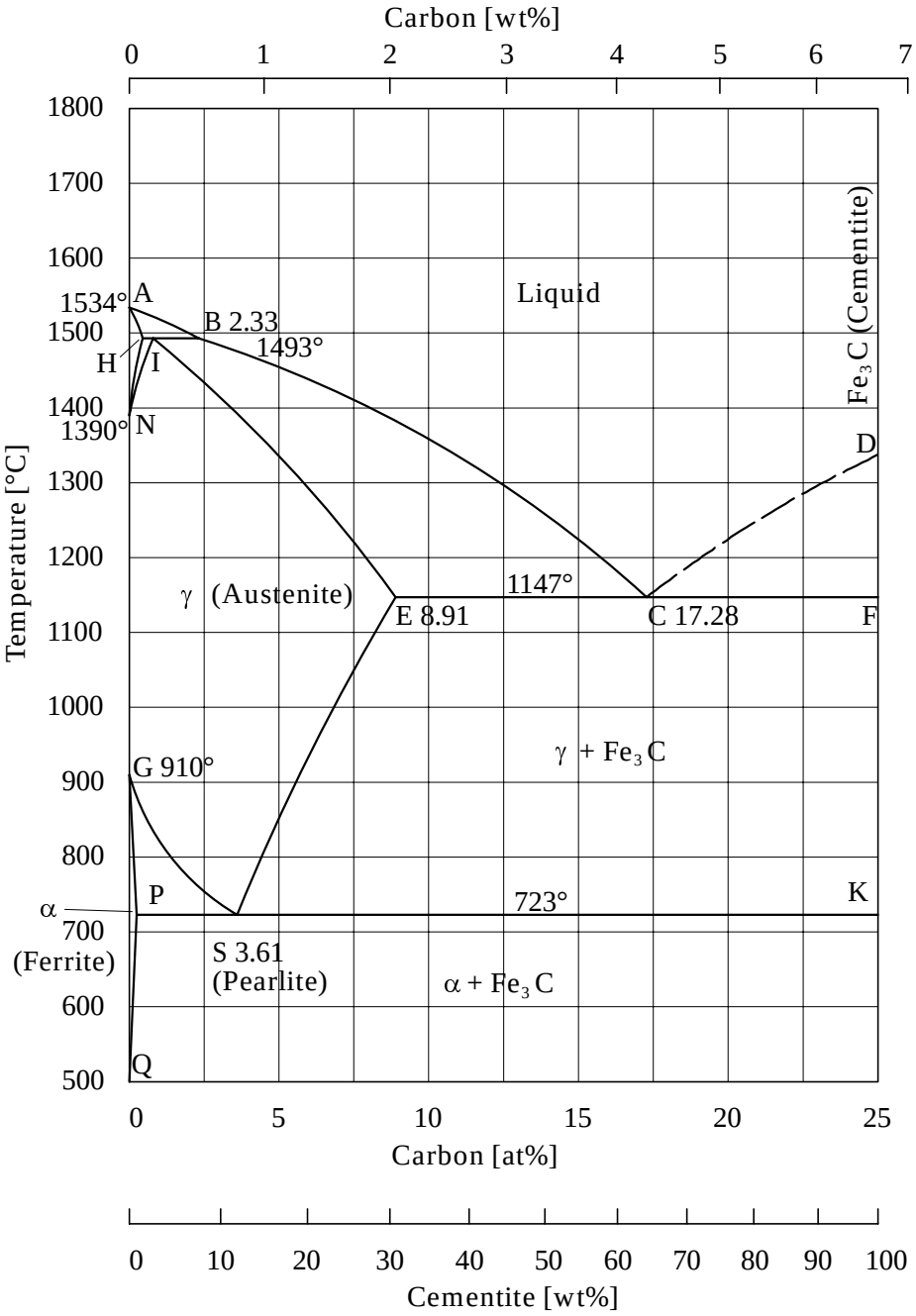

Fig. 7.2: Phase diagram of the metastable Fe-Fe_3C system, adapted from Hansen (1958).

7.2.1 Crystal Structures

The low temperature modification of metallic iron has an body centred cubic structure with a lattice constant of 2.90 Å. Since the solubility of carbon in this bcc ferrite is very restricted, the ferrite phase practically always has the lattice constant and the magnetic transition temperature (768 °C) of pure α-iron (Wever 1924 and Seljakov *et al.* 1927).

If any carbon is dissolved it most probably occupies octahedral interstices.

The crystal structure of pure austenite is face centred cubic with a lattice constant of 3.59 Å (Epstein 1936). The carbon atoms occupy the octahedral interstices (Petch 1942).

The structure of cementite is orthorombic with $a = 4.524$ Å, $b = 5.089$ Å and $c = 6.743$ Å (Jack 1948). Cementite is ferromagnetic, its Curie temperature being at 210–215 °C (Bernier 1951).

Rapid cooling of steel from the austenitic region of the phase diagram yields metastable martensite, which can be considered as supersaturated and distorted ferrite, with a body centred tetragonal lattice ($a = 2.54$ Å and $c = 3.59$ Å) (Kurdjumov and Kaminski 1928). This martensitic transition is a diffusionless shear transition. It is most probable that the carbon atoms in the martensite are in selected octahedral interstices, which are expected if the carbon atoms do not move from the interstices they occupy in the parent phase, austenite (Petch 1943).

7.2.2 Mössbauer Pattern

The Mössbauer pattern of metallic iron (α-Fe) at room temperature is well known to the Mössbauer spectroscopist, because it is usually used for the calibration of the velocity drive. It is a magnetic six line hyperfine pattern with a magnetic splitting corresponding to a hyperfine field of 33.05 T at room temperature, an isomer shift of -0.11 mm/s with respect to a source of ^{57}Fe in a rhodium matrix and a practically zero quadrupole splitting due to the high symmetry in the bcc crystallographic structure.

The high temperature fcc γ-phase of pure iron ($906\,^{\circ}\mathrm{C} \leq T_\gamma \leq 1401\,^{\circ}\mathrm{C}$) gives a non-magnetic single line spectrum (Ron 1980).

Substitution of iron by alloying elements, like chromium, vanadium and others, usually leads to a reduction of the magnetic field in the ferritic phase. Therefore impurities in the lattice show up in the Mössbauer pattern as shoulders on the inner side of the lines of pure metallic iron. Impurities on the order of 0.5 at% can be easily seen in the Mössbauer pattern. Such alloying elements often reduce the temperature of the $\gamma \longrightarrow \alpha$ phase transition. In such cases tempering at moderate temperatures (about 500 °C) and subsequent quenching may yield an austenitic steel. Naturally found alloying elements in the iron are manganese from the ore and nickel from meteoritic iron.

In the non-alloyed steels the presence of non-metallic elements is essential for the metallurgical properties. The main elements here are carbon and nitrogen (Ron 1980), but sulphur, phosphorus and silicon also play some role. These elements may be dissolved in the metallic iron on interstitial sites or they may precipitate as chemical compounds such as Fe_3C, Fe_5C_2 and Fe_4N.

As already mentioned, in this context the cementite (Fe_3C) is of special interest. Fe_3C has an orthorombic structure and a magnetically split Mössbauer pattern. Ron (1980) gives a compilation of results of earlier Mössbauer investigations on this material. The magnetic hyperfine field is typically 20.7(2) T, the isomer shift 0.08(2) mm/s with respect to ^{57}Fe in a rhodium matrix and a quadrupole splitting of 0.02(2) mm/s. Ron (1971) describes the cementite spectrum as a sextet with an asymmetry in the

outer lines, due to an overlapping of two subspectra, which results from two different crystallographic sites for the iron. However it is not quite clear whether cementite precipitated in iron has equal features to pure cementite samples. With a magnetic field of 20.7 T precipitated cementite can be easily detected in the presence of α-iron (33.05 T), although some of the lines are hiding under the dominating α-iron pattern. It is therefore relatively easy to detect even small amounts of cementite precipitated in a ferrite matrix. A quantitative determination of the cementite content of a carbon steel requires that the f-factors of ferrite and cementite are known. For this study it was assumed, that the f-factor of the iron in cementite is the same as that for ferritic iron.

The Mössbauer pattern of martensite is a sum of different subspectra according the different numbers of carbon atoms on the interstices in the next neighbourhoods of the ^{57}Fe nuclei. The hyperfine parameter for this subspectra are given in Table 7.1 according Ino *et al.* (1968). Martensite was not observed for the samples investigated in frame of this work, but could have been distinguished easily from other phases because of its different pattern.

Tab. 7.1: Hyperfine field HF, isomer shift IS and quadrupol splitting QS for the subspectra of martensite according the distance of the ^{57}Fe nuclei from the interstitial carbon atoms. 1st nn Fe means those nuclei which are in the first nearest neighbour shell to a carbon atom. Data from Ino *et al.* (1968). The isomershift is given with respect to ^{57}Fe in a rhodium matrix.

Distance	HF [T]	IS [mm/s]	QS [mm/s]
1st nn Fe	26.5	−0.14	0.13
2nd nn Fe	34.2	−0.09	−0.02
3,4th nn Fe	33.4	−0.10	0.01

7.3 Description of the Samples

Several swords, sword fragments or other iron samples from different historical contexts were investigated by Mössbauer spectrocopy. In this section the origin and appearence of the samples are described. As a reference for typology Sachse (1994) was used throughout this chapter.

7.3.1 Bajuwarian Spatha

The fragment of a Bajuwarian spatha stems from the collection of the Landesamt für Denkmalpflege (Munich). The sword was found with others at an ancient burial site close to Aschheim north east of Munich and is dated from the archaeological context to the 6th Century AD, i.e., to the Merowingian period. A part of the fragment was cleaned by the author to get down to the bare metal and then etched for 10 minutes in concentrated sulphuric acid (Figure 7.3). The etching pattern indicated that the sword is built in a sandwich structure, with four bars on each side of a bridge, which is connecting the edges in the centre of the sword. The four bars on each side of the bridge are twisted pair-wise on a length of several centimetres (compare Sachse (1994, p.24)).

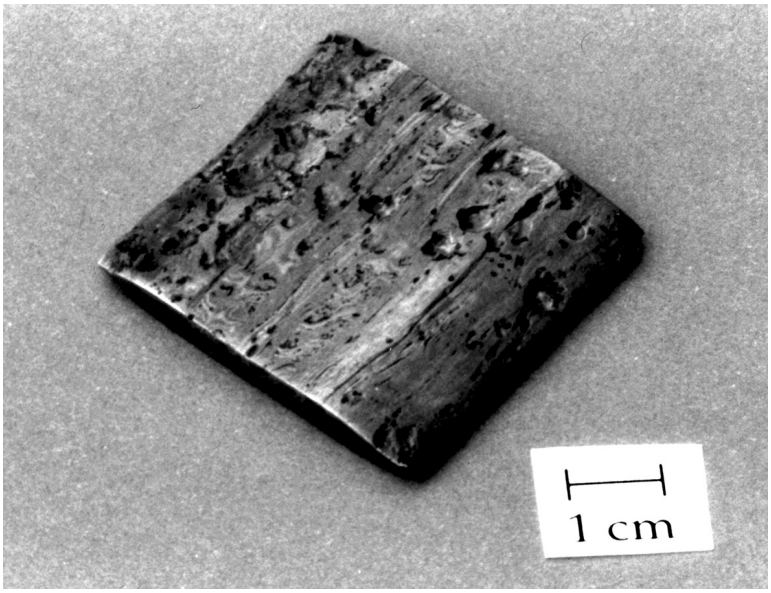

Fig. 7.3: Fragment of the Bajuwarian spatha.

7.3.2 Japanese Katana

The Japanese katana belongs to the collection of the Westfälisches Freilichtmuseum Hagen (Germany). It is dated to the 15th Century AD and is in excellent condition (Figure 7.4). On the polished blade no clear pattern is visible, since these blades are usually not etched. Most probably it is a *masame hada* blade with the lines of the pattern running along the sword. A parting line (*hamon*) can be seen between the hardened edge (*yakiba*) and the unhardened part (*jigane*) of the sword. There are no traces of oxidation on the sword. Japanese swords typically consist of over one million layers of pure carbon steel, with part of the starting material quenched in water. Repeated folding processes lead to the high number of layers (compare Sachse (1994, p.59)).

7.3.3 German Sabre

The German sabre (Westfälisches Freilichtmuseum Hagen, Germany) dates to the 17th Century AD and shows a rather coarse surface pattern with lines running along the blade (Figure 7.4). It was probably forged from one bar of Damascus steel, without twisting. The pattern was produced by filing the blade to its final shape and etching. Traces of oxidation can be seen in the form of little pits in the blade.

7.3.4 British Epée

The British epée (Westfälisches Freilichtmuseum Hagen, Germany) was manufactured by the Toledo company in the year 1790 AD. Like the German sabre it shows lines running along the blade and was therefore probably produced in the same way. However, the pattern on the thin blade is not as coarse as in the case of the sabre (Figure 7.4).

Fig. 7.4: Details of the Japanese katana, the German sabre, the Brithish epée and the Indian wootz bar.

7.3.5 Indian Wootz Bar

The Indian wootz bar (Westfälisches Freilichtmuseum Hagen, Germany) is probably an ingot, which means raw material for the production of a sword. The Indian wootz is often referred to as *cast* Damascus steel. In fact, the production of wootz is completely different from that of pattern welded steel objects. Wootz production is a special smelting process of the iron ore in a sealed crucible (reducing atmosphere) with the addition of charcoal and, for example, glass slag as a flux. The wootz cake resulting from this procedure shows a *watery* surface pattern, i.e. like the surface of a streaming river, with the details depending on the time and temperature of the smelting process (Sachse (1994, p.70ff)). The wootz bar examined here had a rather fine pattern, with the lines already breaking into needles (Figure 7.4).

7.3.6 Indonesian Kris

The Indonesian kris from a private collection is not dated. The sinuous blade (*serpa lumaku* for a moving snake) shows a strongly contrasting black and white pattern that matches the description of *pamor laring gangsir* (Sachse 1994, p.109 and 104) with only a small number of layers. The blade includes a miniature sculpture of an elephant at the guard (Figure 7.5). Traditionally meteoritic iron was used for the production of the kris, but the majority consist of steel and iron without any addition of nickel. The latter is called *false pamor*, but is still genuine Damascus steel. As in the case of the sabre and the epée the pattern suggests that the material was not twisted, but it was filed.

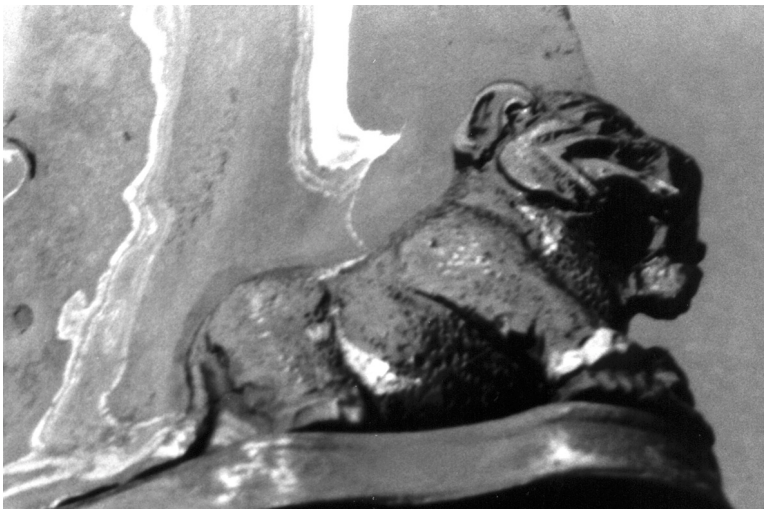

Fig. 7.5: Detail of the Indonesian Kris. The elephant is about 2 cm large.

7.4 Mössbauer Measurements

The Mössbauer measurements on the sword blades and on the samples were performed in a backscattering geometry (c.f. Chapter 5) at different spots with a typical size of about $1\,\mathrm{cm}^2$. No significant differences between the different spots on the same blade were observed, however.

7.4.1 Japanese Katana, German Sabre, British Epée, Indian Wootz Bar

The spectra of the Japanese katana, the German sabre, the British epée and the Indian wootz bar are shown in Figure 7.6. They can be described as a sum of two components, one of which can be attributed to α-iron, the other to cementite.

Since the contribution in some cases of the cementite phase is very small, the fitting procedure was as follows: First the Indian wootz bar was fitted with free values for the hyperfine parameters (isomer shift IS, quadrupole splitting QS and magnetic hyperfine field HF) for the two phases, α-iron and cementite. As already mentioned in section 5.7 it was necessary to alter the intensity ratio of the sextet lines due to different saturation depths of the γ-ray for the different lines in the spectra. This leads to deviations from the 3:2:1:1:2:3 intensity ratio of the α-Fe lines. Moreover, the small amounts of cementite may be overestimated especially in the lines 2 and 5 (c.f. Figure 7.6 for the numbering of the lines), which do not overlap with the lines of α-iron. For the other lines, which partially overlap with those of α-Fe, an asymmetry of the line intensities was allowed, in the sense that the intensity of line 1 was not necessarily equal to the intensity of line 6. For the outer, the middle and the inner lines independent gaussian broadenings were assumed for all sextets.

In this way the fitting parameters of cementite embedded in α-iron result as $IS = 0.08\,\mathrm{mm/s}$, $QS = 0.02\,\mathrm{mm/s}$ and $HF = 20.4\,\mathrm{T}$. If not explicitly provided, the errors

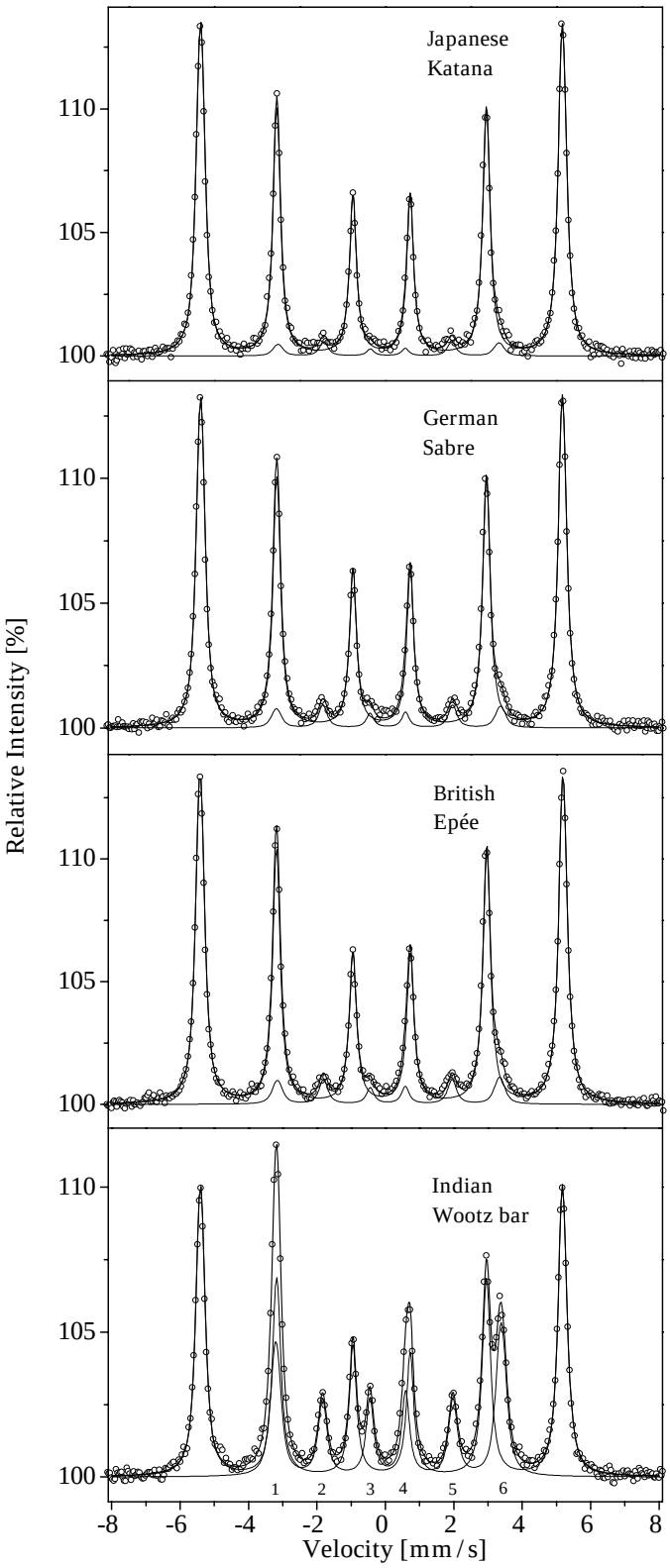

Fig. 7.6: Mössbauer spectra of the Japanes katana, the German sabre, the British epée and the Indian wootz bar. The numbers 1 to 6 at the bottom of the figure are those used in the text for indicating the individual lines for cementite.

of the results given in this section are 1 in the last digit. For the asymmetry in the intensity of lines 1 and 6 or 3 and 4, respectively, the intensity ratios were found to be Area(6)/Area(1)=1.14(2) or Area(4)/Area(3)=1.09(6). The gaussian broadenings for the outer, middle and inner lines of the cementite were 0.08 mm/s, 0.05 mm/s and 0.02 mm/s, respectively. This means that the lines are not much broadened over the lorentzian width of $LW = 0.26$ mm/s fitted for all lines in the spectrum.

For all the other spectra these parameters, except the hyperfine field HF, were kept fixed, in order to obtain accurate values for the partial intensity of cementite in the spectra. The results are compiled in Table 7.2.

Tab. 7.2: Fit results for the Japanese katana, the German sabre, the British epée and the Indian wootz bar. In the last column the values of 99.998 % pure α-iron are given. The errors are ± 1 in the last digit. TA: total area, LW: lorentzian line width for all lines in the spectrum, HF: magnetic hyperfine field, IS: isomer shift, A_I: relative intensity of the inner lines in this sextet, A_M: relative intensity of the middle lines, A_O: relative intensity of the outer lines, σ_O: gaussian broadening of the outer lines of α-Fe, RA: (relative) area contribution of the Fe_3C-component to the whole spectrum.

			Japanese Katana	German Sabre	British Epée	Indian Wootz bar	α-iron 99.998 %
TA			0.083	0.086	0.090	0.093	0.082
LW		[mm/s]	0.24	0.25	0.26	0.26	0.24
α-Fe	HF	[T]	32.9	32.9	33.0	32.9	33.0
	IS	[mm/s]	-0.11	-0.11	-0.11	-0.11	-0.11
	A_I	[%]	19	19	19	19	19
	A_M	[%]	32	33	33	32	34
	A_O	[%]	49	48	48	48	47
	σ_0	[mm/s]	0.06	0.06	0.05	0.06	0.06
Fe_3C	HF	[T]	20.0	20.3	20.1	20.4	–
	A_I	[%]	19	23	22	23	–
	A_M	[%]	39	37	34	23	–
	A_O	[%]	42	40	44	54	–
	RA	[%]	5	8	9	35	–

From Table 7.2 one sees that the Mössbauer parameters of the dominant ferritic component are, within the error equal, for this swords and the wootz bar. Moreover they are identical to the values for 99.998 % pure α-iron (Spectrum c.f. Figure 5.13). The lorentzian line width LW and gaussian broadening σ_O are especially close, which means that the α-iron component in the swords may only contain minor traces of alloying elements. The purity of this material, as far as one can see from the Mössbauer measurements, is remarkable. Again it may be mentioned here that no martensite was found in this samples.

The cementite component shows small changes in the magnetic hyperfine field HF, which are in the range of the hyperfine field discussed in the literature (Ron 1980). As already mentioned, the hyperfine parameters of cementite may vary with the form of precipitation in the α-iron matrix. Depending on the carbon concentration in the steel the cementite precipitates in different shapes (Koch 1983). For low concentrations it may form as ball-shaped cementite especially at grain boundaries of the α-iron. At the eutectic point of pearlite (3.62 % C) it typically forms lamellae. At concentrations higher than that of the eutectic point, so called secondary cementite forms in grains, displacing the α-iron. These different forms of cementite may indeed lead to variations in the hyperfine parameters, depending on the actual surface and interface effects of the cementite particles.

Table 7.2 also shows the partial relative area RA of the cementite in the spectrum, which increases from 5% for the katana to 35% for the wootz bar. At the same time the contribution of the middle lines (2 and 5) A_M to the sextet of the cementite decreases. As shown in section 2.4.2, an increased intensity of the middle lines describes a possible orientation (texture) of the magnetic field in the sample to the direction of the resonant γ-ray. Since there is no increased intensity of the middle lines observed for the α-iron subspectra, the orientation of the magnetic field of the cementite component could be due to a orientation of the cementite lamellae, where the hyperfine field direction is lying in the plane of the lamellae. Still it is not understood, why there should be such a orientation, especially because the surface of the samples has an angle of about 45^o to the direction of the resonant γ-rays from the source in this particular geometry (c.f. Figure 5.1).

However, saturation effects also influence the relative areas of outer, middle and inner lines of the cementite, as well as its total contribution to the spectrum. As shown in Section 5.7, due to saturation effects, the intensity ratio within a sextet is altered. The same argument holds for a second component in small concentrations, in the present case cementite. For the lines which are not overlapping with the lines of the α-iron, the probing depth is larger than for the α-iron itself. For overlapping lines (here especially line 1, but also lines 4 and 6 c.f. Figure 7.3) the probing depth is smaller than for α-iron itself, because the ^{57}Fe nuclei in the cementite compete with the ^{57}Fe nuclei in α-iron for resonant absorption.

A simulation according Sections 5.5 and 5.7 was therefore performed generating spectra for given amounts of cementite in α-iron. These simulated spectra were than fitted with the same procedure as described above. Figure 7.7 shows the amount of Fe bound in cementite as a function of the fitted relative area. For concentrations of cementite between two simulated values a linear interpolation can be used. For the different ranges of relative areas (RA) of the cementite in the Mössbauer spectra Table 7.3 gives the linear approximations for the calculation of the real amount x_{Fe} of Fe bound in cementite. The carbon content in at% can then be calculated as

$$\text{Carbon content} = 100 \cdot \frac{x_{\mathrm{Fe}}/3}{100 + x_{\mathrm{Fe}}/3} \qquad [at\%]. \tag{7.1}$$

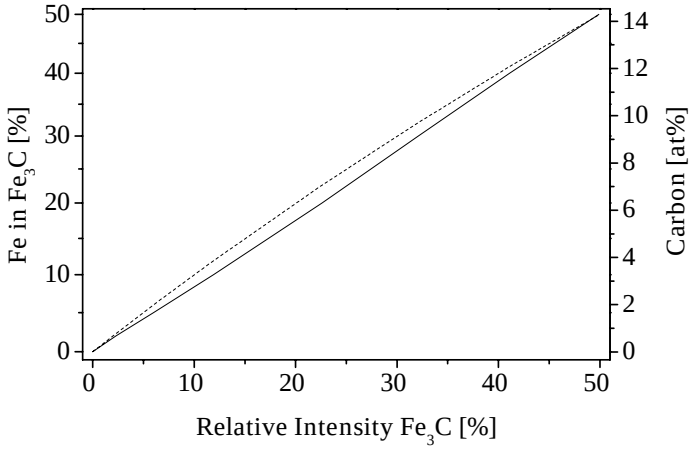

Fig. 7.7: Amount of Fe which is bound in cementite as a function of fitted relative area in simulated spectra. The calculated values are linearly interpolated. The dashed line indicates the situation without saturation effects. On the right side the corresponding carbon concentration in at% is shown.

Tab. 7.3: Linear approximations of the fractional amount of iron x_{Fe} bound in cementite as a function of the relative area RA of cementite in the Mössbauer spectra.

RA [%]	x_{Fe} [%]
$2.3 \leq RA < 6.0$	$0.135 + 0.811 \cdot RA$
$6.0 \leq RA < 11.9$	$-0.085 + 0.847 \cdot RA$
$11.9 \leq RA < 22.6$	$-1.121 + 0.934 \cdot RA$
$22.6 \leq RA < 32.1$	$-3.789 + 1.053 \cdot RA$
$32.1 \leq RA < 41.1$	$-5.667 + 1.111 \cdot RA$
$41.1 \leq RA < 49.9$	$-6.705 + 1.136 \cdot RA$

From Table 7.3 the carbon concentration of the swords can be derived. The results are given in Table 7.4. The Japanese katana, the German sabre and the British epée are clearly under-eutectic steel, which would have a carbon concentration of 3.61 at%, while the wootz plate is in the region of cast steel, which spans carbon contents beyond 8.91 at%.

Tab. 7.4: Carbon concentrations in the swords, derived from the measured Mössbauer spectra by use of the simulation described in the text.

Sword	RA [%]	x_{Fe} [%]	C [at%]
Katana	5(1)	4(1)	1.3(3)
Sabre	8(1)	7(1)	2.3(3)
Epée	9(1)	8(1)	2.6(3)
Wootz plate	35(1)	33(1)	9.9(3)

It should be mentioned that these investigations do not give any information about carbon in the form of graphite inclusions in the steel or small amounts of carbon dissolved in the α-iron at interstitial sites, as long as its concentration is too low for the formation of martensite. However, no indications of the presence of martensite was observed in any of the samples either.

7.4.2 Indonesian Kris

The Mössbauer pattern of the Indonesian kris is shown in Figure 7.8 (top). Besides α-iron with a magnetic field of 32.9 T and a gaussian broadening of 0.06 mm/s in the outer lines, the spectrum shows at best a very small amount of cementite (magnetic field 20.3(2) mm/s, relative area less than 2 %). There is, however, a clearly visible doublet component at small positive velocities.

Sachse (1994, p.114) describes a method of black burning with a special arsenic solution, used by Indonesian smiths. Another method would be to cover the piece with linseed oil and burn over the fire at low temperature.

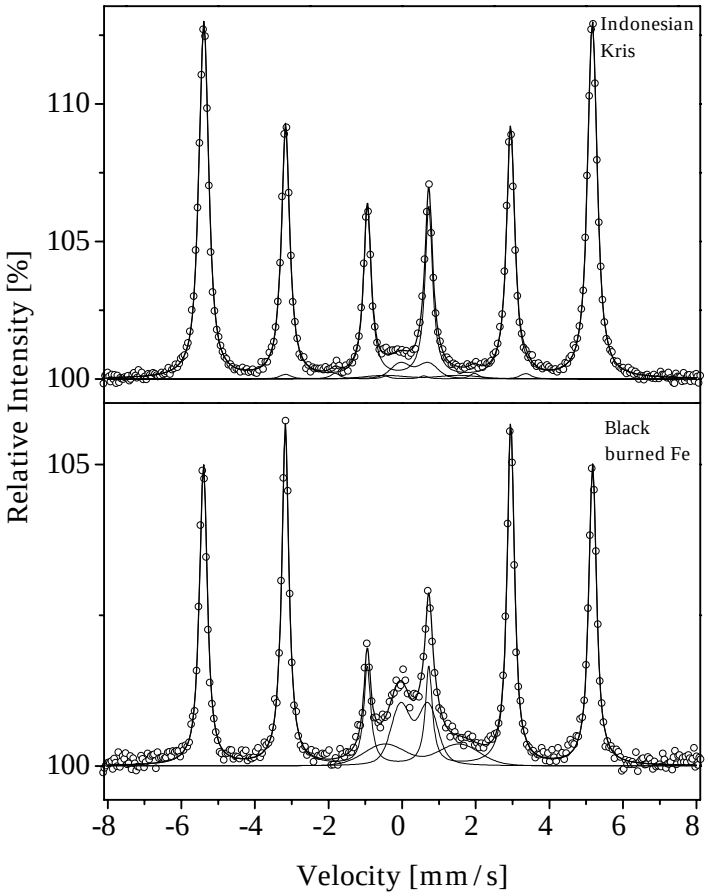

Fig. 7.8: Mössbauer spectra of the Indonesian kris and black burned iron.

To emulate the doublet component in the spectrum of the kris in a laboratory experiment, a foil of α-iron was covered with linseed oil and heated for three minutes at

500 °C. The resulting black covering was scraped off of the metal surface. The CEMS spectrum of this sample is shown in figure 7.8 (bottom). The doublet structure already seen on the kris shows up clearly, especially because the CEMS method is more surface sensitive than Mössbauer spectroscopy in the backscattering mode. Two doublets could be identified, one with an isomer shift of 0.33(2) mm/s and a quadrupole splitting of 0.74(2) mm/s and the other, less well-defined one with an isomer shift of 0.54(6) mm/s and a quadrupole splitting of 2.1(2) mm/s, respectively. The Mössbauer parameters of the first of these doublets are typical for trivalent iron, while the isomer shift of the second one is intermediate between trivalent and divalent iron. Possibly these doublets arise from superparamagnetic magnetite, which is indeed black and might have formed of the surface of the iron.

The doublet components observed in the model material can be used to fit the spectrum of the Indonesian kris in a satisfactory manner, as can be seen in Figure 7.8. It is not clear at this point, whether a compound like magnetite would survive further forging processes and how the pattern on the sword could be influenced by such a kind of black burning.

It should be noted that no signs of the presence of nickel in the iron of the kris were found, but instead the classical signs of Damascus steel. For nickel concentrations up to 25 at% in a Fe-Ni alloy one would expect a increased hyperfine field of up to 34 T. Therefore, this kris can be classified as *false parmor*. The included miniature sculpture of an elephant at the guard was found by Mössbauer spectroscopy to be of the same material like the rest of the blade. Therefore it was probably sculptured from an outstanding part at the guard after the forging of the blade.

7.4.3 Bajuwarian Spatha

Since the Bajuwarian spatha was already broken, destructive methods could be applied, like cleaning (brushing to the bare metal), etching etc. The pattern of the sword was already described in Section 7.4.1. It was made visible by etching a piece of the cleaned sword for 10 minutes in sulphuric acid.

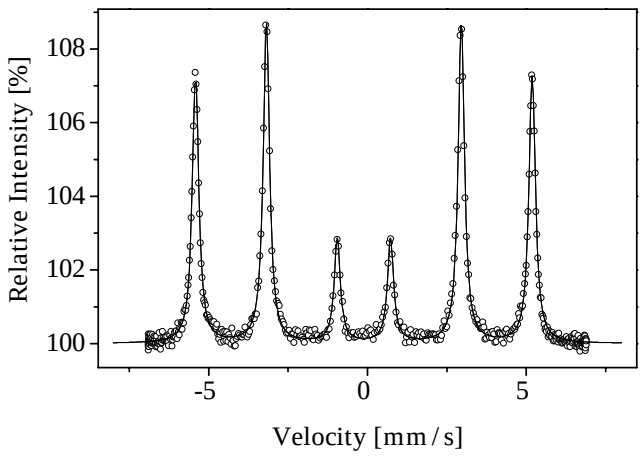

Fig. 7.9: Conversion electron Mössbauer spectrum of the fragment of the Bajuwarian spatha.

Despite the patterned surface, which would indicate two phases, the CEMS spectrum of this piece (Figure 7.9) shows only α-iron with a magnetic field of 33.0 T and a gaussian broadening in the outer line of 0.02 mm/s. The broadening is about three times smaller than the usual broadenings obtained in backscattering, which is mainly due to the absence of saturation effects in the CEMS method. However it still indicates that this is very pure iron that is practically free of carbon.

In electron micrographs one could clearly see ferritic areas with grain boundaries only and areas with very small inclusions of less than a micrometer linear size. Electron microprobe analysis showed the inclusions to contain reasonable amounts of phosphorus, probably in the form of Fe_4P. The amount of these phosphorus containing inclusions is, however, by far too small to be detected in the Mössbauer spectrum. In the electron microscope the inclusions made up about 1/25 of the area of those regions, which showed such inclusions at all. Micro-hardness was measured at about 118(9) for large ferrite grains, 150(6) for ferrite with grain boundaries and 152(8) for ferrite with inclusions containing phosphorus. The overall hardness of the sword would therefore mainly be determined by the size of the ferrite grains, which is also influenced by the presence of the inclusions. The visibility of the pattern on the surface corresponds to different etching behaviour of the inclusion-free and inclusion-containing areas. Probably steels with different phosphorous concentrations were welded together to obtain the pattern.

At the end of this section a correlation should be mentioned: Figure 7.10 shows the content of carbon bound in cementite for the Bajuwarian spatha, the Japanese katana, the German sabre and the British epée as a function of their age. It can be clearly seen that the cementite content decreases with the increasing age of the objects. Assuming a equal carbon concentration at the time of the making of this swords the halflife of cementite can be determined as $t_{1/2} = 480(120)$ a. The common starting concentration for the carbon bound in cementite would be 4.3(7) at%, which would include pearlitic steel. The quality of such a fit is very pure, but it shows the metastability of the cementite. Principially the determination of the overall carbon content in ancient samples in combination with the determination of the amount of carbon, which is still bound in cementite would allow a dating of the ancient objects. However, a database of the carbon concentrations of many objects of known age would be necessary for such a dating method. Also the chemical analysis of the overall carbon content would require to take a sample of the objects and therefore would be destructive.

7.5 Modern Damascus Steel

It is remarkable how pure the iron of the described ancient steel objects is and so it was of interest also to examine modern Damascus steel.

Figure 7.11 shows the Mössbauer spectra of a Damascus steel plate welded at the Freilichtmuseum Hagen (Germany). The starting materials were *ferritic* and *pearlitic* steel suitable for forging.

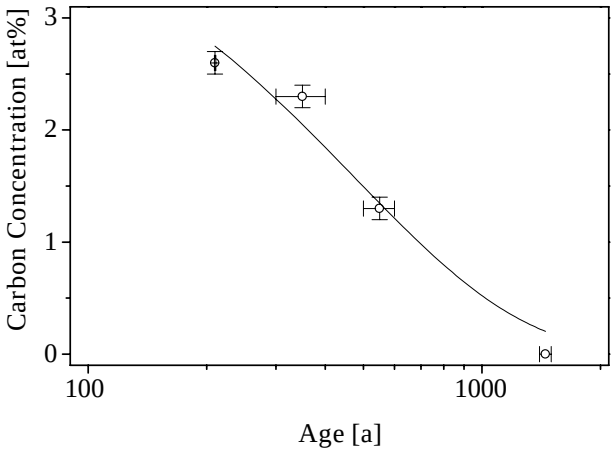

Fig. 7.10: Concentration of carbon which is bound in cementite, as a function of the age of some of the described swords.

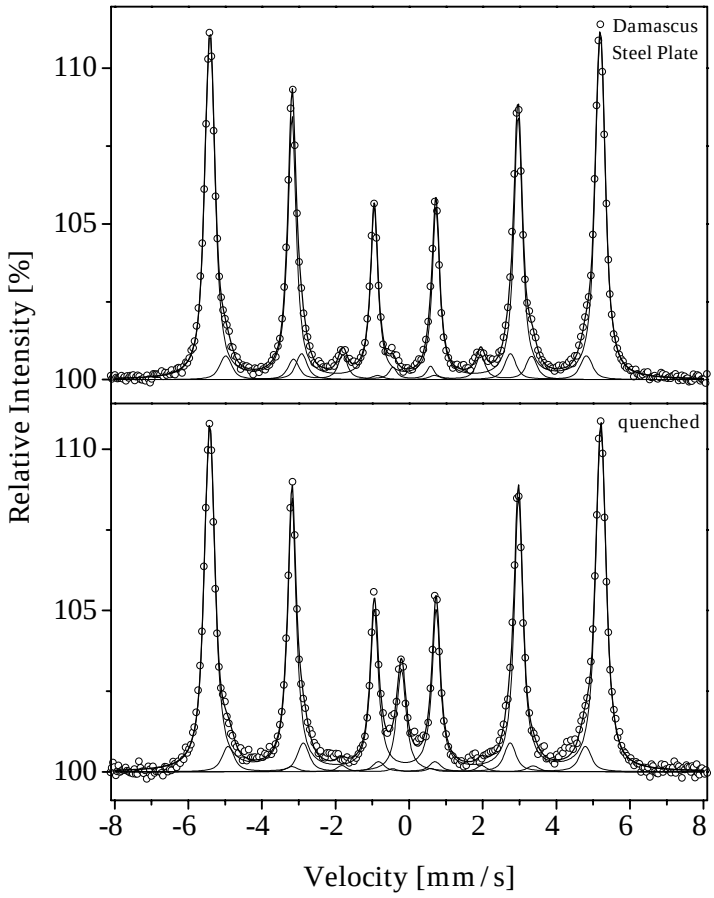

Fig. 7.11: Mössbauer spectra of a modern Damascus steel plate after welding (top) and after heating to 550 °C and quenching (bottom).

In the Mössbauer pattern of the welded plate cementite is present with a relative area of 7 %. Moreover, there is a visible asymmetry of the α-iron sextet towards smaller

magnetic fields. This asymmetry can be fitted with an additional sextet with a hyperfine field of 30.4(1) T. It can be explained by the presence of small amounts of alloying elements, which typically reduce the magnetic hyperfine field in the α-iron of those iron atoms in the α-Fe which have substitutional impurities in their vicinity. These traces of alloying elements also explain the presence of the austenitic component, in the spectrum taken after quenching the plate from about 550 °C to ambient temperature by immerging it into water. This austenite is visible as single line in the centre of the bottom spectrum in Figure 7.11. The alloying elements lower the temperature of the austenite-martensite phase transition in such a way that tempering to 550 °C and subsequent quenching leads to a partially austenitic steel. The cementite subspectrum has nearly vanished in the Mössbauer pattern of the quenched plate. Most of the carbon is probably dissolved in the austenitic phase.

This shows in an impressive way, what problems confront a present day smith who is trying to keep up old handcraft traditions. Although the starting material was classified as pure carbon steel, it contained traces of alloying elements other than carbon because of scrap recycling in modern steel making. This is the reason why practically all modern steels contain traces of various elements. However there is also an advantage of the presence of alloying elements in modern steel: The absence of alloying elements can be used as a test of old iron and steel implements for their origin, since it is very difficult to fake such ancient steel objects nowadays with really pure carbon steel.

7.6 Summary and Conclusions

Mössbauer spectroscopy in backscattering geometry is able to non-destructively yield information of the cementite precipitation in ancient Damascus steel swords and objects.

The cementite precipitated in the α-iron surrounding shows quite well the typical hyperfine parameters found in the literature. From the spectra, the cementite content can be derived by the use of simulated content/relative area relations given in Table 7.3. For the examined swords the carbon content in the cementite phase was between 1.3 at% and 2.3 at% and thus, on the average, in the subeutectoid region. For the Indian wootz bar it was 9.9(3) at%. In the case of the Indonesian kris an additional component was found; it was probably caused by black burning of the sword. The kris turned out to belong to the group of *false pamors*. Only the Bajuwarian spatha does not contain any carbon bound in cementite, but gets its design by phosphorisation, which was detected by the electron microprobe. The amount of phosphorus is too small to be observed, for example as Fe_4P, in the Mössbauer pattern. No martensite was found in any of the samples, which shows either that the martensite is not stable in the course of time or that in no case the product was quenched rapidly after the last heating.

The α-iron component in the objects turned out to be of a quality comparable to 99.998 % pure α-iron. Due to scrap recycling in today's steel production it is difficult to obtain iron of such high purity from the iron industry and at an acceptable price. At the time of writing the price of 99.99 % pure α-iron was about 360 USD for 10 g.

This makes it even more impressive that ancient steel production and smiths were able to produce this swords with such high purity and manufacturing skills. In Celtic times the use of phosphorus was quite common for hardening iron objects (private communication Dozent Preßlinger, Voest Alpine, Austria and Brian Gilmour, University of Oxford, Great Britain). This seems to have survived also the Roman occupation north of the Alps until the time of the Bajuwarian tribes. The phosphorized steel was suitable for the production of Damascus steel as well as carburized steel. Carburisation in different ways was obviously the usual method for hardening steel during the last millennium, where very different cultural contexts led to rather similar results. There seemed to be a general agreement among the ancient smiths, what a good steel suitable for forging had to be like. Starting from the iron age the production of Damascus steel was probably first of all a method to combine starting materials of different properties in order to obtain a good weapon. Only later, pattern welding was perfected in most cultures (though not in Japan) perhaps also to demonstrate the rank of the sword's owner. Damascus steel is a modern composite material from the iron age.

8 Outlook

This work describes the use of non-destructive Mössbauer spectroscopy on archaeological metal objects. The potentials of this method have been demonstrated in two applications on Celtic gold coins and on Damascus steel swords.

In the case of the Celtic gold coins it is interesting to see how Mössbauer spectroscopy together with other techniques yields a rather complete picture. To fully understand how the Celts did surface leaching for gold enrichment, it would be necessary to further investigate the air inclusions in the coins. One possibility would be radiography with myons, which would at the same time yield information about the composition of the bulk by myonic X-ray fluorescence. The influence of the soil on such gold-silver-copper alloys could also be studied by means of trace element analysis (through, for example, neutron activation analysis) of the soil around the sites where hoards were found. Unfortunately hoards are rarely found by archaeologists, so the context of the find is usually not documented.

The experiments on Damascus steel objects demonstrate that Mössbauer spectroscopy is able to yield conclusive information about the material. Thus, for example, the Indonesian kris could be classified as *false parmor*. The samples were chosen to cover a wide range of Damascus steel production across different cultures. In further work it could be of interest to study the variations across a culture or through time. An even wider field would be the investigation of, for example, phosphorized steel and nickel-iron alloys in sword production. Also the metastability of cementite in the iron-cementite system could be investigated by Mössbauer measurements of steel objects of known age and a simultaneous determination of the overall carbon content, including the carbon bound in graphite that may have formed from cementite.

Tin as a Mössbauer isotope was considered in the chapters about CEMS and the backscattering mode, but tin objects were not included in the study. The investigation of tin bronzes would be an obvious application. Since, however, the hyperfine parameters of the various possible bronze phases are not known, this would require some basic research on these materials before studies of archaeological objects can be undertaken.

In short, this study demonstrates how non-destructive Mössbauer spectroscopy in archaeometallurgy strengthens the bridge between science and anthropology.

Literature

Berger M.J. in Alder B., Fernbach S., Rotenberrg M. (Edit.) 1963: *Methods in Computational Physics,* **1**, 135-215, New York

Bernier R. 1951: *Ann.chim.,* **6**, 104–161

Bethe H.A. 1930: *Ann. Physik,* **V 5**, 325–400

Bonchev Z.W., Jordanov A., Minkova A. 1969: Nucl.Intrum.Methods, **70**, 36–40

Bronstein I.N., Semendjajew K.A. 1989: *Taschenbuch der Mathematik,* Frankfurt

Cohen R.L. 1978 in: Shenoy G.K. and Wagner F.E. (Edit.): *Mössbauer Isomershifts,* 541–, Amsterdam

Colbert H.M. 1974: *Sandia Laboratories SLL-74-0012*, Livermore

Crecelius G. 1973: *Z. Physik,* **258**, 56–63

Davisson C.M. 1955 in: Siegbahn K. (Edit.): *Beta- and Gamma-ray Spectroscopy,* **2**, 24, Amsterdam

Epstein S. 1936: *The Alloys of Iron and Carbon,* **1**, Amsterdam

Evans R.D. 1955: *The Atomic Nucleus* in *International Series in pure and applied physics* , New York

Evans R.D. in Flügge S. 1958: *Handbuch der Physik,* **34**, 218–298, Berlin

Forrer R. 1908: *Keltische Numismatik der Rhein und Donaulande* **I**, Straßburg (ND Graz 1968). **II** *Bibliographische Nachträge und Ergänzungen,* edit. by Allen D.F., Castelin K., Colbert de Beaulieu, G.K. Jenkins, Kellner H.J., Winkler J. 1969, Graz

Fukumura K., Katano R., Kobayashi T., Nakanishi A., Isozumi Y. 1991: *Nucl. Instrum. and Meth.* **A301**, 482–484

Fukumura K., Kobayashi T., Nakanishi A., Katano R., Isozumi Y. 1991: *Hyperfine Interactions,* **69**, 755–758

Fukumura K., Makita T., Kobayashi T., Isozumi Y. 1991: *Nucl. Instrum. and Meth.* **A301**, 485–488

Fukumura K., Nakanishi A., Kobayashi T., Katano R., Isozumi Y. 1991: *Nucl. Instrum. and Meth.* **B61**, 127–131

Gebhard R., Wagner U., Raub C., Lehrberger G. in Lehrberger G., Fridrich J., Gebhard R., Hrala J. (eds.) 1997: *Das prähistorische Gold in Bayern, Böhmen und Mähren,* 99–116, Prague

Goganov D.A., Lebedev A.G., Serebryakov A.S. 1983: *Appara. and Meth. of X-Ray Analysis,* **29**, 35–43, Leningrad

Graham R.L., Knuth B.E., Patashnik O. 1990: *Concrete Mathematics*, Reading Massachusetts

Große G. 1992: *Mos-90, Version 2.2, Manual and Program Documentation,* München

Gütlich P., Link R., Trautwein A. 1978: *Mössbauer Spektroskopy and Transition Metal Chemistry,* Berlin

Hansen M. 1985: *Constitution of Binary Alloys* , New York, C-Fe 353–365, Ag-Au 5–7, Au-Cu 198-203

Hellwege K.H. (Edit.) 1961: *Landolt-Börnstein, Gruppe 1: Kernphysik und Kerntechnik,* **1**, Berlin

Herskowitz N., Walker J.C. 1967: *Nucl.Intrum.Methods,* **53** , 273

Höper H.J. 1987: *Damaszenerstahl,* Münster

Hultgren R., Tarnopol L. 1939: *Trans.AIME,* **133**, 228-238

Huray P.G., Roberts L.D., Thomson J.O. 1971: *Physical Review B* **4**, 7, 2147–2161

Isozumi Y. and Takafuchi M. 1975: *Bull.Inst.Chem.Res.,***53** , 147

Isozumi Y., Kishimoto S., Katano R., Tekekoshi 1987: *Rev. Sci. Instrum.* **58(2)**, 293

Isozumi Y., Ito S., Fujii T., Katano R. 1989: *Rev. Sci. Intrum.* **60(10)**, 3262

Jack K.H. 1948: *Proc.Roy.Soc. (London),* **A195**, 56-61

Jackson J.D. 1974: *Classical Elektrodynamics,*Berkley

Jenkins R., De Vries J.L. 1970: *Practical X-ray spectroscopy,* London

Johnson G.G., White W.E.: *ASTM Data Series* **DS 46**

Katano R., Fuji T., Kobayashi T., Fukumura K., Isozumi Y. 1989: *Nucl. Instrum. and Meth.* **A280**, 285–287

Kellner H.J. 1990: *Die Münzfunde von Manching und die keltischen Fundmünzen aus Südbayern. Die Ausgrabungen in Manching,* **12**, Stuttgart

Kishimoto S., Isozumi Y., Katano R., Takekoshi H. 1987: *Nucl. Instrum. and Meth.* **A262**, 413–418

Kishimoto S., Isozumi Y. 1990: *Nucl. Instrum. and Meth.* **A286**, 262–264

Kobayashi T., Fukumura K., Nakanishi A., Katano R., Isozumi Y. 1992: *Bulletin of Inst. for Chem. Research,* **70.4**, 408–417

Kobayashi T., Fukumura K., Nakanishi A. 1993: *Nucl. Instrum. and Meth.* **B76**, 204–206

Koch F., Pyzalla G. 1983: *Werkstoffe,* Köln-Porz

Kogachi M., Nakahigashi K. 1985: *Jpn.J.Appl.Phys.,* **24** (2),121-125

Kopitzki K. 1993: *Einführung in die Festkörperphysik,* Stuttgart

Kuhn M., Bzowski A., Sham T.K. 1994: *Hyperfine Interactions* **94**, 2267–2272

Kurdjumov G, Kaminski E. 1928: *Nature,* **122**, 475–476

Lang G. 1963: *Nucl. Instrum. and Meth.* **48**, 425–428

Lehrberger G., Raub Ch.J. in Morteani G., Northover J.P. (eds.) 1995: *Prehistoric Gold in Europe,* 341–355, Dordrecht

Lehrberger G. in Lehrberger G., Fridrich J., Gebhard R., Hrala J. (eds.) 1997: *Das prähistorische Gold in Bayern, Böhmen und Mähren,* 137–140, Prague

Levy L., Mitrani L., Ormanjiev S. 1964: *Nucl.Intrum.Methods,* **31**, 233

Major J.K. 1962: *Nucl.Phys.* **33**, 323

Mayer-Kuckuk T. 1992: *Kernphysik,* Stuttgart

Martinek K.P. 1997 in Lehrberger G., Fridrich J., Gebhard R., Hrala J. (eds.) 1997: *Das prähistorische Gold in Bayern, Böhmen und Mähren,* 136, Prague

Morteani G. (Edit.) 1993: *Das prähistorische und keltische Gold im bayerisch-böhmischen Raum: Metallurgie und Herkunft,* 1. Zwischenbericht, München

Morteani G., Martinek K.P. 1997 in Lehrberger G., Fridrich J., Gebhard R., Hrala J. (eds.) 1997: *Das prähistorische Gold in Bayern, Böhmen und Mähren,* 127–135, Prague

Mößbauer R. 1959: *Z. Naturforschung* **14a**, 211–16

Neuert H. 1984: *Atomare Stoßprozesse,* Stuttgart

Overbeck B. 1980: *Die Kelten in Mitteleuropa*, 101–10, Salzburg

Paulsen R. 1933: *Die Münzprägung der Boier,* Wien-Leipzig

Pearson W.B. 1967: *A Handbook of Lattice Spacings and Structures of Metals and Alloys* **2** , Pergamon Press, 80–81 and 151

Petch N.J. 1942: *J. Iron Steel Inst.,* **145**, 111-123

Petch N.J. 1943: *J. Iron Steel Inst.,* **147**, 221-227

Plinius C.S. d. Ältere 1984: *Naturalis Historiae,* **XXXIII**, Artemis-Verlag, München

Polenz H. 1982: *Münzen in latènezeitlichen Gräbern Mitteleuropas aus der Zeit zwischen 300 und 50 v.Chr., BVbl.* **47**, 27–222

Press W.H., Flannery B.P., Teukolsky S.A., Vetterling W.T. 1988: *Numerical Recipes in C,* Cambridge

Prince A., Raynor G.V., Evans D.S. 1990: *Phase Diagrams of Ternary Gold Alloys,* London

Prosser H., Wagner F.E., Wortmann G., Kalvius G.M., Wäppling R. 1975: *Hyperfine Interactions* **1**, 25–32

Rauscher G. 1995: *Metall,* **50** (3), 174–178

Regen M. 1994: *Diplomarbeit,* TU-München

Riley M.E., MacCallum C.J., Biggs F. 1975: Atom. Data and Nucl. Data Tables, **15**, 443–476

Ron M. 1980 in: Cohen R.L. (Edit.): *Applications of Mössbauer Spectroscopy,* **2**, 329–388, London

Ron M., Mathalone Z. 1971: *Physical Review B,* **4** , 774

Rose M.E. 1955 in: Siegbahn K. (Edit.): *Beta- and Gamma-ray Spectroscopy,* **2** , 396, Amsterdam

Rutherford E. 1911: *Philos. Mag.,* **21**, 669–668

Sachse M. 1994: *Damascus Steel,*Düsseldorf

Sawicki J.A., Sawicka B.D., Stanek J. 1976: *Nucl.Instrum.Methods,* **138**, 565

Sawicki J.A., Tyliszczak T., Gzowski O. 1981: *Nucl.Instrum.Methods,* **190**, 433–435

Sawicki J.A., Tyliszcak T., Stanek J., Sawicka B.D., Kowalski J. 1983: *Nucl. Instrum. Methods Phys.Res.,* **215** (3), 567–568

Schatz G., Weidinger A. 1985: *Nukleare Festkörperphysik*, Stuttgart

Schwabl F. 1993: *Quantenmechanik*, Berlin

Seljakov N., Kurdjumov G., Goodtzov N. 1927: *Z.Physik,* **45**, 384–408

Shenoy G.K., Dunlop B.D. 1978 in: Shenoy G.K. and Wagner F.E. (Edit.): *Mössbauer Isomershifts*, 869–876, Amsterdam

Shenoy G.K., Friedt J.M., Maletta H., Ruby S.L. 1974: *Mössbauer Effect Methodology*, **9**, 277–305

Sternheimer R.M. 1966: *Physic. Rev.,* **145**, 247–250

Stevens J.G., Stevens V.E. 1978: *Mössbauer Effect Data Index 1976*, New York

Stöcker H. 1993: *Taschenbuch der Physik,* Frankfurt

Storm E., Israel H.I. 1970: *Nuclear Data Table A,* **7**, 566–681

Subramanian P.R., Perepezko J.H. 1993: *J.Ph.Equil.* **14** (1), 62-75

Swanson K.R., Spijkerman J.J. 1970: *J.Appl.Phys.,* **41**, 3155

Thomson J.O., Obenshain F.E., Huray P.G. 1974: *Physical Review B* **11,5**, 1835–1839

Thümmel H.W. 1974: *Durchgang von Elektronen- und Betastrahlung durch Materieschichten,* Berlin

Tylecot R.F. 1992: *A History of Metallurgy,* London

Vegard L. 1928: *Z.Cryst.,* **67** , 239

Wagner F.E., Friedl J., Füssel A., Gebhardt A.R., Kyek A., Lehrberger G., Kobayashi T., M. Regen 1996: *Conference Proceedings Vol. 50, ICAME-95,* 773–76, Bologna

Wagner U., Wagner F.E., Häusler W., Shimada I. 2000: *The Use of Mössbauer Spectroscopy in Studies of Achaeological Ceramics,* to be published

Wegener H. 1966: *Der Mössbauer-Effekt und seine Anwendungen in Physik und Chemie,* Mannheim

Wentzel G. 1927: *Z.Physik,* **40**, 590–593

Wever F. 1924: *Z.Elektrochem,* **30**, 376–382

Wordel R. 1988: *Dissertation,* TU-München

Yasuda K. 1987: *Gold Bulletin* **20** (4), 90–103

Ziegaus B. 1993: in *Das keltische Jahrtausend*, 220–27, Mainz

Ziegaus B. 1993b: *Der Münzfund von Sontheim, Kat.Prähist.Staatsslg.* **24**, München

Ziegaus B. 1995: *Der Münzfund von Großbissendorf, Kat.Prähist.Staatsslg.* **27**, Kallmünz

Acknowledgements

Many thanks to

- Prof. Dr. F.E. Wagner for the friendly admission in his group and the helpfull discussions during the last months.
- Dr. Ziegaus from the Prähistorische Staatssammlung München for leaving the Celtic gold coins.
- Dr. Dauskardt from the Westfälische Freilichtmuseum Hagen for leaving some of the Damascus steel swords and objects.
- Dr. van Bürck for leaving the Indonesian kris from his private collection.
- Dr. U. Wagner for her help in the radiochemistry laboratory.
- Prof. Pankhurst from the University College London for providing access to an electron microscope.
- Prof. Calogero from the University Venice for providing access to a X-ray diffractometer.
- Dr. Reisner from the Lehrstuhl A für Mechanik, TU-München, for some helpfull experiments on an electron microscope and a X-ray diffractometer.
- my colleagues Mr. Haslbeck and Dr. Große for helpfull discussions and keeping the Mössbauer group at E15 alive.
- the administration team of E15GMK: Mrs. Clauß, Mr. Tosolini, Mr. Punsch and Mr. Leitwein.
- Sigi da Haglmo for his music.
- my wife Angela.